

AD-A217 127

**AEROSOL SAMPLE ACQUISITION FOR  
CHEMICAL AND BIOLOGICAL AGENT DETECTION**

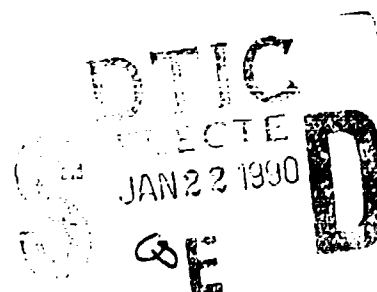
**Final Comprehensive Report**

**V. A. Marple and B. Y. H. Liu**

**1 December 1989**

**U. S. Army Research Office  
Contract DAALO3-88-C-0010**

**MSP Corporation  
1313 Fifth St. S.E., Suite 206  
Minneapolis, MN 55414  
612/379-3963**



**Approved for Public Release**

**Distribution Unlimited**

**90 01 22 0 54**

## REPORT DOCUMENTATION PAGE

1a. REPORT SECURITY CLASSIFICATION <u>Unclassified</u>		1b. RESTRICTIVE MARKINGS	
2a. SECURITY CLASSIFICATION AUTHORITY		3. DISTRIBUTION/AVAILABILITY OF REPORT  Approved for public release; distribution unlimited.	
2b. DECLASSIFICATION/DOWNGRADING SCHEDULE		4. PERFORMING ORGANIZATION REPORT NUMBER(S)	
5. MONITORING ORGANIZATION REPORT NUMBER(S)  <u>ARO 25616.1-CHS</u>		6a. NAME OF PERFORMING ORGANIZATION  MSP Corporation	
6b. OFFICE SYMBOL (If applicable)		7a. NAME OF MONITORING ORGANIZATION  U. S. Army Research Office	
6c. ADDRESS (City, State, and ZIP Code) 1313 Fifth St. S.E., Suite 206 Minneapolis, MN 55414		7b. ADDRESS (City, State, and ZIP Code) P. O. Box 12211 Research Triangle Park, NC 27709-2211	
8a. NAME OF FUNDING/SPONSORING ORGANIZATION U. S. Army Research Office		8b. OFFICE SYMBOL (If applicable)	
8c. ADDRESS (City, State, and ZIP Code) P. O. Box 12211 Research Triangle Park, NC 27709-2211		9. PROCUREMENT INSTRUMENT IDENTIFICATION NUMBER  <u>DAAL03-88-C-0010</u>	
10. SOURCE OF FUNDING NUMBERS		11. TITLE (Include Security Classification) Aerosol Sample Acquisition for Chemical and Biological Agent Detection	
PROGRAM ELEMENT NO.		PROJECT NO.	
TASK NO.		WORK UNIT ACCESSION NO.	
12. PERSONAL AUTHOR(S) V. A. Marple and B. Y. H. Liu		13a. TYPE OF REPORT Final	
13b. TIME COVERED FROM 15/4/88 TO 15/10/89		14. DATE OF REPORT (Year, Month, Day) 1989/12/01	
15. PAGE COUNT 121		16. SUPPLEMENTARY NOTATION The view, opinions and/or findings contained in this report are those of the author(s) and should not be construed as an official Department of the Army position, policy, or decision, unless so designated by other documentation.	
17. COSATI CODES		18. SUBJECT TERMS (Continue on reverse if necessary and identify by block number)	
FIELD		GROUP	
SUB-GROUP		Aerosol, sampling, detection,	
19. ABSTRACT (Continue on reverse if necessary and identify by block number)		20. DISTRIBUTION/AVAILABILITY OF ABSTRACT <input type="checkbox"/> UNCLASSIFIED/UNLIMITED <input type="checkbox"/> SAME AS RPT. <input type="checkbox"/> DTIC USERS	
21. ABSTRACT SECURITY CLASSIFICATION Unclassified		22a. NAME OF RESPONSIBLE INDIVIDUAL	
22b. TELEPHONE (Include Area Code)		22c. OFFICE SYMBOL	

The view, opinions, and/or findings contained in this report are those of the authors and should not be construed as an official Department of the Army position, policy, or decision, unless so designated by other documentation

Accession For	
NIOS ACTAI	<input checked="checked" type="checkbox"/>
DIAG FID	<input checked="checked" type="checkbox"/>
Unpublished	<input type="checkbox"/>
Justification	
By	
Distribution/	
Availability Codes	
Date/for	
Date/for	

A-1



# TABLE OF CONTENTS

	Page
List of Figures	i
List of Tables	iii
1. Introduction	1
2. Theoretical background and analysis	2
2.1 The virtual impactor	3
2.2 Numerical techniques for flow field analysis	5
2.3 Numerical techniques for particle trajectory calculation	19
2.4 Application of flow field and particle trajectory solution techniques to virtual impactors	23
3. Design considerations	27
3.1 Single nozzle virtual impactor concentrator	28
3.2 Multiple nozzle virtual impactor concentrator	30
4. Design and evaluation of a 22 liters per minute virtual impactor concentrator	37
4.1 Experimental evaluation and results	37
4.2 Conclusions	40
5. Vaporizer/pyrolyzer	45
5.1 Preliminary experiments	45
5.2 Results	49
5.3 Vaporizer/pyrolyzer for the virtual impactor concentrator	55
6. Summary of Important Results	56
7. Participating scientific personnel	56
8. Bibliography	56
Appendix A. Performance of the single nozzle virtual impactor	63
Appendix B. Performance of the multiple nozzle virtual impactor concentrator with sampling flow rates of 10, 100, 1000 and 22 liters per minute	73
Appendix C. Design drawings for the virtual impactor concentrator	110

## LIST OF FIGURES

- Figure 1. A typical system of node points for computation
- Figure 2. (a) Geometry of the virtual impactor (b) typical collection efficiency curves
- Figure 3. Virtual impactor efficiency curves showing (1) effect of jet Reynolds number, (b) ratio of minor to total flow, (c) ratio of receiving tube to jet diameter, (d) jet to plate distance, (e) nozzle angle and (f) effect of collection probe inlet.
- Figure 4. Dependence of nozzle diameter, pressure drop, jet velocity, and air power on flow rate for a virtual impactor concentrator
- Figure 5. Dependence of nozzle diameter, pressure drop, jet velocity, and air power on number of nozzles for a virtual impactor concentrator ( $Q = 10$  lpm,  $D = 2.0 \mu\text{m}$ )
- Figure 6. Dependence of nozzle diameter, pressure drop, jet velocity, and air power on number of nozzles for a virtual impactor concentrator ( $Q = 100$  lpm,  $D = 2.0 \mu\text{m}$ )
- Figure 7. Dependence of nozzle diameter, pressure drop, jet velocity, and air power on number of nozzles for a virtual impactor concentrator ( $Q = 1000$  lpm,  $D = 2.0 \mu\text{m}$ )
- Figure 8. Dependence of jet velocity on number of nozzles for a multiple nozzle virtual impactor concentrator ( $Q = 22$  lpm,  $D = 2.0 \mu\text{m}$ )
- Figure 9. Design of the virtual impactor concentrator with inlet
- Figure 10. Virtual impactor concentrator with inlet adapter piece
- Figure 11. Virtual impactor concentrator with large particle and small particle collection filters during test to determine collection efficiency and particle loss

- Figure 12. Collection efficiency and particle loss characteristics of virtual impactor concentrator
- Figure 13. Virtual impactor collector during pressure drop tests, showing locations where pressure was measured
- Figure 14. Pressure drop vs. flow characteristics of virtual impactor concentrator
- Figure 15. Voltage-current curves for foil vaporizer/pyrolyzer
- Figure 16. Foil temperature as a function of input power
- Figure 17. Experimental system for evaluating foil vaporizer/pyrolyzer
- Figure 18. Vaporization spectrum for 4  $\mu\text{L}$  of 0.1% DOP solution
- Figure 19. Vaporization spectrum for 4  $\mu\text{L}$  of 0.1% DOS solution
- Figure 20. Vaporization spectrum for de-ionized water of high and low purity
- Figure 21. Vaporization spectrum for ordinary tap water
- Figure 22. Vaporization spectrum for finger print
- Figure 23. Conceptual design of electrostatic precipitator for particle collection
- Figure 24. Design of electrostatic precipitator, vaporizer/pyrolyzer

## LIST OF TABLES

- Table 1. Electrical and thermal characteristics of foil vaporizer/pyrolyzer
- Table 2. Vaporization spectrum for 4  $\mu$ L of 0.1% DOP
- Table 3. Flash vaporization for 0.1% DOP
- Table 4. Vaporization spectrum for 4  $\mu$ L of 0.1% DOS
- Table 5. Flash vaporization for 0.1% DOS
- Table 6. Flash vaporization of de-ionized water
- Table 7. Vaporization spectrum for tap water
- Table 8. Flash vaporization of 4  $\mu$ L of tap water
- Table 9. Vaporization spectrum for finger print
- Table 10. Flash vaporization of finger print
- Table 11. Typical CNC count (#/cc) for various materials

## AEROSOL SAMPLE ACQUISITION FOR CHEMICAL AND BIOLOGICAL AGENT DETECTION

### 1. Introduction

The objective of this project is to investigate means for sampling aerosol particles from the ambient atmosphere for chemical and biological detection. Sample acquisition for such purpose require innovative approaches involving sample extraction from the ambient atmosphere, means for concentrating the aerosol particles from the extracted sample into a smaller airstream, collecting the concentrated particles onto a suitable substrate and then volatilizing and/or pyrolyzing the collected sample for subsequent physical or chemical analysis. While considerable knowledge is available on sample extraction from the ambient atmosphere, less is known about sample concentration and volatilization and pyrolyzing methods. The major focus of this project is to perform theoretical and experimental study of sample concentration and volatilization/pyrolysis methods with the goal of developing sufficient understanding of the processes so that complete sample concentration and volatilization/pyrolysis systems can be developed to suit different needs.

The report is divided into several sections with sections 2 - 4 devoted to the theoretical and experimental study of virtual impactor concentrators. Following a review of the theoretical methods used for virtual impactor studies in Section 2, a design analysis of virtual impactor concentrator is made in Section 3. A specific virtual impactor concentrator with a design flow rate of 22 liters per minute has been designed, constructed and tested and this

is described in detail in Section 4. Results of this study provides information for virtual impactor concentrator design of nearly any flowrate and particle cut size in the future. In Section 5, the problems related to particle collection for volatilization and pyrolysis are studied and analyzed. Several experimental volatilizer/pyrolyzer concepts were analysis and compared. Finally, an experimental volatilizer/ pyrolyzer was constructed and tested. On the basis of the study, a new volatilizer/pyrolyzer was then proposed for possible future development for various applications as described in Section 6.

## 2. Theoretical Background and Analysis

One of the most powerful techniques to determine the details of fluid flow fields and particle trajectories in an aerosol system is by use of numerical methods to solve the equations governing the flow field and the particle motion in that flow field. The governing equations for the flow field are the Navier-Stokes equations, and those for the particle trajectories, the equations of motion of the particles derived from the Newton's law relating the forces acting on the particle and the particle inertia.

The first part of this technique (flow field analysis) has been used by many investigators to determining the details of the flow around objects or through confined spaces. However, we have used both parts of the technique extensively to determine the particle trajectories as well as the flow field, and in some cases have used the technique to determine the particle concentration profile in an aerosol system. The technique has been used in detailed studies of

particle motion in inertial impactors, filters, elutriators, clean rooms, glove boxes, at inlets as well as in virtual impactors. In many of these studies the theoretical results have been compared with experimental results and agreement has been found to be excellent if the boundary conditions used in the actual system closely approximates those used in the theoretical analysis.

## 2.1 The virtual impactor

In a conventional impactor a jet of particle laden air is accelerated through a nozzle and directed at a flat plate. Particles larger than a certain critical size, the so-called cut size of the impactor, would impact upon the plate while smaller particles would follow the airstream and escape impaction. In a "virtual impactor" an accelerating nozzle is used as in the conventional real impactor to accelerate the airstream to a suitably high velocity, but the impaction plate is replaced by a void space in the form of a receiving tube through which a small fraction of the flow is allowed to pass. The main flow is deflected by the receiving tube, but the large particles are able to cross the streamlines and enter the receiving tube on account of their inertia, while the small particles are carried by the deflected airstream around the impactor. The output of the virtual impactor are in the form of two airstreams. The small stream (the minor flow) contains the large particles inertially impacted into the void space of the receiving tube, and the main airstream (the major flow), the small particles contained in the original flow. In contrast to the conventional real impactor where the large particles are impacted on a solid surface, the virtual impactor has the large

particles impacted into a void space and these particles would thus remain suspended or airborne.

The virtual impactor has two features which are desirable for the continuous sampling and analysis of airborne particles. First, both the large and small particles remain airborne and can be easily transported to another instrument for collection (such as a real impactor), to an instrument for analyses (such as an optical counter for continuous size distribution monitoring) or be removed from the airstream by filtration. Second, the particles larger than the cut size of the impactor are concentrated into the small fraction of the flow passing through the receiving tube. This makes analysis easier and more sensitive than if the particles were in the total flow entering the impactor.

The major features of the flow in a virtual impactor is rather simple. The air exits the nozzle and penetrates into the receiving tube that is about 30% larger in diameter than the nozzle. The depth (measured in number of receiving tube diameters) to which the air penetrates into the receiving tube depends upon the Reynolds number of the air passing through the nozzle. The Reynolds number is based on the nozzle diameter and the average velocity of the air in the nozzle. Most of the air reverses direction inside the receiving tube and exits the receiving tube at its outer diameter. Particles with large enough inertia cannot reverse direction and penetrate farther into the receiving tube. Since a small fraction of the flow entering the receiving tube is drawn through the tube, the large particles are concentrated into this small flow.

Although the flow in the virtual impactor is rather simple in its gross features, there is no analytical solution for the basic flow field and particle trajectory equations. Therefore, the problem must be solved numerically to determine the details of the flow field and particle trajectories.

## 2.2 Numerical Techniques for Flow Field Analysis

There are several numerical routines for solving the Navier-Stokes equations. One routine expresses the Navier-Stokes equations and the continuity equation in terms of the stream function and the vorticity. These two quantities are then solved numerically at the node points covering the computation domain. The velocity components at the node points are then determined from knowledge of the value of the stream function at these points. Other routines, such as SIMPLE and SIMPLER, solves directly for the velocity components and pressure at the node points. Both types of routines should give the same answer since the same basic sets of equations derived from the same basic Navier-Stokes equations are solved. In either case, the values of the velocity components at the node points is the final result. By using these velocity components, the particle trajectories are then calculated in the same manner for both cases.

We have used both types of routines. However, because the boundary conditions are slightly easier to define for the stream function - vorticity routine, we have chosen it to be the routine for analysis of the virtual impactor.

The general method of solution is to first express the Navier-Stokes equations in terms of the vorticity and the stream function.

The resulting differential equations are then changed to a finite difference form and solved by the method of relaxation over a grid of node points covering the field of interest. This method of analysis follows closely the general solution procedure described by GOSMAN, et al. (1969).

In the method devised by GOSMAN, et al. (1969) it is not necessary to have equally spaced grid lines. Therefore, more node points can be placed in areas where the velocity gradients are the largest. It is also assumed that the density and viscosity are constant and that there is no swirl so that there is no  $\theta$  component of velocity. Considering these assumptions the Navier-Stokes equations are:

$r$  direction:

$$\rho \left( V'_r \frac{\partial V'_r}{\partial r'} + V'_z \frac{\partial V'_r}{\partial z'} \right) = - \frac{\partial p}{\partial r'} + \mu \left( \frac{\partial^2 V'_r}{\partial r'^2} + \frac{1}{r'} \frac{\partial V'_r}{\partial r'} - \frac{V'_r}{r'^2} + \frac{\partial^2 V'_r}{\partial z'^2} \right) \quad (1)$$

$z$  direction:

$$\rho \left( V'_r \frac{\partial V'_z}{\partial r'} + V'_z \frac{\partial V'_z}{\partial z'} \right) = - \frac{\partial p}{\partial z'} + \mu \left( \frac{\partial^2 V'_z}{\partial r'^2} + \frac{1}{r'} \frac{\partial V'_z}{\partial r'} + \frac{\partial^2 V'_z}{\partial z'^2} \right) \quad (2)$$

and the continuity equation is:

$$\frac{\partial V'_r}{\partial r'} + \frac{V'_r}{r'} + \frac{\partial V'_z}{\partial z'} = 0 \quad (3)$$

The continuity equation is satisfied by the stream function,  $\psi'$ , defined as follows:

$$V'_z = -\frac{1}{r'} \frac{\partial \psi'}{\partial r'}, \quad V'_r = \frac{1}{r'} \frac{\partial \psi'}{\partial z'} \quad (4)$$

The vorticity,  $\omega'$ , is defined as:

$$\omega' = \frac{\partial V'_z}{\partial r'} - \frac{\partial V'_r}{\partial z'} \quad (5)$$

The above five equations are combined into two differential equations which fully describe the flow field in terms of  $\omega'/r'$  and the stream function. These equations are made dimensionless, as denoted by dropping the primes, by means of the jet diameter,  $W$ , and the average air velocity at this diameter,  $V_0$ . The dimensionless terms are:

$$r = \frac{r'}{W}, \quad z = \frac{z'}{W}, \quad (6)$$

$$\psi = \frac{\psi'}{V_0 W^2} \quad (7)$$

$$\frac{\omega}{r} = \frac{\omega'/r'}{V_0/W^2} \quad (8)$$

and

$$Re = \frac{\rho V_o W}{\mu} \quad (9)$$

The Navier-Stokes equations (equations 1 and 2), continuity equation (equation 3) and the definition of the stream function (equation 4) and the vorticity (equation 5) have been combined into two differential equations which fully describe the flow field in terms of  $w/r$  and the stream function. These two equations are made dimensionless by means of equations (6) to (9) and the results are:

$$r^2 \frac{\partial \left( \frac{\omega}{r} \frac{\partial \psi}{\partial z} \right)}{\partial r} - r^2 \frac{\partial \left( \frac{\omega}{r} \frac{\partial \psi}{\partial r} \right)}{\partial z} = \frac{1}{Re} \left\{ \frac{\partial (r^3 \frac{\partial \omega}{\partial r})}{\partial r} + \frac{\partial (r^3 \frac{\partial \omega}{\partial z})}{\partial z} \right\} \quad (10)$$

and

$$\frac{\omega}{r} r = - \frac{\partial}{\partial r} \left( \frac{1}{r} \frac{\partial \psi}{\partial r} \right) - \frac{\partial}{\partial z} \left( \frac{1}{r} \frac{\partial \psi}{\partial z} \right) \quad (11)$$

Equations (10) and (11) are integrated over a finite area around a typical node point and two finite difference equations are obtained. The typical node point is denoted by the subscript P and the surrounding node points by E, W, N, S, SE, NE, SW and NW. Figure 1 shows the orientation of these node points with respect to the  $r$  and  $z$  directions.

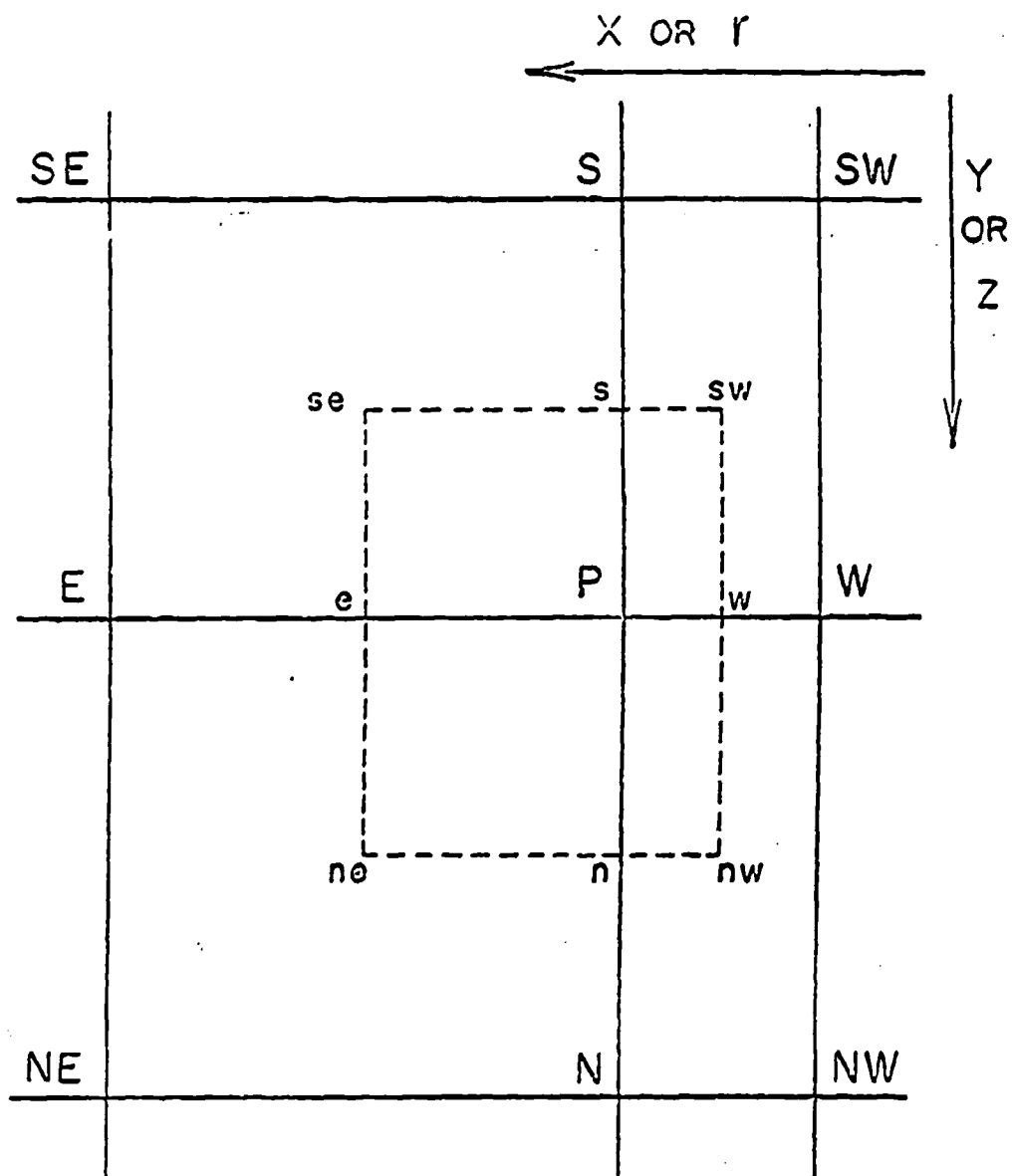


Figure 1. A typical system of node points for computation

The convective terms (the 2 terms on the left-hand side of equation (10) are integrated using the upwind difference method.

The result of integrating equation (10) and solving for  $\omega/r$  at point P is:

$$\left(\frac{\omega}{r}\right)_P = \frac{(\omega/r)_E(AE + RBE) + (\omega/r)_W(AW + RBW) + (\omega/r)_N(AN + r_p(RBN) + (\omega/r)_S AS + r_p(RBS)}{AE + AW + AN + AS + RBE + RBW + r_p^2(RBN + RBS)} \quad (12)$$

where:

$$AE = \{(\psi_S + \psi_{SE} - \psi_N - \psi_{NE}) + |\psi_S + \psi_{SE} - \psi_N - \psi_{NE}|\} DV$$

$$AW = \{(\psi_N + \psi_{NW} - \psi_S - \psi_{SW}) + |\psi_N + \psi_{NW} - \psi_S - \psi_{SW}|\} DV$$

$$AN = \{(\psi_E + \psi_{NE} - \psi_W - \psi_{NW}) + |\psi_E + \psi_{NE} - \psi_W - \psi_{NW}|\} DV$$

$$AS = \{(\psi_W + \psi_{SW} - \psi_E - \psi_{SE}) + |\psi_W + \psi_{SW} - \psi_E - \psi_{SE}|\} DV$$

(13)

$$DV = \frac{r_p}{2(r_E - r_W)(z_N - z_S)}$$

$$\begin{aligned}
 RBE &= \frac{1}{4} \frac{1}{Re} \frac{1}{r_p} \frac{1}{(r_E - r_p)} \frac{1}{(r_E - r_W)} (r_E + r_p)^3 \\
 RBW &= \frac{1}{4} \frac{1}{Re} \frac{1}{r_p} \frac{1}{(r_p - r_W)} \frac{1}{(r_E - r_W)} (r_W + r_p)^3 \\
 RBN &= 2 \frac{1}{Re} \frac{1}{(z_N - z_p)} \frac{1}{(z_N - z_S)} \\
 RBS &= 2 \frac{1}{Re} \frac{1}{(z_p - z_S)} \frac{1}{z_N - z_S}
 \end{aligned}
 \tag{14}$$

The result of integrating equation (11) and solving for the stream function at point P is:

$$\psi_P = \frac{\psi_E BE + \psi_W BW + \psi_N BN \frac{1}{r_p^2} + \psi_S BS \frac{1}{r_p^2} + (\omega/r)_P}{BE + BW + \frac{1}{r_p^2} (BN + BS)}
 \tag{15}$$

where:

$$\begin{aligned}
 BE &= 4 \frac{1}{r_p} \frac{1}{(r_E - r_p)} \frac{1}{(r_E - r_W)} \frac{1}{(r_E + r_p)} \\
 BW &= 4 \frac{1}{r_p} \frac{1}{(r_p - r_W)} \frac{1}{(r_E - r_W)} \frac{1}{(r_p + r_W)}
 \end{aligned}
 \tag{16}$$

$$BN = 2 \frac{1}{(z_N - z_P)} \frac{1}{(z_N - z_S)}$$

$$BS = 2 \frac{1}{(z_P - z_S)} \frac{1}{(z_N - z_S)}$$

Equations (12) and (15) are the equations used in calculating  $\omega/r$  and  $\psi$  at each node point.

Iteration equations are also required for grid points on the boundary. These equations for the boundary node points are somewhat different than for the interior nodes. For each of these boundary nodes there is a condition for the stream function and the vorticity.

First, the stream functions along the surface defining the nozzle is held constant and made equal to zero. Also, along the centerline the stream function is held constant at  $\psi_{\max}$ , where  $\psi_{\max} = 1/8$ . Finally, the stream function at the receiving tubes wall is constant and equal to the percentage of  $\psi_{\max}$  that is equal to the fraction of the flow in the major flow.

At the entrance  $V_z$  is assumed to be constant so that:

$$\psi = \psi_{\max} - \frac{r^2}{2} \left( \frac{W}{D_{\text{entrance}}} \right)^2 \quad (17)$$

The boundary condition at all exits assume the streamlines are straight or:

$$\psi_{IN} = \psi_{INM} \quad (18)$$

Where subscript IN denotes boundary nodes and INM denotes the adjacent interior node.

The vorticity boundary conditions along a solid surface can be deduced from the fact that the velocities along the wall and perpendicular to the wall are set equal to zero and the gradients perpendicular to the wall are assumed to be much larger than those along the wall. Therefore, for surfaces of constant  $z$ , equation (10) becomes:

$$\frac{\partial^2(\omega/r)}{\partial z^2} = 0 \quad (19)$$

and the equation (11) becomes:

$$\frac{\omega}{r} = -\frac{1}{r^2} \frac{\partial^2 \psi}{\partial z^2} \quad (20)$$

leading to the boundary condition:

$$\left(\frac{\omega}{r}\right)_P = -\frac{3}{r_P} \frac{(\psi_{NP} - \psi_P)}{(z_P - z_{NP})^2} - \frac{(\omega/r)_{NP}}{2} \quad (21)$$

where the subscript P denotes any node on the surface and the subscript NP denotes the adjacent interior node.

For surface where  $r=\text{constant}$ , equation (10) becomes:

$$\frac{\partial}{\partial r} \left( r^3 \frac{\partial \omega}{\partial r} \right) = 0 \quad (22)$$

equation (11) becomes:

$$\frac{\omega}{r} = -\frac{1}{r} \frac{\partial}{\partial r} \left( \frac{1}{r} \frac{\partial \psi}{\partial r} \right) \quad (23)$$

and the boundary condition becomes:

$$\begin{aligned} \left( \frac{\omega}{r} \right)_P = (\psi_{NP} - \psi_P) + \left( \frac{\omega}{r} \right)_{NP} \frac{r_P^3}{(r_P - r_{NP})} \frac{1}{16} \left[ 4 r_{NP} \ln \left( \frac{r_{NP}}{r_P} \right) - \frac{r_{NP}^4}{r_P^2} + \right. \\ \left. r_P, \frac{r_P^3}{(r_P - r_{NP})} \frac{1}{16} \left[ 4 r_{NP}^2 \ln \left( \frac{r_{NP}}{r_P} \right) - \frac{r_{NP}^4}{r_P^2} + r_P^2 \right] - \frac{1}{8} (r_P^2 - r_{NP}^2)^2 \right] \end{aligned} \quad (24)$$

Where the subscripts P denote grid points on a surface and NP denotes the adjacent interior grid point.

Along the conical entrance surface neither equation (20) nor (21) applies, since the wall is at an angle to the grid lines. However, since the cone surface is at an angle of 30° to the centerline, equation (21) is used instead of equation (20). Although this is an approximation, the conical entrance is the farthest surface from the receiving tube and is not expected to affect the flow in the inertial separation region. Therefore, equation (21) is used along the conical wall with the subscript P denoting a boundary node point. The

subscript NP denotes the adjacent interior node point on a grid line parallel to the entrance and passing through the point P.

Even though the vorticity values along the conical surface can now be solved, there is still one more problem presented by this surface. This problem arises when the vorticity is calculated at the node points directly adjacent to the cone. If the expressions for AE and AN of equation (13) are examined it will be seen that the stream function at point NE must be known. We are assuming in Figure 1 that the conical surface is passing through points E and N and point NE, which in  $(I+1, J+1)$ , will lie outside of the calculation domain. Therefore, the expression for AE and AN must be revised when the vorticity at nodes in this position are calculated.

The revision of AE and AN can best be performed by noting that AE and AN are actually

$$AE = \{(\psi_{se} - \psi_{ne}) + |\psi_{se} - \psi_{ne}|\} DV$$

and

(25)

$$AN = \{(\psi_{ne} - \psi_{nw}) + |\psi_{ne} - \psi_{nw}|\} DV$$

The subscripts refer to the corners of the dotted rectangle of Figure 1.

It can be seen in Figure 1 that the point denoted by subscript ne lies on the surface of the cone. Since the boundary condition for the stream function on the conical surface is  $\psi=0$ ,  $\psi_{ne}=0$  in equations

(25). If the other terms are expressed as an average of their four surrounding node points, equation (25) becomes:

$$AE = \{(\psi_S + \psi_{SE} + \psi_E + \psi_P) + |\psi_S + \psi_{SE} + \psi_E + \psi_P|\} DV \quad (26)$$

$$AN = \{(-\psi_N - \psi_{NW} - \psi_W - \psi_P) + |-\psi_N - \psi_{NW} - \psi_W - \psi_P|\} DV$$

These equations must be used in place of AE and AN in equations (13) when the vorticity is calculated at the node points one step from the conical surface.

At the entrance, the flow is assumed uniform and parallel to the impactor axis. Therefore,  $\omega/r = 0$ . At the exit it is assumed:

$$\left(\frac{\omega}{r}\right)_{IN} = \left(\frac{\omega}{r}\right)_{INM} \quad (27)$$

On the centerline both  $\omega$  and  $r$  are equal to zero. Hence  $\omega/r$  becomes indeterminate. However, near the centerline  $\omega/r$  is an even function of  $r$  so that:

$$\omega/r = A + Br^2 \quad (28)$$

At the centerline  $r = 0$  so  $(\omega/r)_1 = A$ , where the subscript 1 denotes a centerline node.

The values of A can be determined by evaluating equation (28) at the two grid lines adjacent to the centerline. At the nearest grid line

$$(\omega/r)_2 = A + Br_2^2 \quad (29)$$

and at the next grid line

$$(\omega/r)_3 = A + Br_3^2 \quad (30)$$

Since the grid lines near the centerline are equally spaced,  $r_2 = \Delta r$  and  $r_3 = 2\Delta r$  where  $\Delta r$  is the grid spacing, A can thus be solved as:

$$A = \left(\frac{\omega}{r}\right)_1 = \frac{4(\omega/r)_2 - (\omega/r)_3}{3} \quad (31)$$

Which is the iteration equation used on the centerline.

After the stream function has been determined at each of the node points, the velocity component in both the r and z directions can be calculated.

The x-component of velocity can be determined from the definition of stream function:

$$V_r = \frac{1}{r} \frac{\partial \psi}{\partial z} \quad (32)$$

Since the grid lines are not equally spaced, node P is not equally distant from nodes S and N as can be seen in Figure 1. Therefore,

equation (32) is weighted more in favor of the closer grid point as follows:

$$V_r = \frac{1}{r} \left( \frac{\partial \psi}{\partial z} \right)_n \left( \frac{z_P - z_S}{z_N - z_S} \right) + \frac{1}{r} \left( \frac{\partial \psi}{\partial z} \right)_s \left( \frac{z_N - z_P}{z_N - z_S} \right) \quad (33)$$

If the partial derivatives are put in finite difference form, equation (33) becomes:

$$V_r = \frac{1}{r_p} \frac{(\psi_N - \psi_P)}{(z_N - z_P)} \frac{(z_P - z_S)}{(z_N - z_S)} + \frac{(\psi_P - \psi_S)}{(z_P - z_S)} \frac{(z_N - z_P)}{(z_N - z_S)} \quad (34)$$

The z-component of velocity is derived in exactly the same manner from the equation:

$$V_z = -\frac{1}{r} \frac{\partial \psi}{\partial r} \quad (35)$$

to give:

$$V_z = \frac{1}{r_p} \frac{(\psi_E - \psi_P)}{(r_E - r_P)} \frac{(r_W - r_P)}{(r_E - r_W)} + \frac{(\psi_P - \psi_W)}{(r_P - r_W)} \frac{(r_P - r_E)}{(r_E - r_W)} \quad (36)$$

The value of  $V_z$  at the centerline cannot be determined from equation (36) since  $r_p = 0$  for this case. At the centerline it can be assumed that the stream function is an even function of  $r$

$$\psi = ar^2 + b \quad (37)$$

where  $a$  and  $b$  are constants. It can be seen that  $b = \psi_P$  and  $a = \frac{\psi_{NP} - \psi_P}{r_{NP}^2}$ . Again the subscript  $P$  denotes a node on the centerline and  $NP$  denotes the adjacent interior node.

The definition of the stream function can now be used to derive an expression for  $V_z$ .

$$V_z = -\frac{1}{r} \frac{\partial \psi}{\partial r} \quad (38)$$

Substitute equation (37) into (38) and we obtain

$$V_z = -2a$$

or

$$V_z = \frac{2(\psi_{NP} - \psi_P)}{r_{NP}^2} \quad (39)$$

Which is used in calculating  $V_z$  on the centerline.

### 2.3 Numerical Technique for Particle Trajectory Calculation

Once the flow field has been determined as explained in the previous section, the particle trajectories can be calculated. The

starting point for the particle trajectory calculations is the values of the velocity components in the  $r$  and  $z$  directions at each node point. Recall that these velocity components were the final result of the flow field calculation.

The governing equation for the particle trajectory is the Newton's law governing the particle motion:

$$F = ma \quad (40)$$

where  $F$  is the aerodynamic force on the particle,  $m$  is the mass of the particle and  $a$  is the acceleration of the particle. By assuming Stokes' law of resistance, the equations of motion of a particle in the  $r$  and  $z$  directions are:

$$m \frac{d^2 r'}{dt'^2} = \frac{3\pi\mu D_p}{C} \left( V'_r - \frac{dr'}{dt'} \right)$$

and

$$m \frac{d^2 z'}{dt'^2} = \frac{3\pi\mu D_p}{C} \left( V'_z - \frac{dz'}{dt'} \right) \quad (41)$$

These equations can be made dimensionless by using:

$$r = \frac{r'}{W} \quad z = \frac{z'}{W}$$

$$V_r = \frac{V'_r}{V_0} \quad V_z = \frac{V'_z}{V_0} \quad (42)$$

$$t = \frac{t'}{W/V_0}$$

The equations now become:

$$\frac{Stk}{2} \frac{d^2 r}{dt^2} = V_r - \frac{dr}{dt}$$

$$\frac{Stk}{2} \frac{d^2 z}{dt^2} = V_z - \frac{dz}{dt}$$
(43)

where

$$Stk = \frac{\rho_p C V_0 D_p^2}{9\mu W}$$
(44)

The square root of the Stokes number,  $\sqrt{Stk}$ , is used as a dimensionless particle size.

It should be noted that equations (43) are interrelated since both fluid velocity components,  $V_r$  and  $V_z$  are dependent on the position of the particle,  $(r, z)$ . Therefore, these two equations must be integrated simultaneously.

Several numerical methods are available for carrying out this integration. The method we have chosen is the Runge-Kutta fourth order method, since it is self starting and gives good accuracy.

In general the method for determining the particle trajectory is as follows:

1. A particle of known Stokes number is assigned to start at some point at the virtual impactor inlet with a velocity equal to that of the fluid at that point.
2. Linear interpolation formulas are derived for the velocity components  $V_r$  and  $V_z$  based on the values of the velocity components at the four node points situated at the corners of the elemental area in which the particle is located.
3. An estimate is made of the particle crossing time, i.e. the time taken by the particle to cross this elemental area.
4. Equations (43) are integrated numerically to determine a new particle position using the Runge-Kutta method with a time increment equal to 1/10th of the estimated particle crossing time.
5. A check is made to see if this new position of the particle is still within the same elemental area. If the particle is still in the same area, step 4 is repeated with the same time increment until a grid line is crossed.
6. When a grid line is crossed the process is started again at step 2 for this new elemental area. This is continued until the particle reaches the exit of either the major or minor flows or strikes a surface.

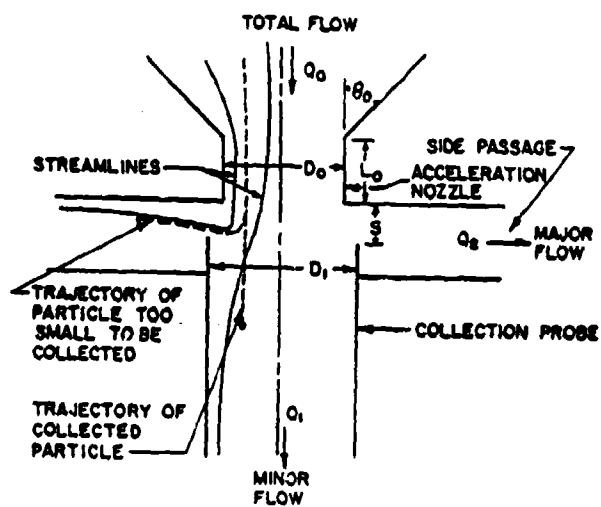
By starting particles of different sizes (Stokes Numbers) at different points along the inlet, it is possible to construct efficiency curves for particles passing through the receiving tube with the minor flow and out the side exit with the major flow. In addition, it is possible to determine the percentage of particles of any size that

hit a surface. These are considered to be particle losses in the impactor.

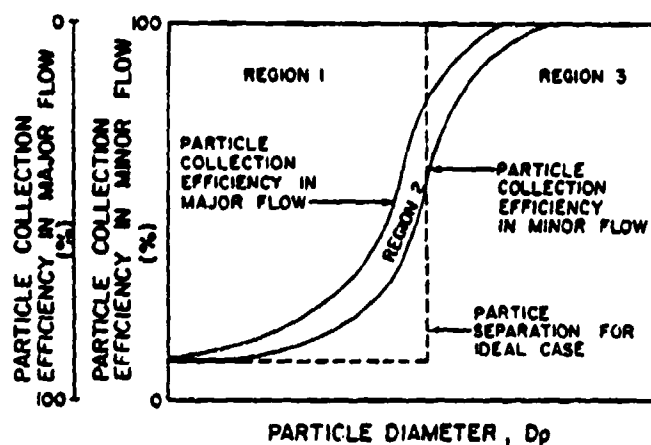
#### 2.4 Application of Flow Field and Particle Trajectory Solution Techniques to Virtual Impactors

The best application of the flow field and particle trajectory solution techniques to aerosol transport problems is on a case by case basis so the exact boundary conditions can be modeled. However, since virtual impactors are rather simple instruments with air flowing from nozzles into a receiving tubes, it is possible to do a parametric study of virtual impactors and apply the results from the case that is the closest to that of interest. This was done by Marple and Chien (1980) and the resulting efficiency curves from their study reproduced in figures 2 and 3. Figure 2 shows the basic configuration and defines the parameters while Figure 3 shows the efficiency curves. For cases which are different from those given in these figures, such as different geometries or flow rates, the technique should be applied with the correct boundary conditions.

The efficiency curve shown in Figure 3 are for the percentage of particles passing through the nozzle and penetrating into the receiving tube. These are the large particle collection efficiency curves. In each set of efficiency curves, one parameter has been varied. Therefore, it was possible to study the effects of varying parameters such as the angle of the inlet, the distance between the receiving tube inlet and the nozzle exit, the Reynolds Number, the configuration of the inlet to the receiving tube and other relationships between the diameters of the receiving tube to that of



(a) VIRTUAL IMPACTOR



REGION 1-PARTICLES IN THE MAJOR FLOW  
 REGION 2-PARTICLES IMPACTED ON COLLECTION PROBE  
 REGION 3-PARTICLES IN THE MINOR FLOW

(b) COLLECTION EFFICIENCY CURVES

Figure 2. (a) Geometry of the virtual impactor (b) typical collection efficiency curves

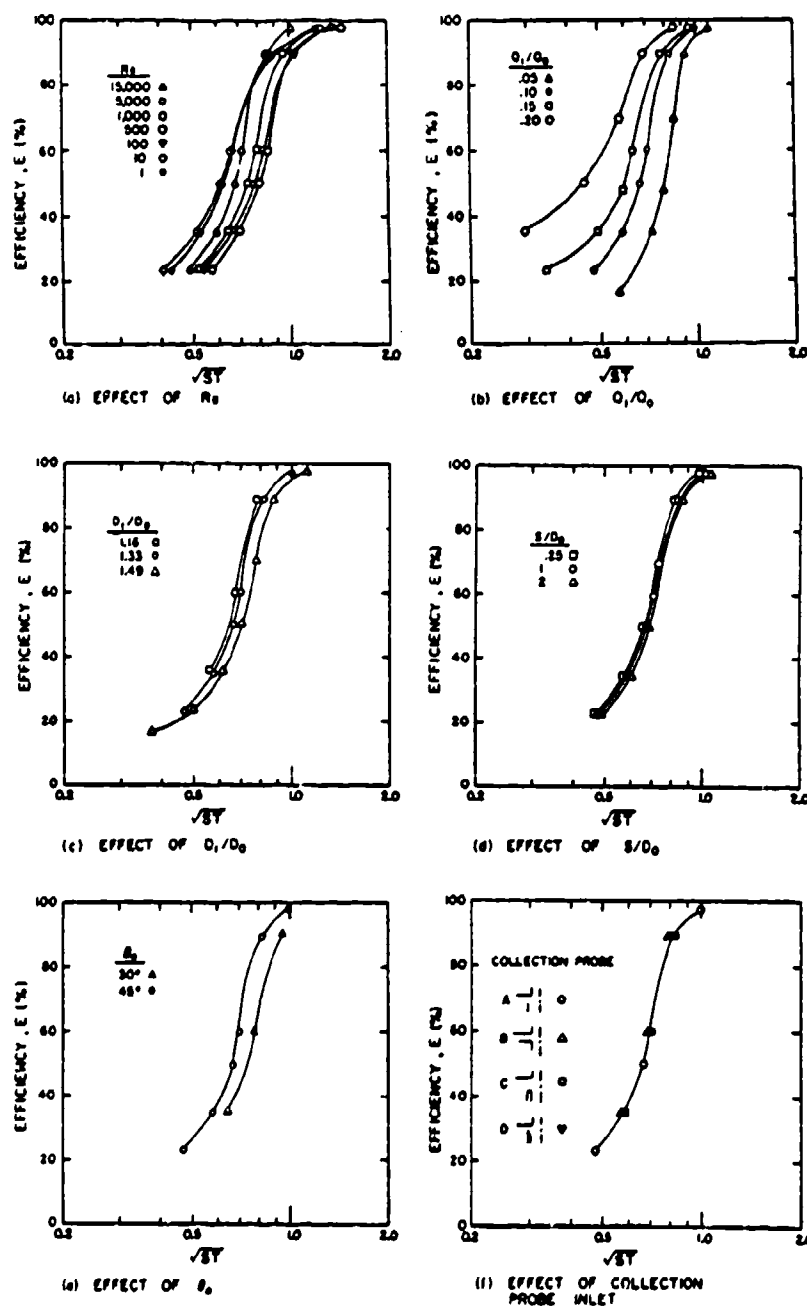


Figure 3. Virtual impactor efficiency curves showing (1) effect of jet Reynolds number, (b) ratio of minor to total flow, (c) ratio of receiving tube to jet diameter, (d) jet to plate distance, (e) nozzle angle and (f) effect of collection probe inlet.

the nozzle. One striking feature of these efficiency curves is that all parameters except the minor to total flow ratio parameter have only a minor influence on the position or the shape of the efficiency curve. The reason for this is that the flow from the nozzle penetrates into the receiving tube and all of the separation is accomplished within the receiving tube. Other parameters, such as the distance between the receiving tube inlet and nozzle exit, the angle of the inlet, the nozzle Reynolds Number, shape of the receiving tube, all have little influence on the collection characteristics.

The one parameter that has a significant influence on the efficiency curve is the ratio of minor to total flow. As the minor flow is decreased, the efficiency curve shifts to the larger sizes of STK indicating a larger cutoff size. In addition, the cutoff characteristics of the efficiency curves become sharper. Also note that the efficiency curves asymptotically approach the value corresponding to the percentage of flow passing through the receiving tube for the smaller particle sizes. Therefore, it is desirable to have as small a minor flow as possible to obtain a sharp cutoff characteristic.

In the above described calculation results, it is assumed that particles impacting on the receiving tube walls will stick to the walls. Since this may not occur in actual practice when solid particles are involved, there is some uncertainty in the use of these theoretical results for actual impactor designs. For these and other reasons, impactors designed on the basis of theoretical calculations must be calibrated and studied experimentally.

### 3. Design Considerations

The starting point in the design of virtual impactor concentrators is the Stokes number, defined as the ratio of the particle stopping distance to the radius of the nozzle,

$$Stk = \frac{\tau U}{R} \quad (45)$$

where  $Stk$  is the Stokes number,  $\tau$  is the particle relaxation time and  $U$  is the mean jet velocity in the nozzle. The particle relaxation time,  $\tau$ , is a function of the particle diameter,  $D_p$ , and particle density,  $\rho_p$ ,

$$\tau = \frac{D_p^2 \rho_p}{18 \mu C} \quad (46)$$

where  $C$  is the particle slip correction given by

$$C = 1 + 1.246 Kn + 0.42 Kn e^{-0.87/Kn} \quad (47)$$

and  $Kn$  is the Knudsen number defined by

$$Kn = \frac{2\lambda}{D_p} \quad (48)$$

To design a virtual impactor concentrator, the functional relationship between the efficiency of the concentrator and the Stokes must be known. Theoretical and experimental studies of the virtual impactor

described above have shown that the collection efficiency,  $\eta$ , is primarily a function of the Stokes number,  $St$ ,

$$\eta = f(Stk) \quad (49)$$

with the other parameters, such as the jet to receiving tube distance, jet Reynolds number, the nozzle to receiving-tube diameter ratio, the major and minor flow ratios, etc. playing a secondary, though sometimes important, role. Therefore, the design of virtual impactor concentrator can begin by first as finding a constant Stokes number at the desired impactor cut-point and then calculating the corresponding nozzle diameters and required jet velocities to achieve the desired cut point. The results can then be verified by constructing an experimental impactor and performing the necessary calibration and verification studies. The design procedure is described in more detail below.

### 3.1 Single Nozzle Virtual Impactor

In the case of the single nozzle impactor, the design is straight forward. Let  $q$  be the volumetric flow through the nozzle.  $q$  is related to the mean jet velocity,  $U$ , as follows,

$$q = \pi R^2 U \quad (50)$$

By means of Equations (45) and (50) we have

$$R = \left( \frac{q \tau}{\pi S_t} \right)^{1/3} \quad (51)$$

for the nozzle radius. Knowing the nozzle radius, the required jet velocity,  $U$ , can then be calculated by means of Equation (50). To determine the pressure drop,  $\Delta P$ , across the nozzle, we make use of the Bernoulli's law and the definition of the nozzle discharge coefficient,  $C_d$ ,

$$U = C_d \sqrt{\frac{2\Delta P}{\rho}} \quad (52)$$

from which we obtain

$$\Delta P = \frac{\rho U^2}{2 C_d^2} \quad (53)$$

The power required to maintain an air flow at the rate of  $q$  through a nozzle at a pressure drop of  $\Delta P$  is

$$P_{th} = q \Delta P \quad (54)$$

which is the theoretical air power for operating the virtual impactor concentrator. The actual input power,  $P$ , to the blower or pump is higher by a factor equal to the blow or pump efficiency,  $\eta_b$ ,

$$P = \frac{P_{th}}{\eta_b} \quad (55)$$

Figure 4 shows the calculated nozzle diameter, jet velocity, pressure drop and the theoretical air power for a single nozzle virtual impactor concentrator designed for a cut-point diameter of  $2.0 \mu\text{m}$ . The calculation has been made by assuming  $\sqrt{\text{St}} = 0.65$  and a nozzle discharge coefficient of 0.8. Other values can be used for the calculation, but the results will not differ substantially from those obtained.

It is interesting to note that the nozzle diameter, the jet velocity, the pressure drop and the theoretical air power all increase substantially with increasing flow rate. For a 1 liters per minute (lpm) sampling flow rate a nozzle of 1.11 mm in diameter is required. The required nozzle diameter increases to 1.11 cm at a flow rate of 1000 lpm. The corresponding jet velocity increases from 1,740 cm/s to 17,400 cm/s, and the pressure drop from 1.14 to 114 inch  $\text{H}_2\text{O}$ . The theoretical air power increases from 4.71 mW to 471 W. More detailed data on the design calculations are given in Appendix. A.

### 3.2 Multiple-nozzle Virtual Impactor Concentrator

Because of the high pressure drop and power requirement of the single nozzle virtual impactor concentrator, practical impactors with moderate to high flow rate requirements generally must be designed with multiple nozzles. For a multiple nozzle impactor consisting of  $n$  identical nozzles operating in parallel, the flow rate through each nozzle is

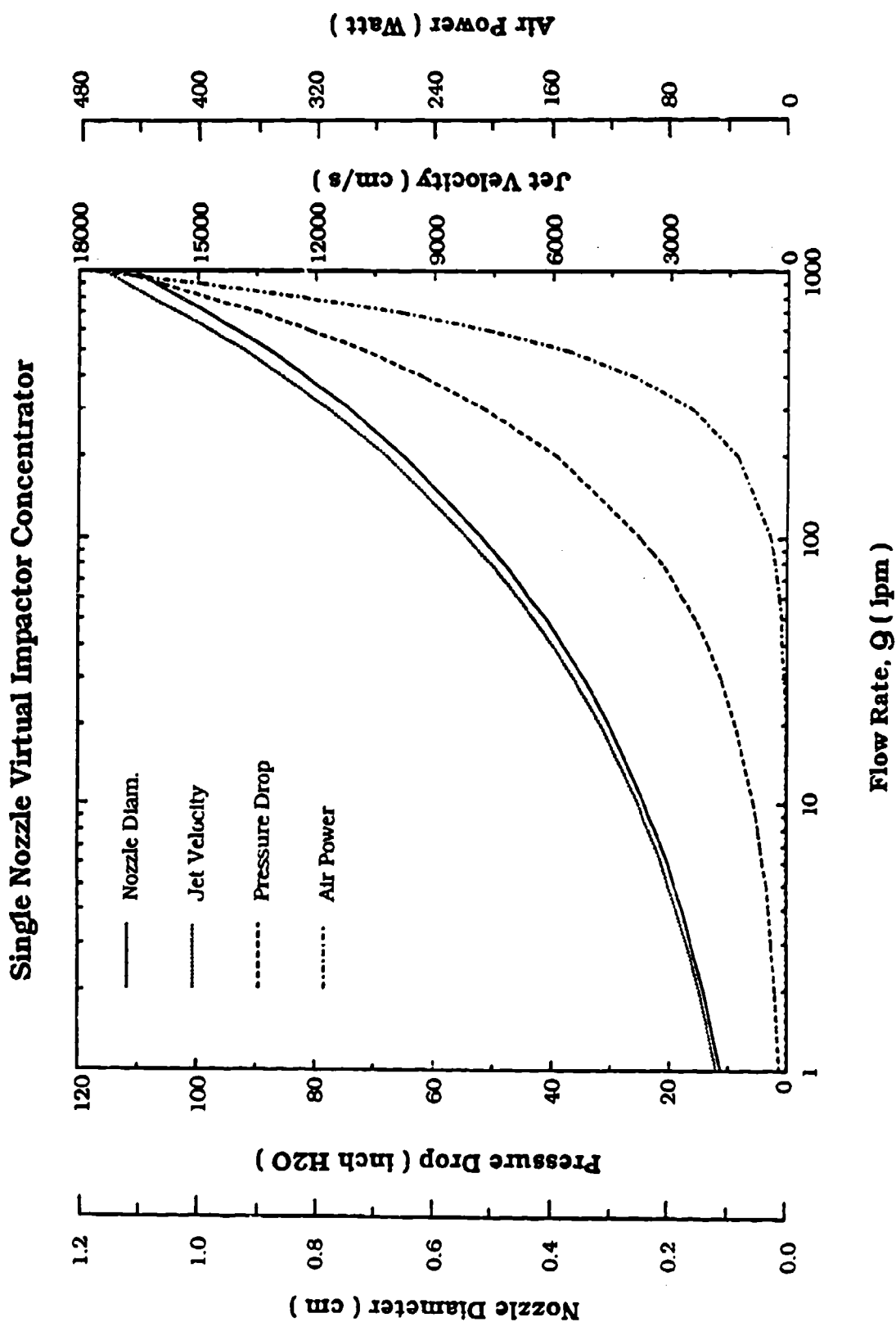


Figure 4. Dependence of nozzle diameter, pressure drop, jet velocity, and air power on flow rate for a virtual impactor concentrator

$$q = \frac{Q}{n} \quad (56)$$

where  $Q$  is total flow rate through the multiple nozzle impactor. by substituting Eq. (56) into Equations (51) and making use of Equations (51) - (54), we have the following equations for the design of multiple nozzle impactor

$$R = \left( \frac{Q \tau}{n \pi S_t} \right)^{1/3} \quad (57)$$

$$U = C_d \sqrt{\frac{2\Delta P}{\rho}} \quad (58)$$

$$\Delta P = \frac{\rho U^2}{2 C_d^2} \quad (59)$$

$$P_{th} = Q \Delta P \quad (60)$$

Figures 5 - 8 show the calculated impactor characteristics for a virtual impactor concentrator operating with a flow rate of 10, 100, 1000 and 22 lpm and a cut point diameter of 2.0  $\mu\text{m}$ . In this calculation, the number of nozzles has been varied from 1 to 100. The advantage of the multiple nozzle approach is thus obvious. For instance, for a virtual impactor concentrator with a sampling flow rate of 22 lpm, a single nozzle design will result in a concentrator having a pressure drop of 8.92 inch  $\text{H}_2\text{O}$ . With 100 nozzles, the pressure drop is reduced to 0.414 inch  $\text{H}_2\text{O}$ . The decrease in the theoretical air power is quite dramatic. A single nozzle impactor

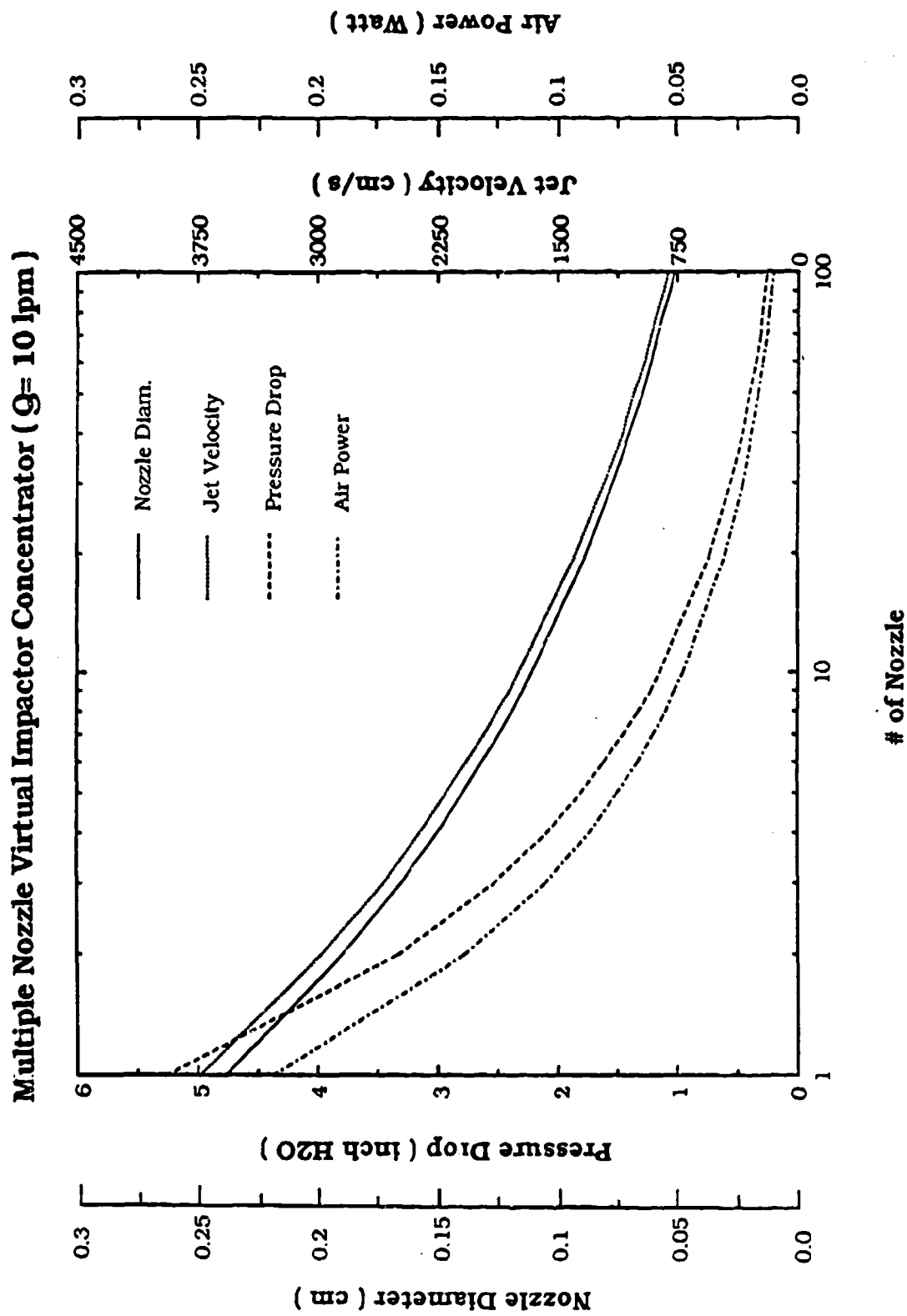


Figure 5. Dependence of nozzle diameter, pressure drop, jet velocity, and air power on number of nozzles for a virtual impactor concentrator ( $Q = 10 \text{ lpm}$ ,  $D = 2.0 \text{ }\mu\text{m}$ )

Multiple Nozzle Virtual Impactor Concentrator (  $Q = 100 \text{ lpm}$  )

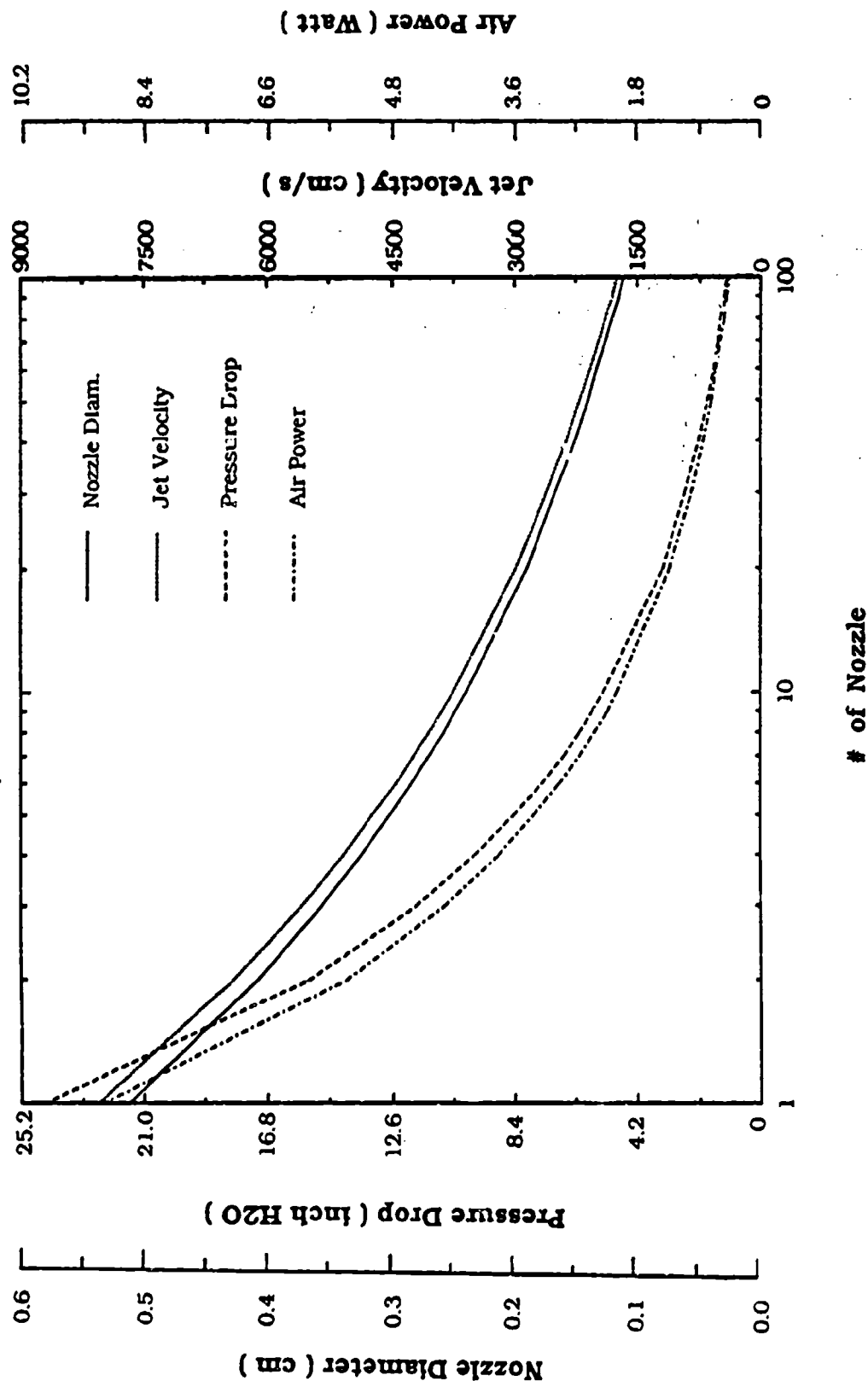


Figure 6. Dependence of nozzle diameter, pressure drop, jet velocity, and air power on number of nozzles for a virtual impactor concentrator ( $Q = 100 \text{ lpm}$ ,  $D = 2.0 \text{ } \mu\text{m}$ )

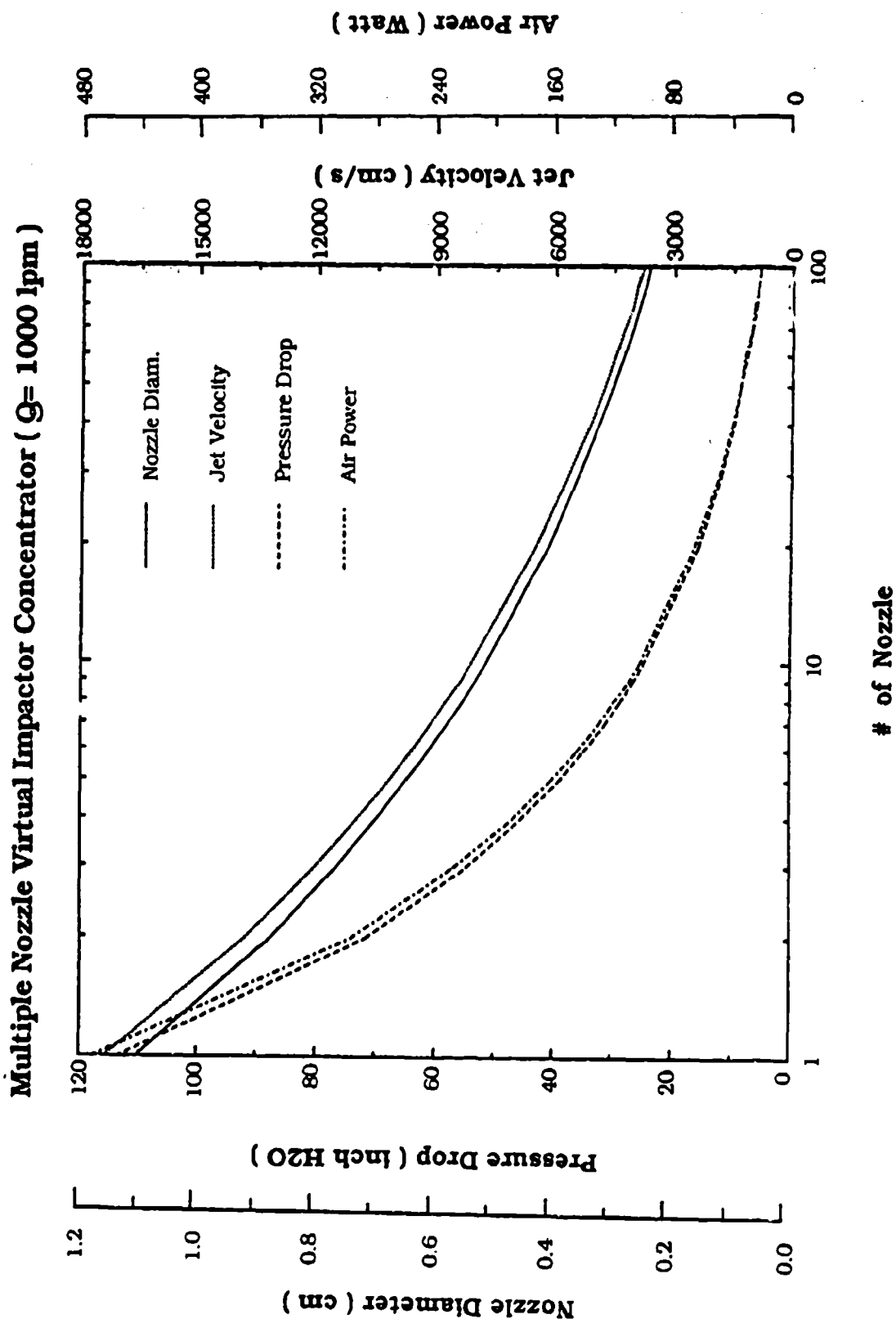


Figure 7. Dependence of nozzle diameter, pressure drop, jet velocity, and air power on number of nozzles for a virtual impactor concentrator ( $Q = 1000$  lpm,  $D = 2.0 \mu\text{m}$ )

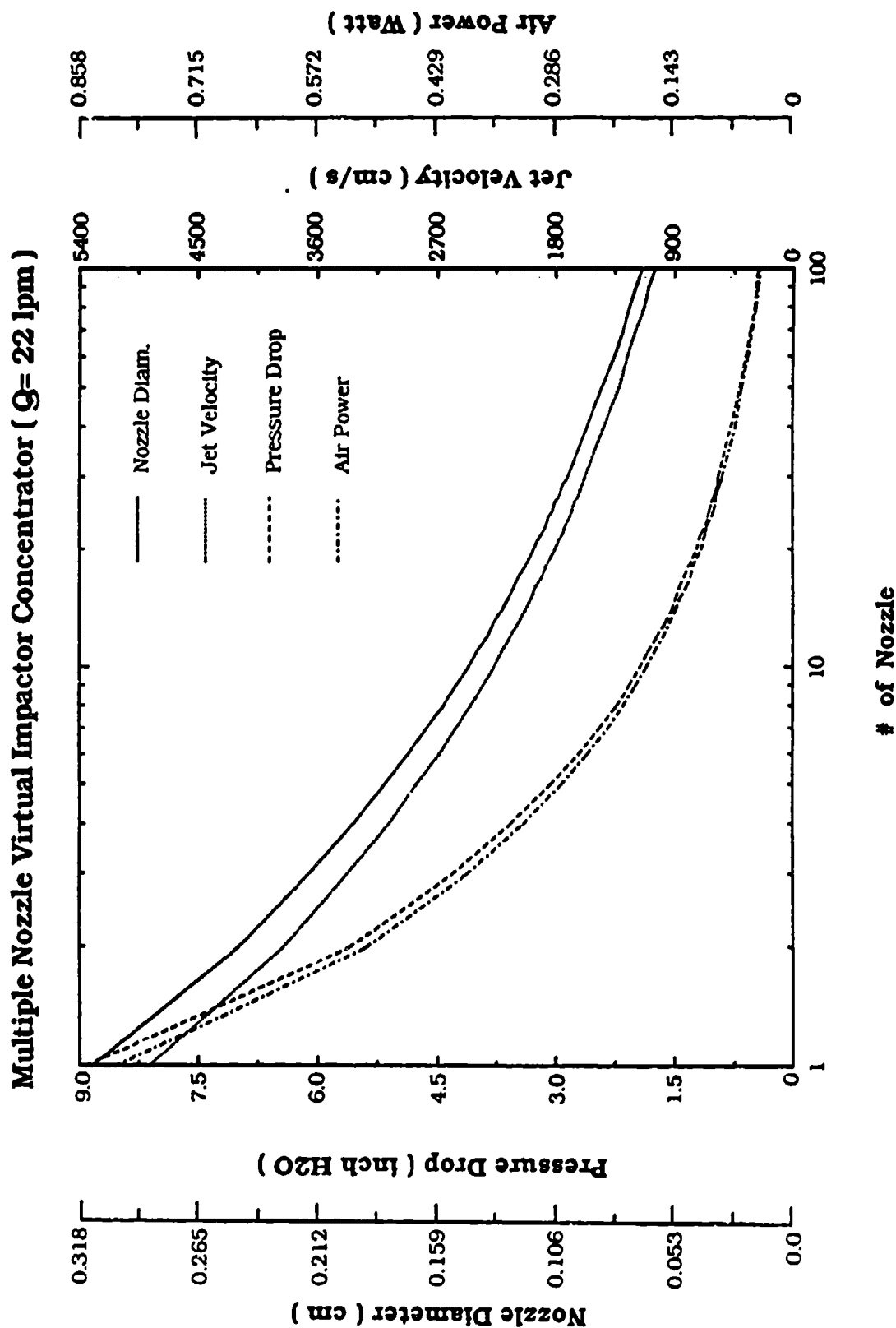


Figure 8. Dependence of jet velocity on number of nozzles for a multiple nozzle virtual impactor concentrator ( $Q = 22$  lpm,  $D = 2.0 \mu\text{m}$ )

requires a power of 814 mW, while a 100 nozzle impactor requires only 37.8 mW of theoretical air power. More detailed data on the design calculations are given in Appendix B.

#### 4. Design and Evaluation of a 22 Liter Per Minute Virtual Impactor Concentrator

On the basis of the above design considerations, a virtual impactor having a sampling flow rate of 22 liters per minute was designed, constructed and tested. The concentrator consists of 22 nozzles each operating at a flow rate of 1 liter per minute. The specifications of the design are as follows:

Nozzle diameter	=	0.048"
Total flow rate	=	22 lpm
Major flow rate	=	21 lpm
Minor flow rate	=	1.0 lpm
Number of nozzles	=	22

A design drawing for the concentrator is shown in Figure 9. Detailed design of the various parts of the system is given in Appendix C.

##### 4.1 Experimental Evaluation and Results

For the purpose of the laboratory evaluation of the virtual impactor concentrator, an inlet adapter piece is constructed so that the test aerosol can be introduced into the concentrator through this adapter piece. Figure 10 shows the concentrator with this inlet adapter piece used during the test in place of the regular inlet.

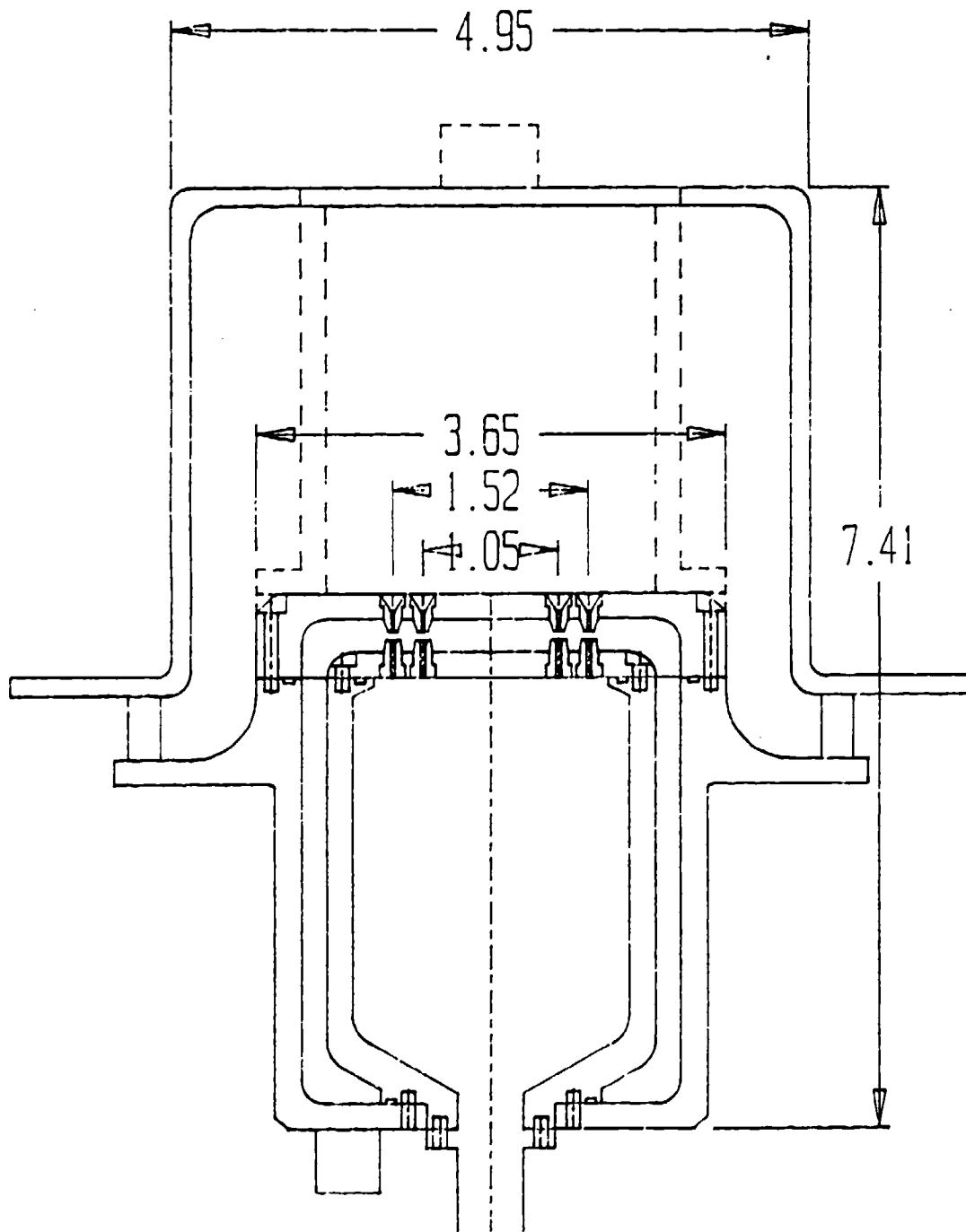


Figure 9. Design of the virtual impactor concentrator with inlet

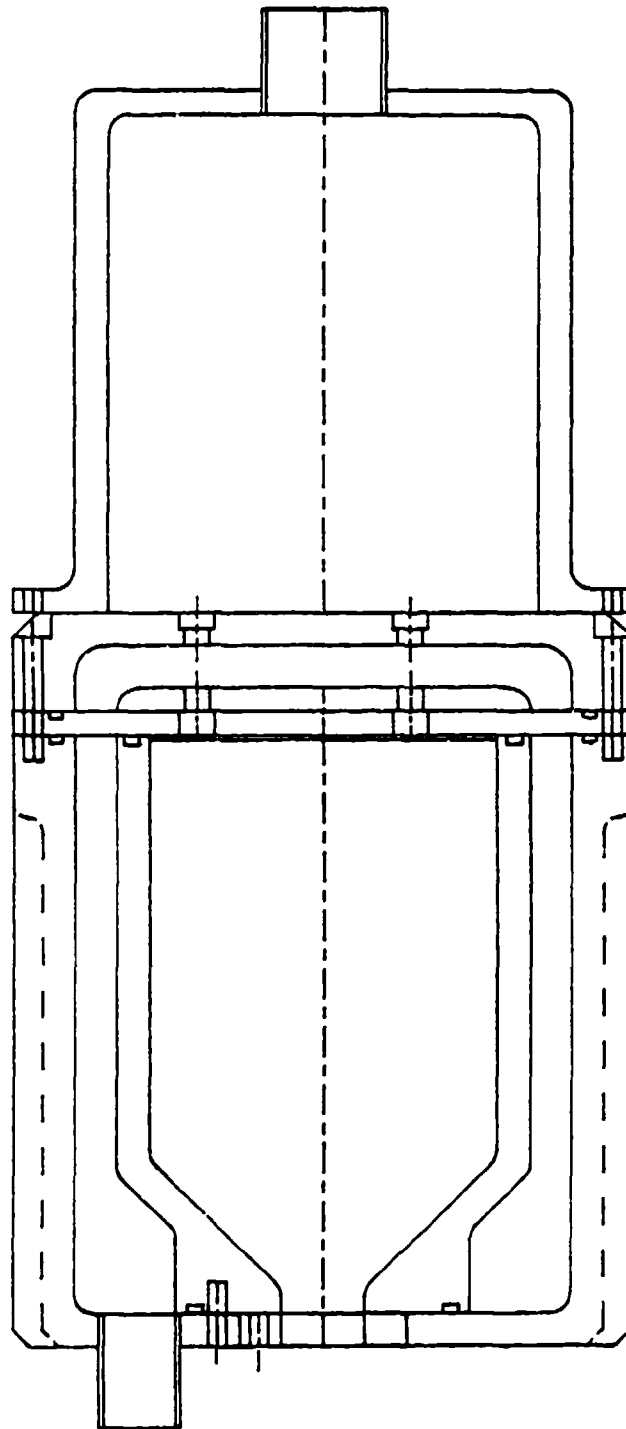


Figure 10. Virtual impactor concentrator with inlet adapter piece

The actual calibration was made using liquid oleic-acid particles generated with a Berglund-Liu vibrating orifice monodisperse aerosol generator (Berglund and Liu, 1973) to determine its particle collection efficiency and loss characteristics. Fluorescent uranine-tagged oil drops of a specific particle size were generated by the Berglund-Liu generator, and were collected using the large particle and small particle collection filters shown in Figure 11. Particle loss inside the minor flow chamber was also determined by wiping the internal surfaces with a wet cotton swap and measuring the fluorescence. The experimental results are shown in Figure 12.

Results of these experiments show that the virtual impactor concentrator has excellent particle concentrating performance characteristics. The 50% aerodynamic was found to be  $3.1\text{ }\mu\text{m}$  and the internal particle loss in the minor flow chamber was quite small, ranging from 0.5% for a particle diameter of  $2.53\text{ }\mu\text{m}$ , to a maximum of 12.8% at the particle diameter of  $7.31\text{ }\mu\text{m}$ .

The pressure drop through the concentrator was checked at various flow rates and at the locations shown in Figure 13 using an inclined water manometer. The results are shown in Figure 14. For the operating conditions of 21 lpm major flow and 1 lpm minor flow, the pressure drops are 0.9 and 0.03 in.  $\text{H}_2\text{O}$  respectively.

#### 4.2 Conclusions

The experimental virtual impactor concentrator was found to perform satisfactorily with high collection efficiency, low particle loss and low pressure drop. The experimentally determined cut-point

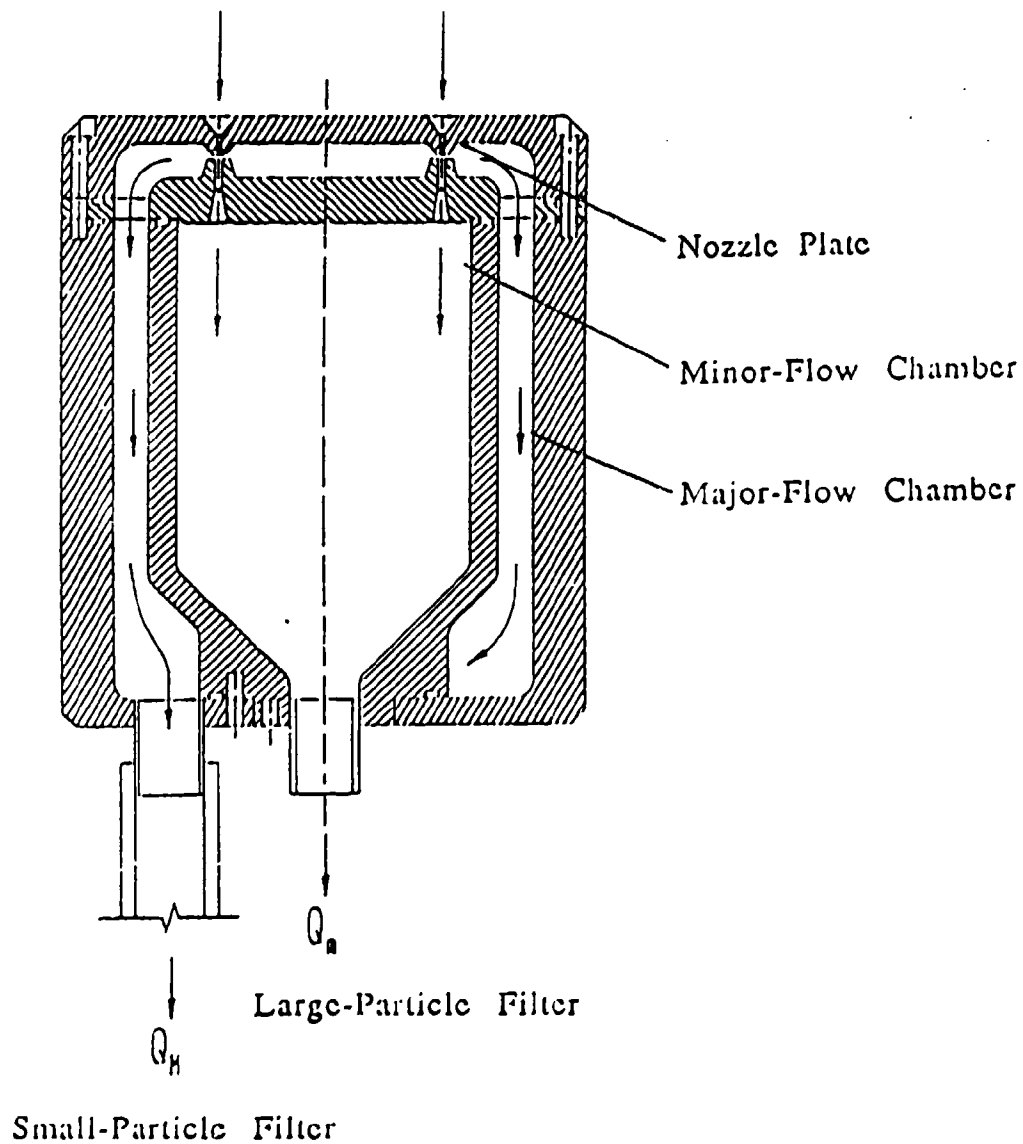


Figure 11. Virtual impactor concentrator with large particle and small particle collection filters during test to determine collection efficiency and particle loss

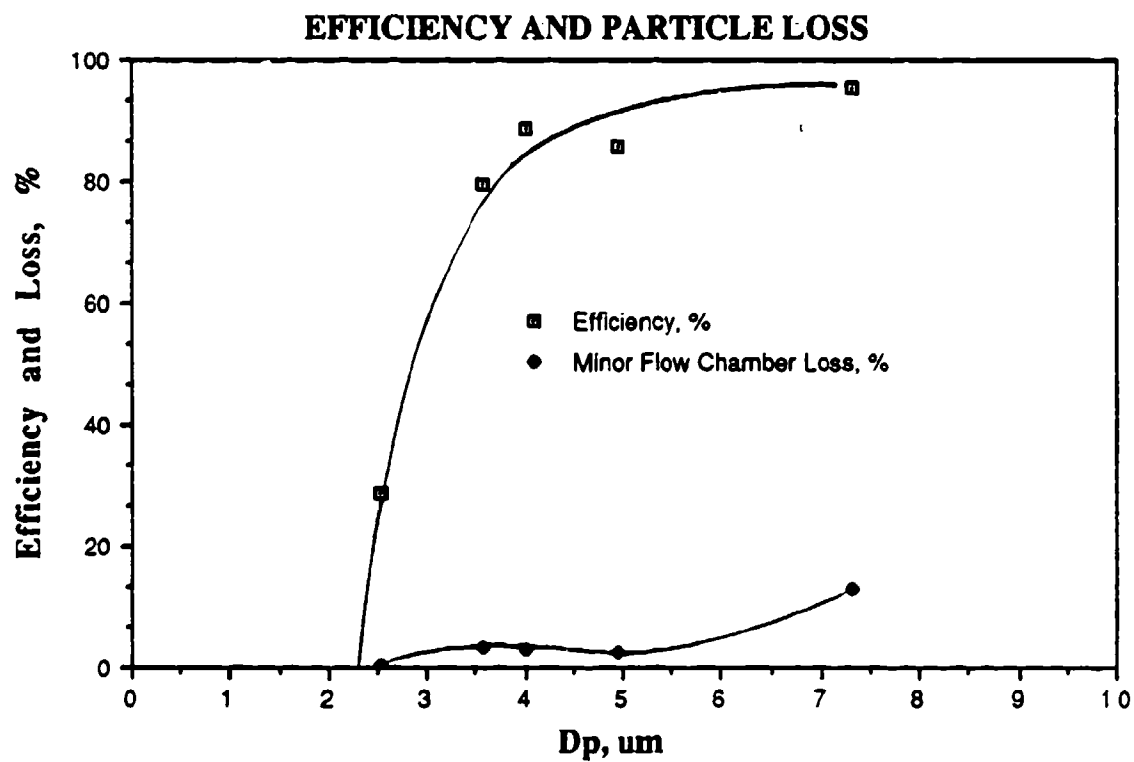


Figure 12. Collection efficiency and particle loss characteristics of virtual impactor concentrator

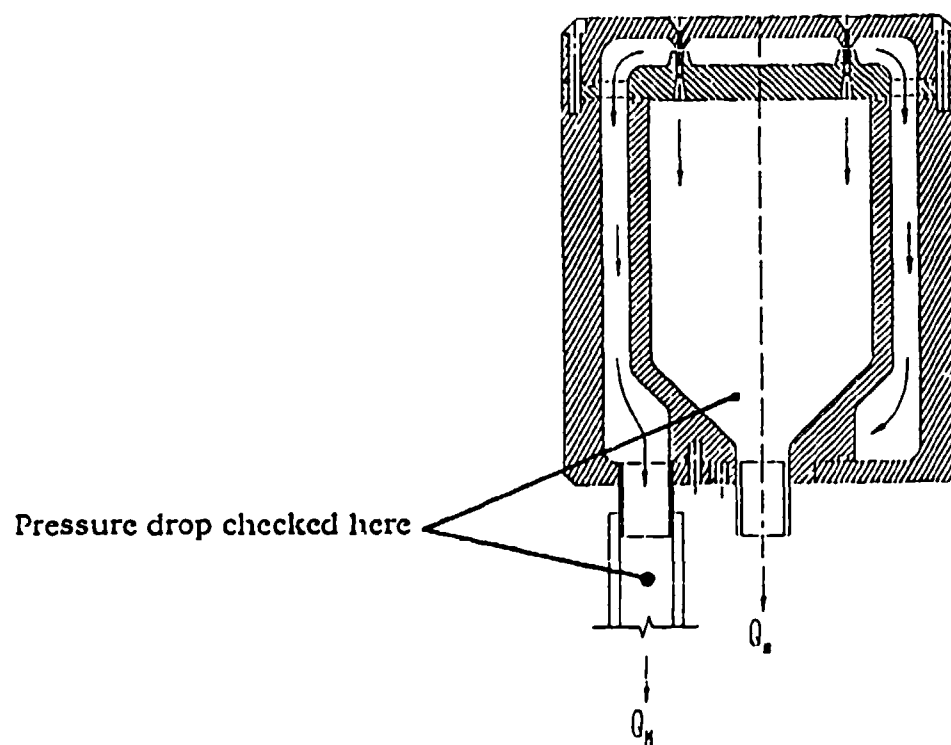


Figure 13. Virtual impactor collector during pressure drop tests, showing locations where pressure was measured

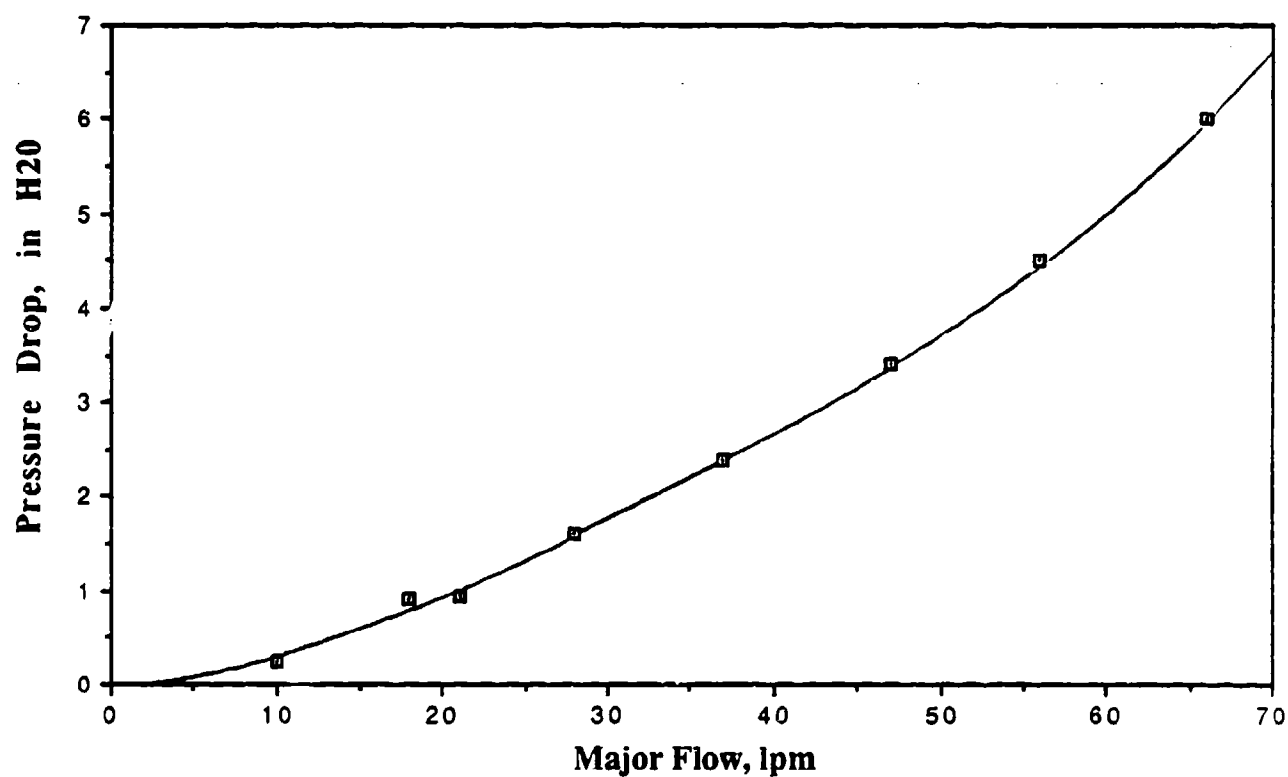


Figure 14. Pressure drop vs. flow characteristics of virtual impactor concentrator

diameter at 3.1  $\mu\text{m}$  of the concentrator was larger than intended. However, the cut-point diameter can be decreased by increasing the jet velocity. To achieve a cutpoint diameter of 2.0  $\mu\text{m}$  it is necessary to increase the jet velocity by a factor equal to the ratio of the relaxation time of the 3.1  $\mu\text{m}$  diameter particle to that of the 2.0  $\mu\text{m}$  diameter. The ratio is found to be 2.34. By increasing the total flowrate of the concentrator from 22 lpm to 51.5 lpm, the desired cutpoint can be achieved. At this flow rate, the pressure drop through the impactor would be 4.0 in.  $\text{H}_2\text{O}$ , based on the flow vs. pressure drop measurement. No other change in the design of the concentrator would be necessary.

## 5. Vaporizer/Pyrolyzer

The purpose of the vaporizer/pyrolyzer is to collect airborne particles from the concentrated aerosol stream from the virtual impactor concentrator onto a suitable substrate and then vaporize or pyrolyze the collected particles for subsequent physical or chemical analysis. Specific chemical detection techniques that can be used include mass-spectroscopic or gas chromatographic techniques. However, this project deals with the vaporizer/pyrolyzer designs only. The specific chemical analysis techniques to be used are not investigated.

### 5.1 Preliminary Experiments

Preliminary experiments were performed by means of a foil vaporizer/pyrolyzer made of nichrome foil. The physical

characteristics of the nichrome foil used in the experiments were as follows:

Resistivity:	108 $\mu\Omega/\text{cm}^3$	
Composition:	Chromium	20%
	Iron	0.5%
	Silicon	1.0%
	Nickel	78.5%

Dimensions:

0.25" x 1.0" x 0.001" (Width x length x thickness)

The material was obtained from Hoskins Manufacturing Co. (4445 Lawton Ave., Detroit, Michigan 48208) and the foil was mounted on supporting electrodes. The completed unit was found to have an electrical resistance of 0.345  $\Omega$ .

The electrical and thermal characteristics of the foil vaporizer/pyrolyzer was determined by connecting a low voltage DC power supply to the evaporator and measuring the electrical current and the temperature of the foil as the voltage is varied. The power supply used has a voltage range of 0 - 36 Volts and current range of 0-10 Amperes. The foil temperature was measured by welding a thermocouple to the surface of the foil and measuring the thermocouple output directly with a temperature indicator. The experimental data are summarized in Table 1 and the results are plotted in Figures 15 and 16 for the voltage vs. current and power vs. temperature relationships. It is interesting to note that the foil is able to achieve a temperature of 700  $^{\circ}\text{C}$  with an input power of 28 Watts.

**Table 1: Electrical and Thermal Characteristics of Foil Vaporizer/Pyrolyzer**

I, Ampere	V, Volt	W, Watt	T, °C
0.0	0.00	0.00	25
1.0	0.34	0.34	50
2.0	0.69	1.38	94
3.0	1.01	3.03	145
4.0	1.38	5.52	205
5.0	1.72	8.60	290
6.0	2.07	12.48	398
7.0	2.44	17.08	510
8.0	2.76	22.08	615
9.0	3.11	27.98	700

**Table 2: Vaporization Spectrum for 4  $\mu$ L of 0.1% DOP**

W, Watt	T, °C	#/cc	
		Run 1	Run 2
2.09	130	18	34
3.83	170	$3.9 \times 10^4$	$2.6 \times 10^3$

The performance of the vaporizer/pyrolyzer was evaluated using the experimental system shown in Figure 17. Here the vaporizer/pyrolyzer is mounted inside a small glass bottle and filtered air at 24 or 12 lpm is introduced into the bottle to flush out the vaporized or pyrolyzed material. A TSI 3760 condensation nucleus counter (CNC) is used to monitor the particles in the output air stream. Since the CNC is capable of detecting particles as small as  $0.01\text{ }\mu\text{m}$ , the system proves to be extremely sensitive for detecting the small amounts of vaporized or pyrolyzed material from the vaporizer/pyrolyzer.

Foil Cleaning: For the purpose of cleaning the foil, the vaporizer/pyrolyzer was immersed in denatured alcohol for about one hour and then dried in an oven. The assembly was then installed in the system. Next, 23 watts of power was applied so that all material that would be vaporized or pyrolyzed below this power level would be vaporized or pyrolyzed. Finally,  $4\text{ }\mu\text{L}$  of denatured alcohol was added to the foil. The foil was then heated with 23 w of power. No CNC count was observed, indicating that the foil was in fact clean and that the alcohol used was nearly impurity free.

Vaporization Spectrum: To determine the response of the vaporizer/pyrolyzer, a solution was prepared by adding 0.1% of DOP (di-octyl phthalate) by volume to the denatured alcohol solvent.  $4\text{ }\mu\text{L}$  of this 0.1% DOP (di-octyl phthalate) solution was then added to the foil. The electrical current was then slowly increased. When the CNC began to indicate a count, the current increase was stopped and the current was maintained at that level until the CNC count rose to a peak and then decayed to zero. The current was then slowly

increased and the above steps repeated until all current levels at which counts were observed were determined.

Figure 18 shows a sample spectrum obtained with 4  $\mu\text{L}$  of 0.1% DOP. It is interesting to note that two peaks were observed at power levels of 2.09 W and 3.83 W, corresponding to temperature levels of approximately 110 and 170  $^{\circ}\text{C}$ . At these temperature levels, materials in the DOP were vaporized and recondenses to form an aerosol, which is then detected by the CNC. The detailed data are given in Table 2.

Flash Vaporization: For the flash vaporization tests, 2, 4 or 8  $\mu\text{L}$  of the sample solution was added to the vaporizer/pyrolyzer and 12 W of power was applied to the foil vaporizer/pyrolyzer suddenly. Power was maintained at this level and aerosol particle counts were recorded by the CNC. The results obtained for the 0.1% DOP are shown in Table 3. It is interesting to note that the peak concentration detected is approximately proportional to the solution volume added to the foil, indicating a linear relationship between vaporized material and peak aerosol concentration detected.

## 5.2 Results

DOS: Experiments were performed using both solutions of known impurity content as well as solutions with unknown impurity content. Figure 19 shows the spectrum obtained with 4  $\mu\text{L}$  of 0.1% DOS (di-octyl sebacate) in denatured alcohol. The spectrum is quite similar to that for DOP with the second peak occurring at a power level somewhat lower than that for DOP (3.32 W for DOS vs. 3.83 W

**Table 3: Flash Vaporization for 0.1% DOP**

Volume, $\mu\text{L}$	#/cc	
	Run 1	Run 2
2	$2.2 \times 10^4$	$2.4 \times 10^4$
4	$6.2 \times 10^4$	$6.2 \times 10^4$
8	$1.2 \times 10^5$	$8.9 \times 10^4$

**Table 4: Vaporization Spectrum for 4  $\mu\text{L}$  of 0.1% DOS**

W, Watt	T, $^{\circ}\text{C}$	#/cc	
		Run 1	Run 2
2.04		$3.1 \times 10^4$	$4.5 \times 10^4$
3.32		$2.1 \times 10^4$	$3.6 \times 10^2$

**Table 5: Flash Vaporization for 0.1% DOS**

Volume, $\mu\text{L}$	#/cc	
	Run 1	Run 2
2	$3.2 \times 10^4$	$3.0 \times 10^4$
4	$4.6 \times 10^4$	$5.3 \times 10^4$
8	$7.0 \times 10^5$	$6.7 \times 10^4$

for DOP). The data are given in Table 4. The results for the flash vaporization tests are given in Table 5.

De-ionized Water: To test the impurity in de-ionized water, two grades of de-ionized water was used. One of the de-ionized water tested was known to be of high-quality with electrical resistivity in the vicinity of 18 M $\Omega$ . The second de-ionized water was considerably lower in quality, with much lower, but unknown electrical resistivity. The results are shown in Figure 20. In both cases, one peak was observed at a power level in the vicinity of 13 W. The result for the flash vaporization test is shown in Table 6.

Tap Water: When tap water from the laboratory faucet was used, interesting and complicated spectra was observed. Figure 21 shows the spectrum for the tap water. A total of six peaks were observed corresponding to the various unknown impurities in the tap water. The results are given in more detail in Table 7. The corresponding data for the flash vaporization test are given in Table 8.

Finger Print: When the foil vaporizer/pyrolyzer surface is lighted touched by the finger, there is sufficient contamination to give interesting and easily observed peaks. The results are shown in Figure 22 and in Tables 9 and 10.

The above experimental results are compared and summarized in Table 11. The highest particle count is obtained with DOP where 4  $\mu$ L of 0.1% of DOP produced the highest count of  $6 \times 10^4$  particles/cc. Lightly touching the foil surface with the tip of the finger produced counts that are of the same order of magnitude. On the other hand, when high purity DI water was used, the counts obtained was

**Table 6: Flash Vaporization of De-ionized Water**

Run	#/cc	
	High Purity	Low Purity
1	0.054	3.732
2	0.193	0.508
3	0.610	0.447
4	0.054	3.808
5	0.060	1.040
Mean	0.194	1.905

**Table 7: Vaporization Spectrum for Tap Water**

W, Watt	T, °C	#/cc	
		Run 1	Run 2
3.04	142	0.265	0.803
4.10	176	1.71	1.342
5.36	202	0.162	0.521
8.77	300	0.017	0
14.02	440	$1.197 \times 10^3$	$1.15 \times 10^3$
19.59	580	$1.070 \times 10^4$	$2.26 \times 10^2$

Table 8: Flash Vaporization of 4  $\mu$ L of Tap Water

Run	#/cc
1	$2.40 \times 10^4$
2	$2.39 \times 10^4$
3	$2.82 \times 10^4$
Mean	$2.54 \times 10^4$

Table 9: Vaporization Spectrum for Finger Print

W, Watt	T, °C	#/cc	
		Run 1	Run 2
2.67		$2.85 \times 10^2$	$5.07 \times 10^2$
3.02		$6.77 \times 10^2$	$9.29 \times 10^4$
3.90		$7.24 \times 10^4$	$3.38 \times 10^4$
5.28		$4.82 \times 10^1$	1.905
17.97		$6.47 \times 10^3$	$9.65 \times 10^2$
21.44		0.241	1.809

**Table 10: Flash Vaporization of Finger Print**

Run	#/cc
1	$4.95 \times 10^4$
2	$5.80 \times 10^4$
3	$1.78 \times 10^5$
4	$1.44 \times 10^5$
Mean	$1.07 \times 10^5$

**Table 11: Typical CNC Count (#/cc) for Various Materials**(4  $\mu$ L sample Volume, except finger print)

Material	#/cc
0.1% DOP	$6 \times 10^4$
0.1% DOS	$5 \times 10^4$
Tap Water	$2.5 \times 10^4$
DI Water (high purity)	0.194
DI Water (low purity)	1.90
Finger Print	$1 \times 10^4$

approximately 5 orders of magnitude lower, and in the vicinity of 0.19 particles/cc.

### 5.3 Vaporizer/Pyrolyzer for the Virtual Impactor Concentrator

On the basis of the experimental work described above, a vaporizer/pyrolyzer was designed and constructed for the virtual impactor concentrator described earlier. The conceptual design of the vaporizer/pyrolyzer is shown in Figure 23 and a more detailed design is shown in Figure 24.

Specifically, the vaporizer/pyrolyzer consists of a needle-in-a-tube electrostatic precipitator to precipitate the particles in the concentrator aerosol stream from the virtual impactor concentrator. The particle collecting surface is in the form of a tight cylindrical helix wound from nichrome heating wires. The helical coil of nichrome wire provide the collecting surface onto which particles can precipitate. After sufficiently amounts of material has been collected, an electrical current can then be passed through the nichrome wire to cause the material to be vaporized or pyrolyzed. The vaporized or pyrolyzed material can then be introduced into a mass spectrometer for physical or chemical analysis. This particular design of the vaporizer/pyrolyzer has the advantage that the electrostatic precipitator designed has high collecting efficiency and the small mass of the nichrome wire results in short thermal time constant and rapid heating of the collected sample. In addition, since particles are collected on the nichrome wire by electrostatic charging and precipitation, particles would be attracted to the collecting surface and bounce and re-entrainment of particles are unlikely to occur.

This particular design is specifically recommended for further research and development effort.

6. Summary of Important Results

The result of this study indicates that sample acquisition for chemical or biological detection can best be accomplished by the use of a multiple nozzle virtual impactor concentrator to concentrate the aerosol stream and an electrostatic precipitator to deposit the particles onto the surface of a nichrome wire to volatilize or pyrolyze the collected material for subsequent physical or chemical identification. The use of a multiple nozzle virtual impactor concentrator will lead to significant savings in pressure drop and power consumption for the sample flow pump. The use of an electrostatic precipitator will provide high collection efficiency and avoid the problem of particle bounce. A sample acquisition system incorporating the above mentioned elements has been designed, constructed and tested. The performance characteristics of the system have been found to be satisfactory.

7. Participating Scientific Personnel

Virgil Marple, Benjamin Liu, Bernard Olson and Steven Behm

8. Bibliography

Burglund, R. N. and B. Y. H. Liu (1973), "Generation of Monodisperse Aerosol Standards," Environ. Sci. Technol. 7:147.

Gousman, A. D., W. M. Pun, A. K. Runchal, D. B. Spalding and M. Wolfshtein (1969) Heat and Mass Transfer in Recirculating Flows, Academic Press, New York.

Marple, V. A. and C. M. Chien, (1980) "Virtual Impactors: Theoretical Study," Environ. Sci. Technol. 14:976 .

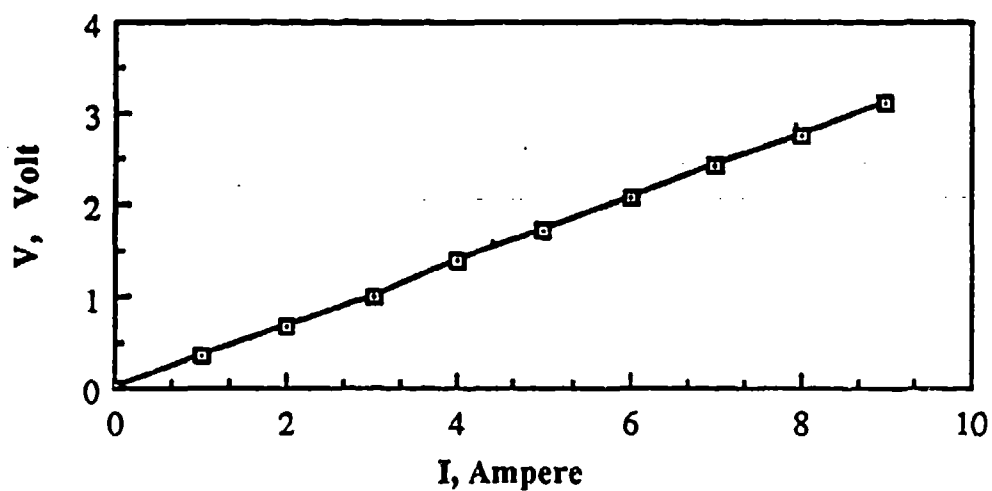


Figure 15. Voltage-current curves for foil vaporizer/pyrolyzer

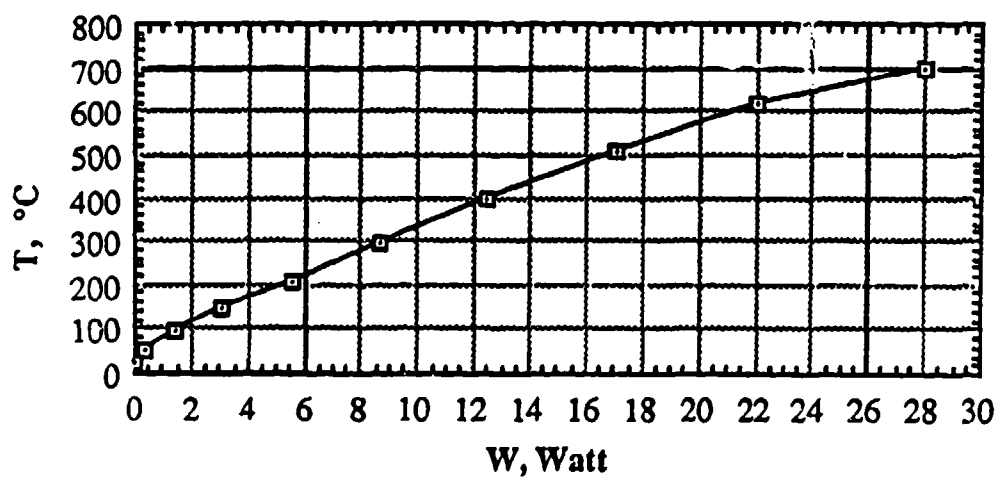


Figure 16. Foil temperature as a function of input power

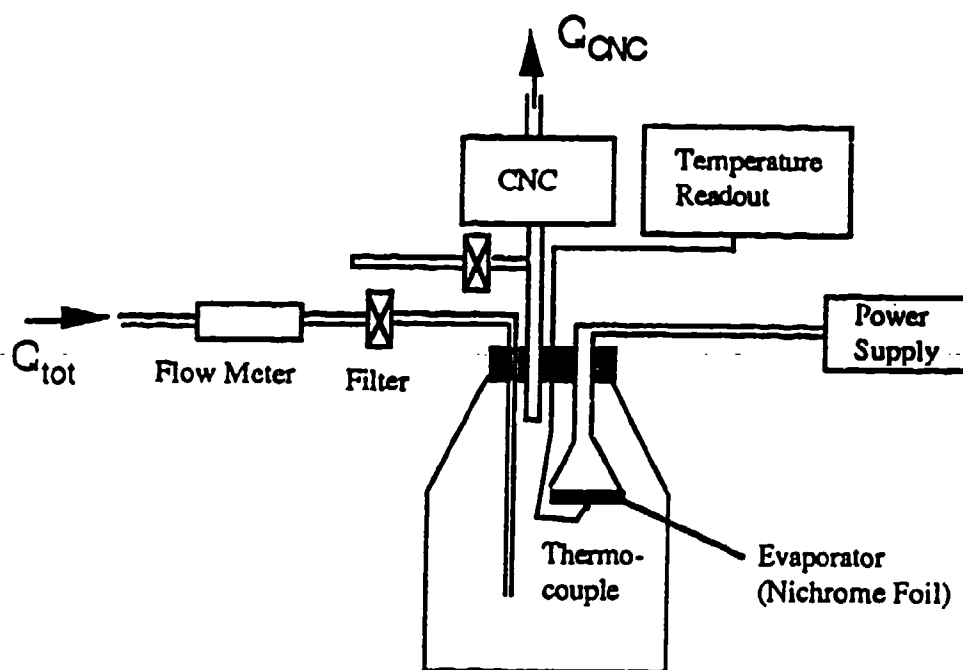


Figure 17. Experimental system for evaluating foil vaporizer/pyrolyzer

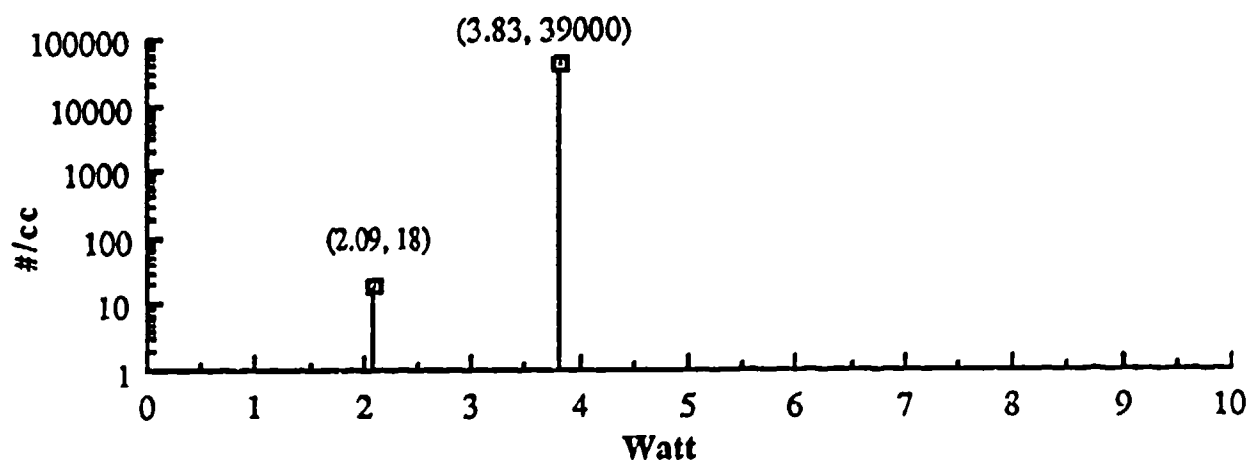


Figure 18. Vaporization spectrum for 4  $\mu$ L of 0.1% DOP solution

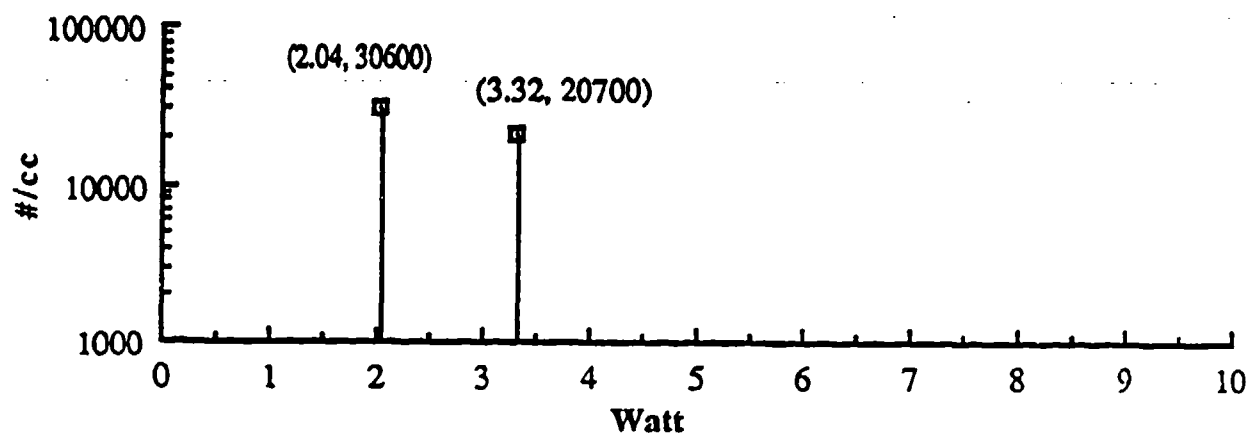


Figure 19. Vaporization spectrum for 4  $\mu\text{L}$  of 0.1% DOS solution

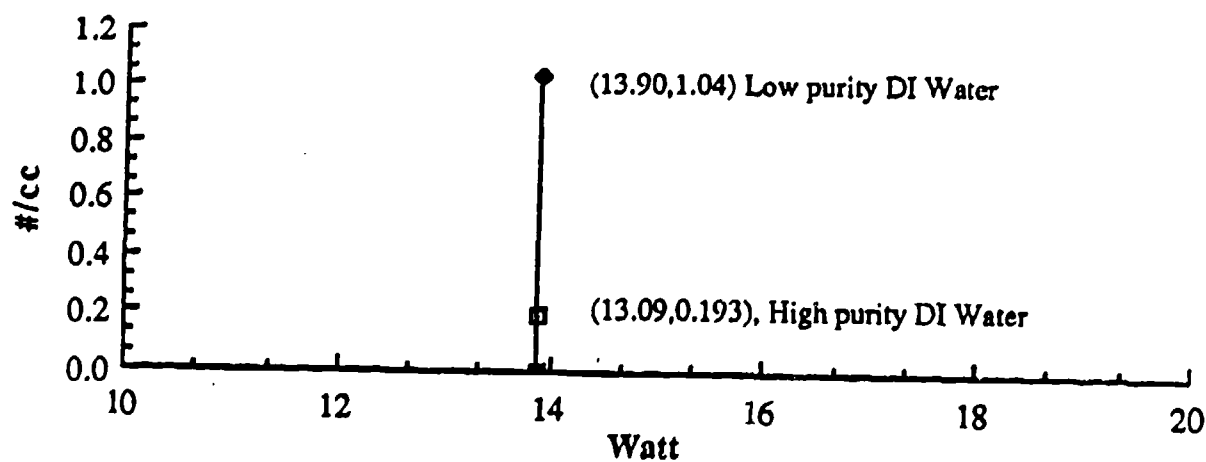


Figure 20. Vaporization spectrum for de-ionized water of high and low purity

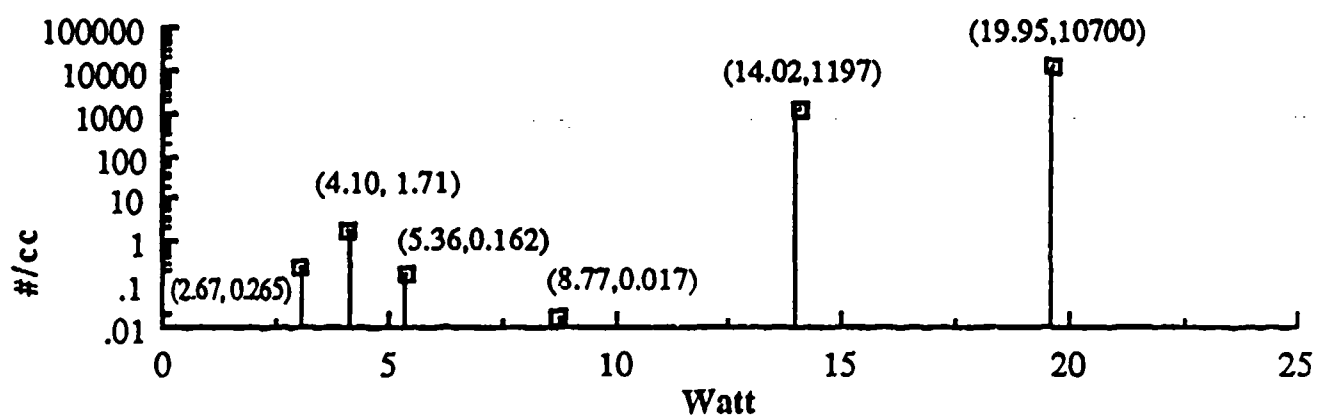


Figure 21. Vaporization spectrum for ordinary tap water

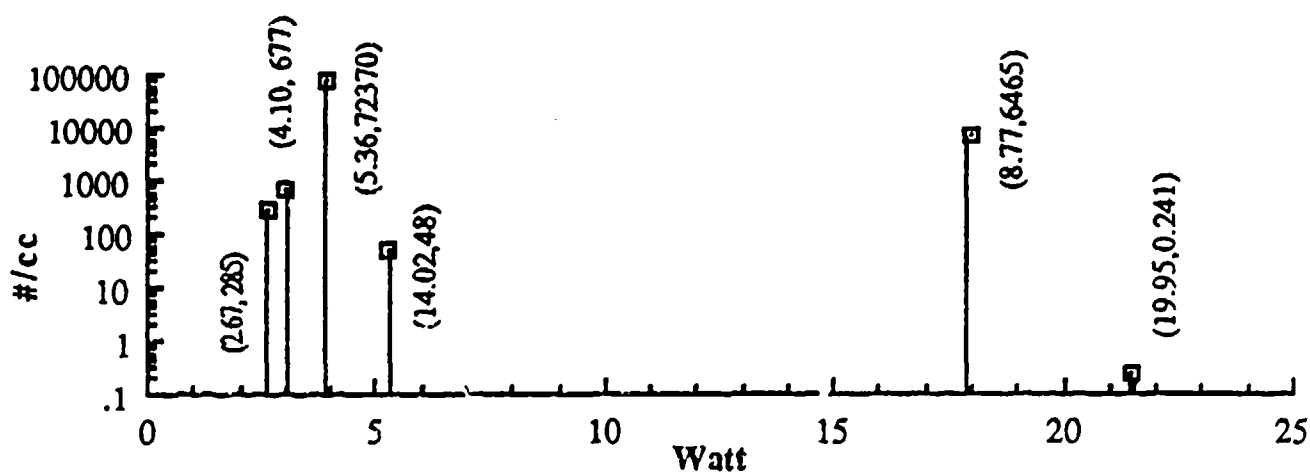


Figure 22. Vaporization spectrum for finger print

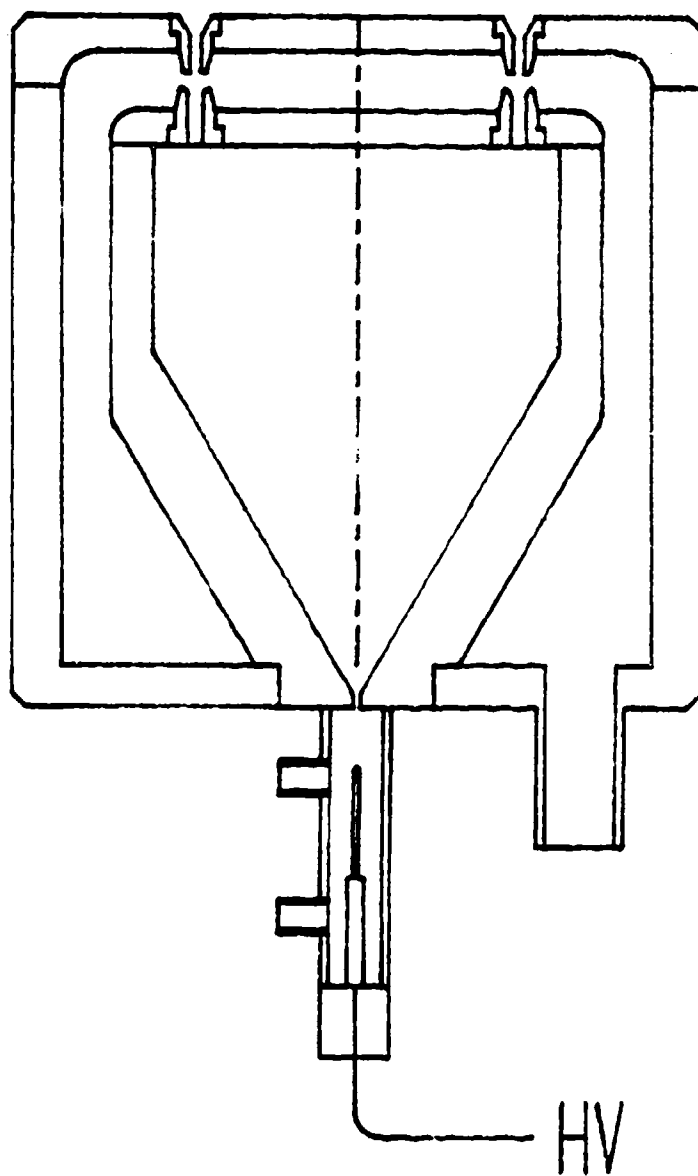


Figure 23. Conceptual design of electrostatic precipitator for particle collection

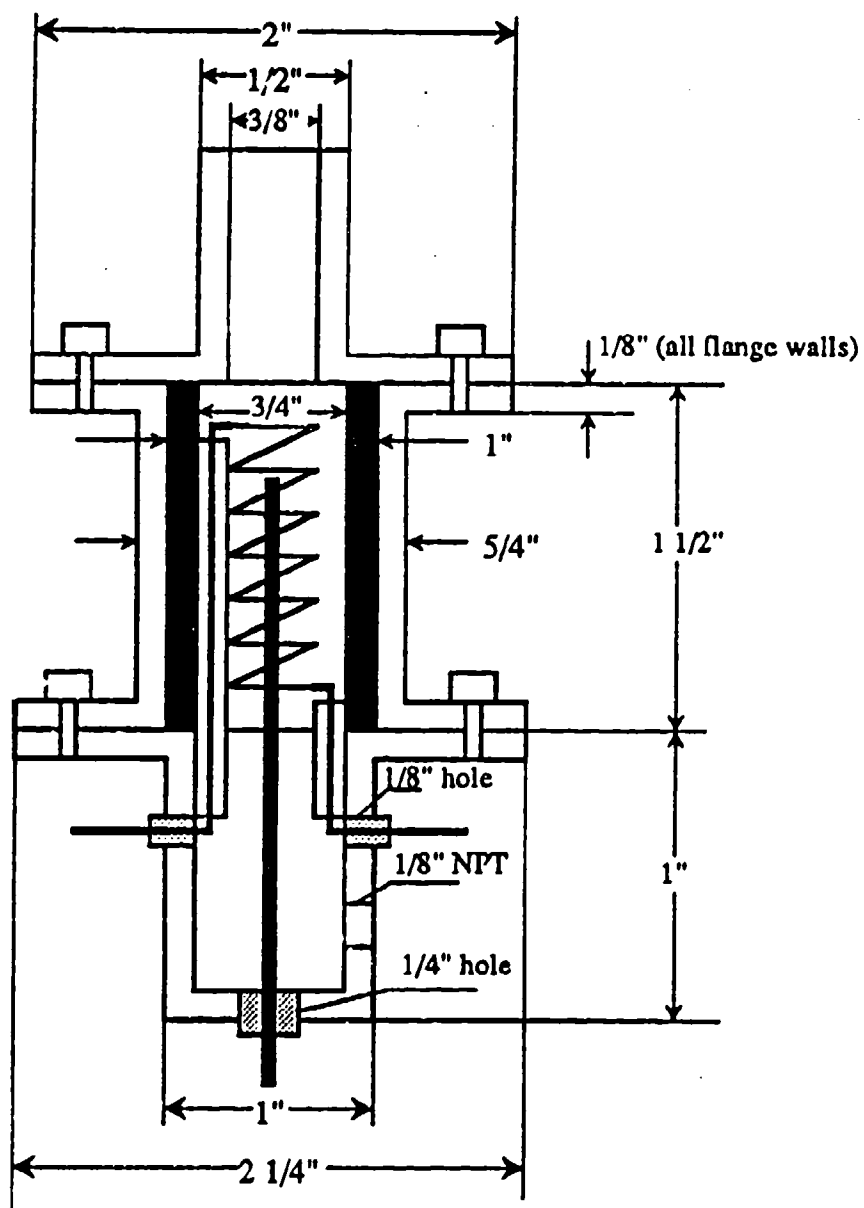


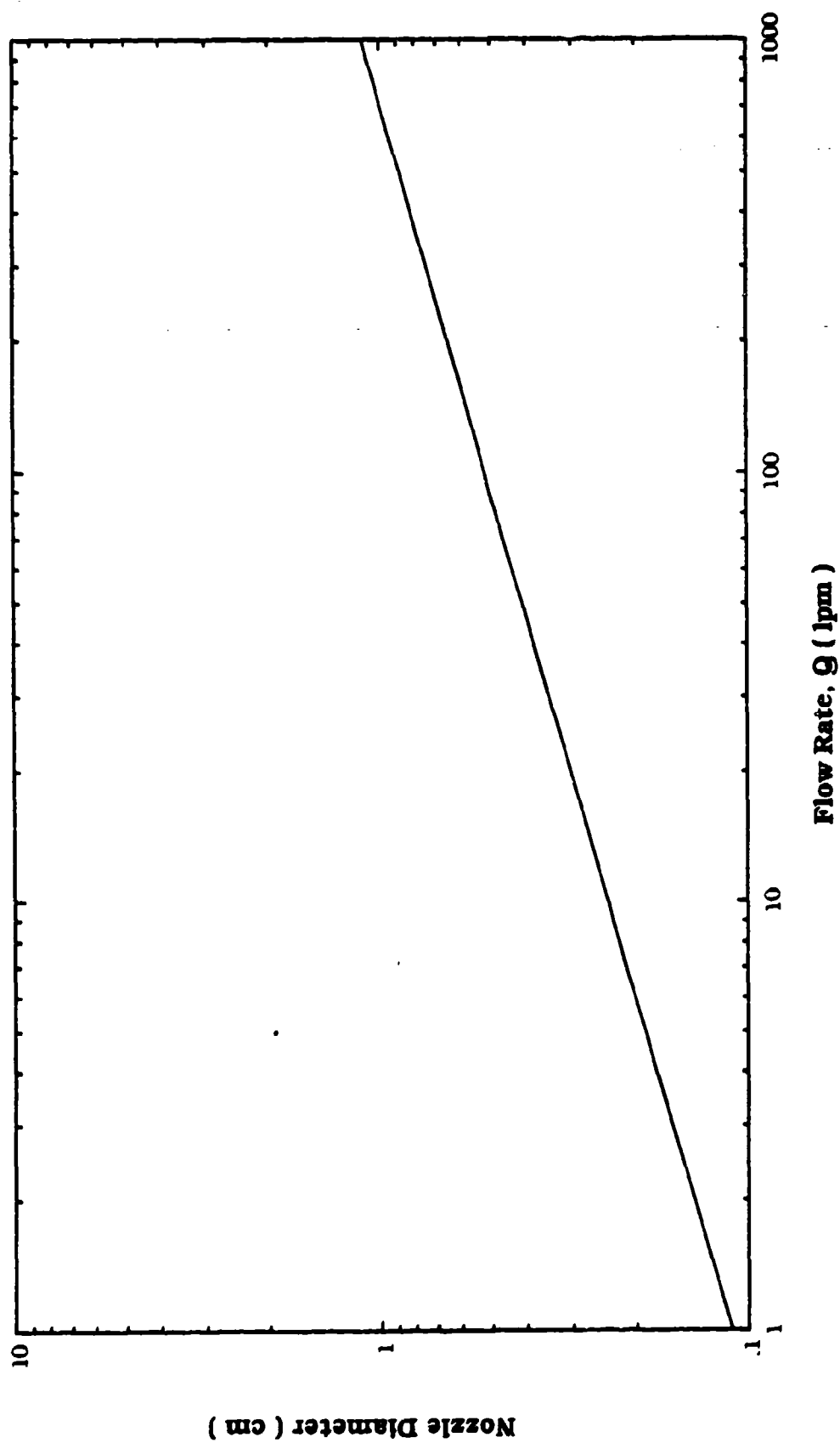
Figure 24. Design of electrostatic precipitator, vaporizer/pyrolyzer

## Appendix A

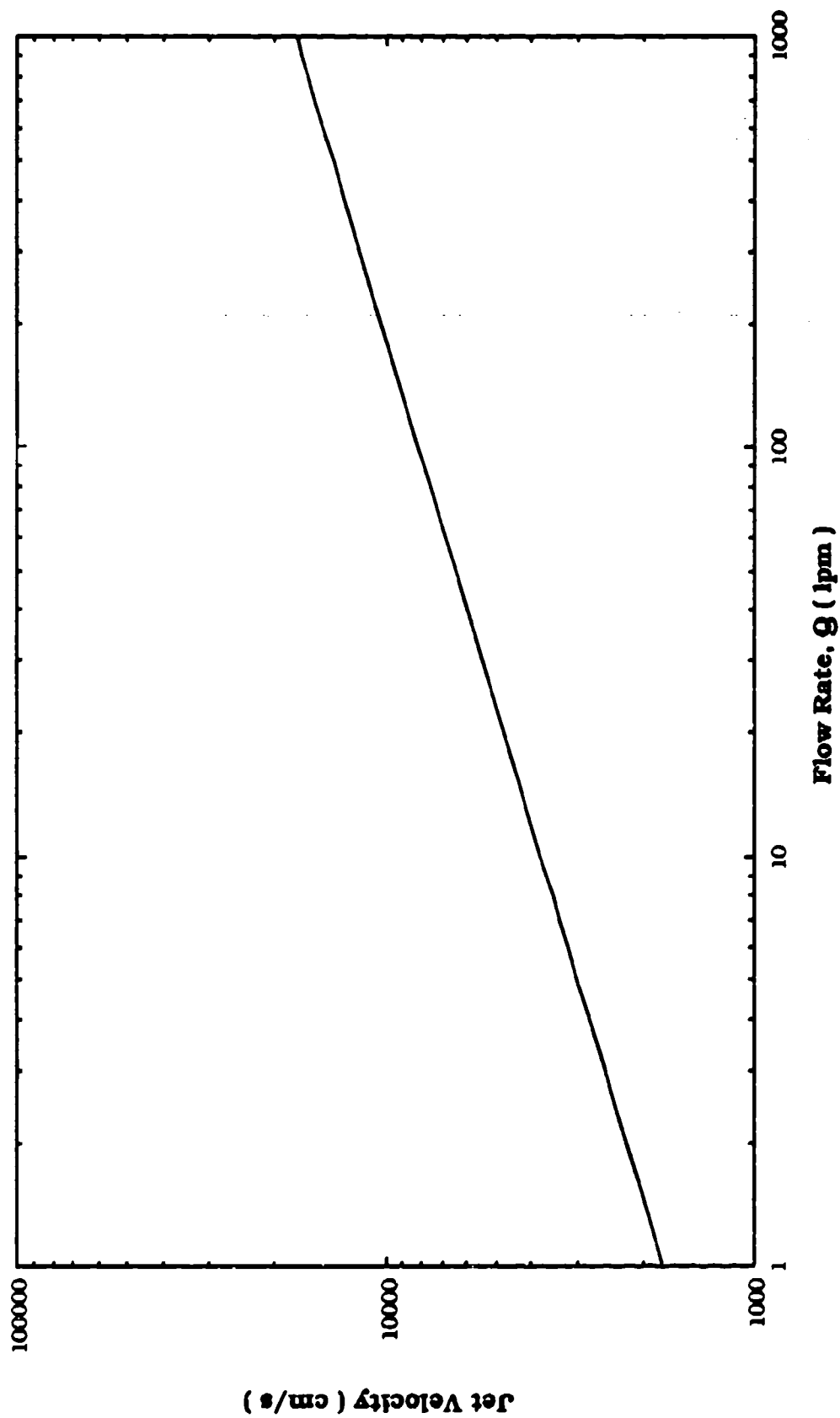
### Performance of the Single Nozzle Virtual Impactor Concentrator



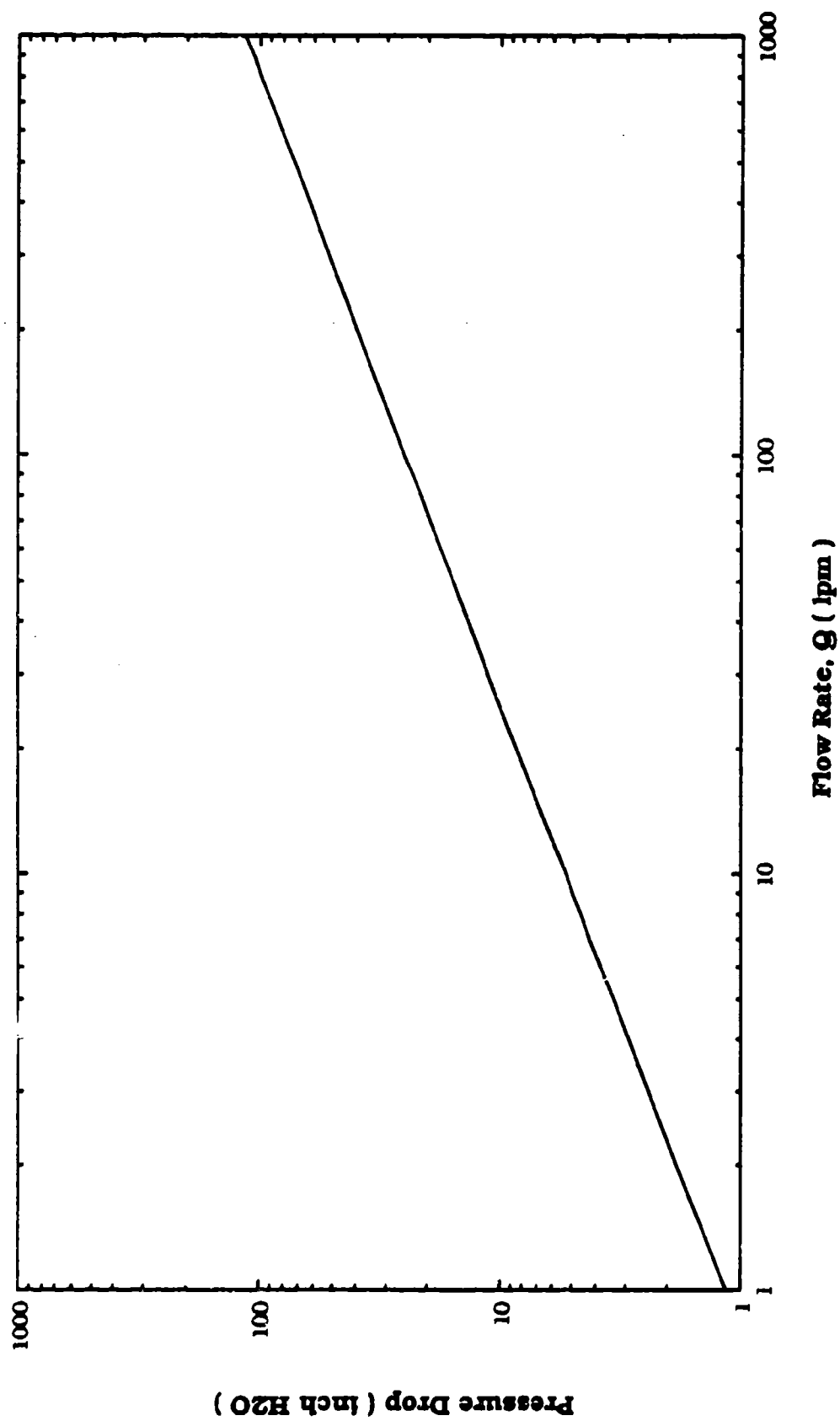
# Single Nozzle Virtual Impactor Concentrator



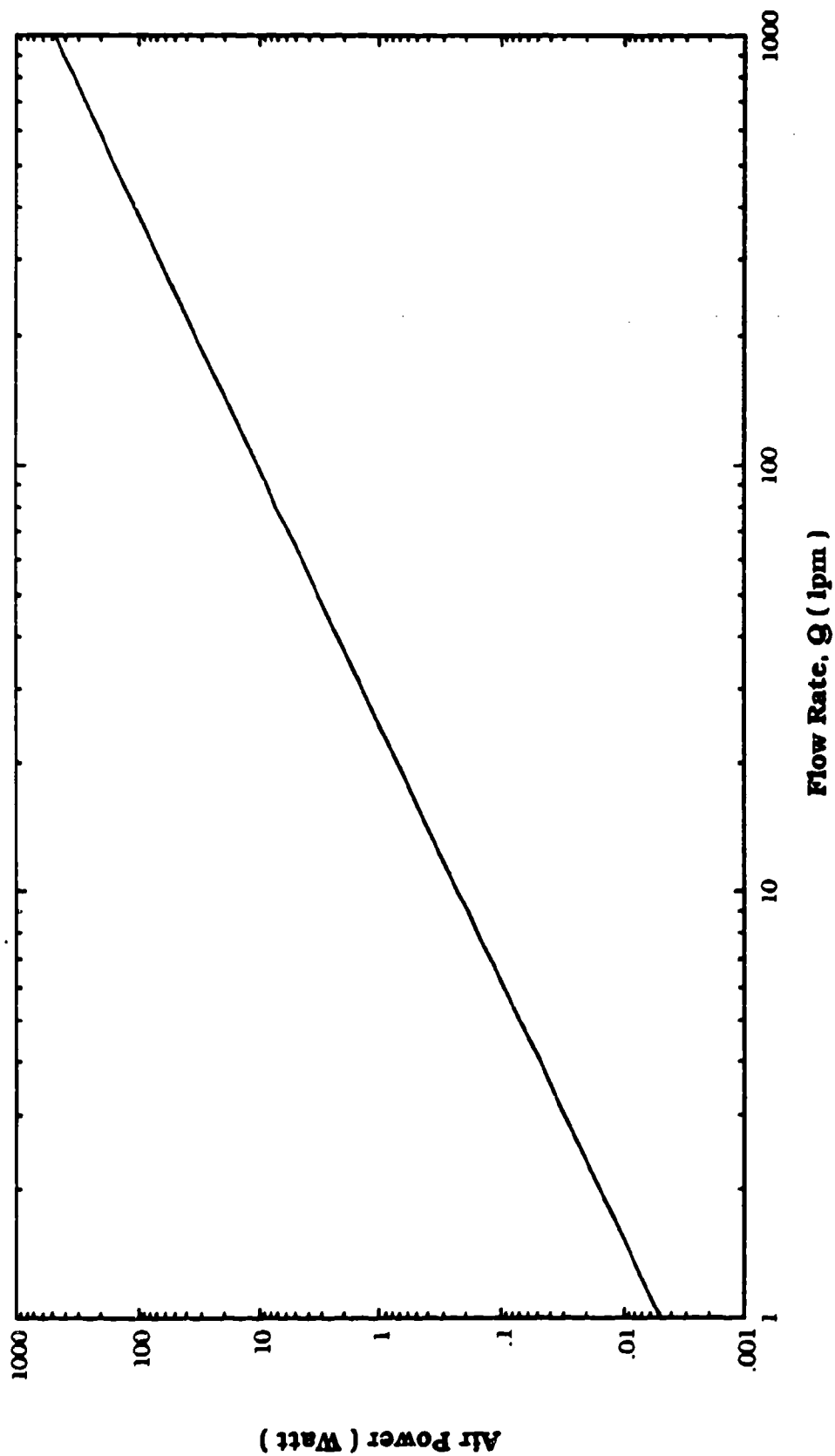
# Single Nozzle Virtual Impactor Concentrator



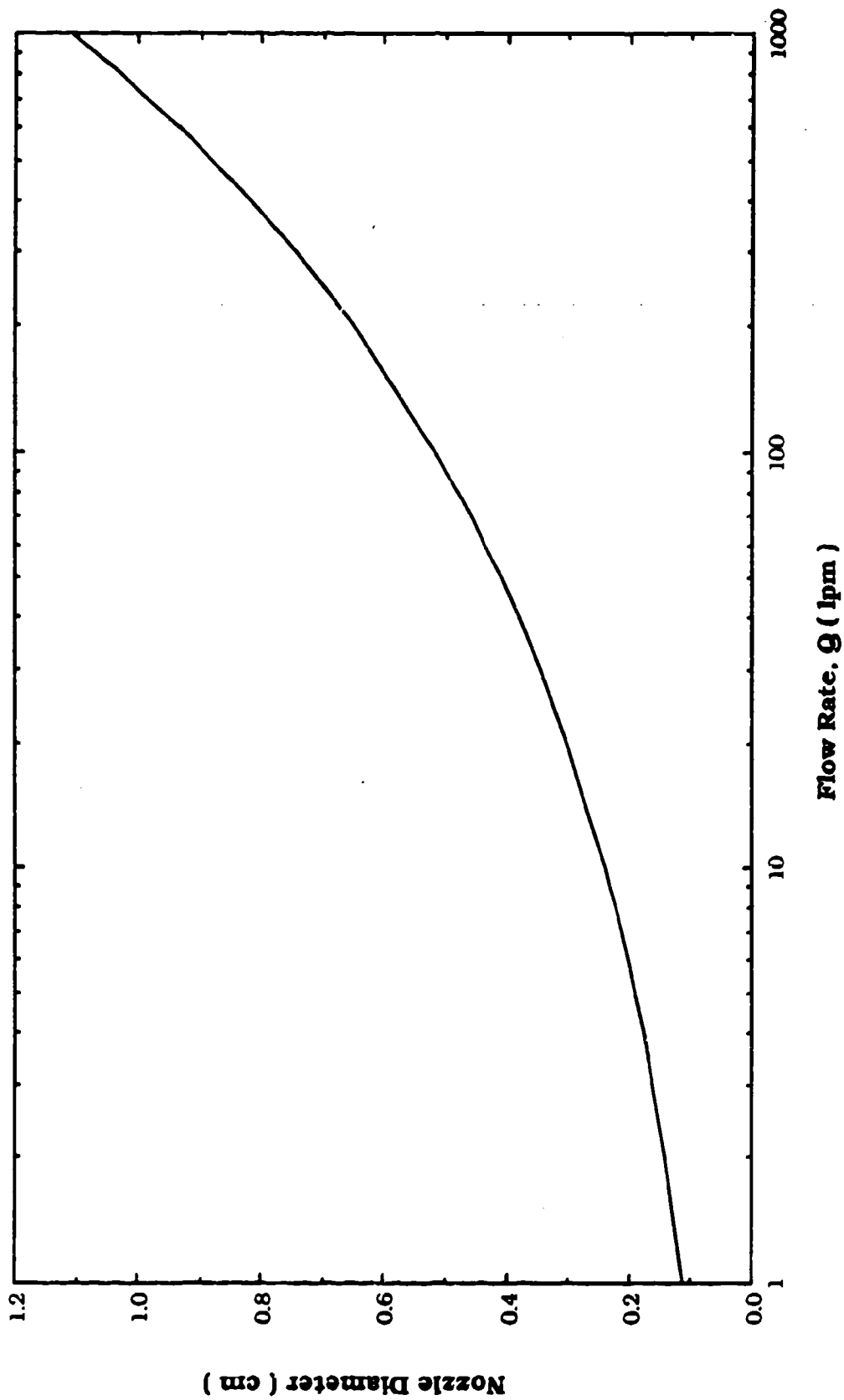
### Single Nozzle Virtual Impactor Concentrator



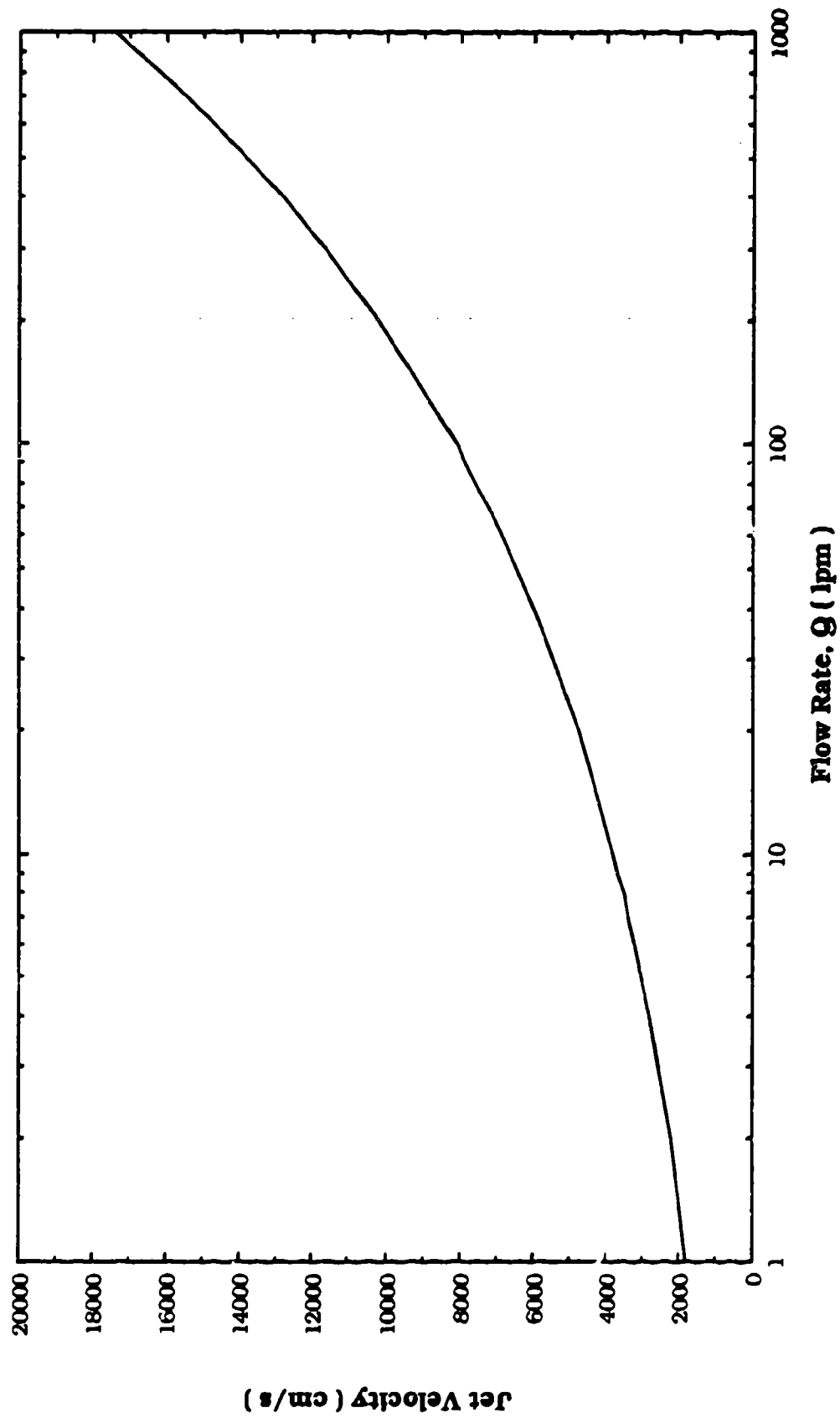
# Single Nozzle Virtual Impactor Concentrator



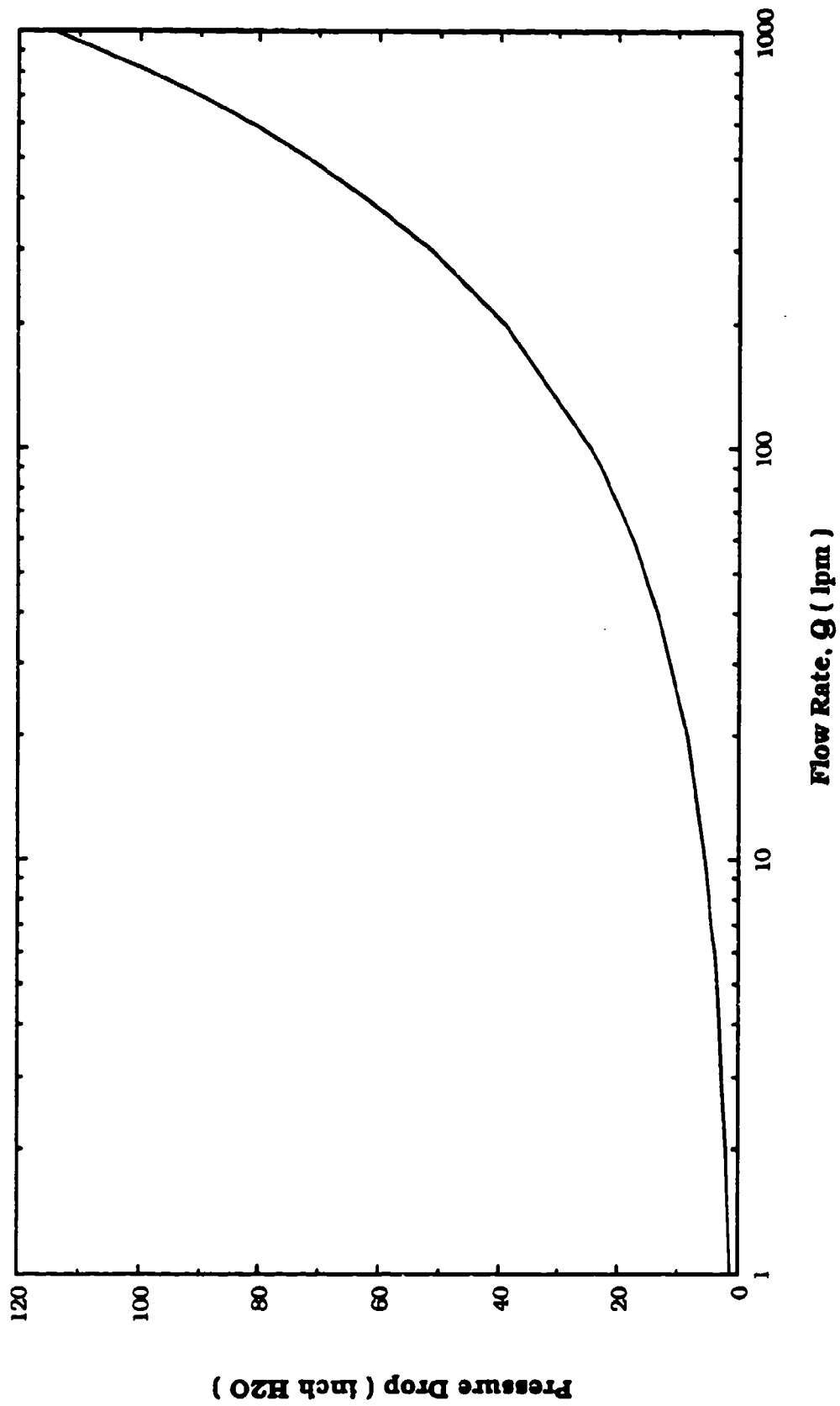
# Single Nozzle Virtual Impactor Concentrator



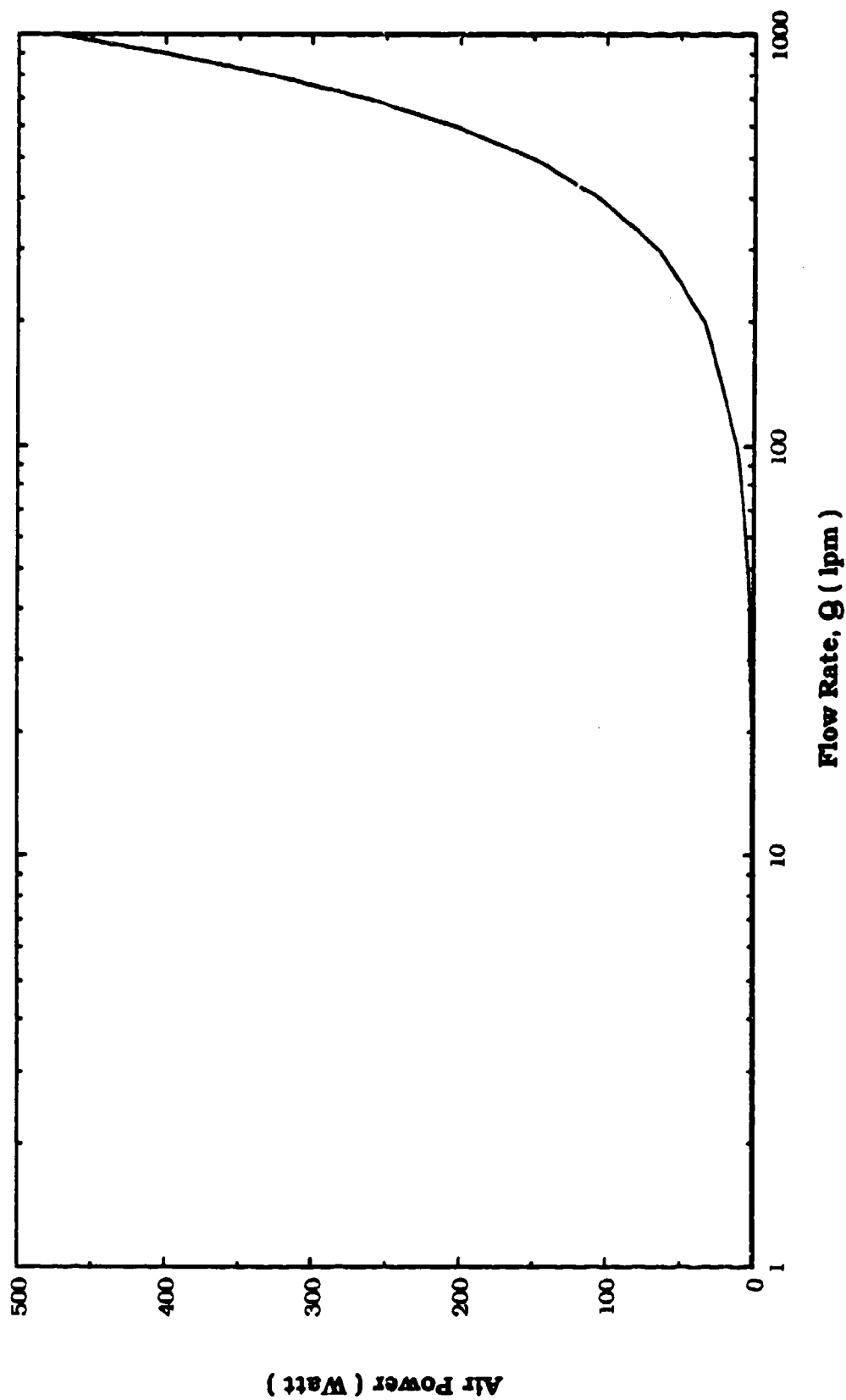
### Single Nozzle Virtual Impactor Concentrator



### Single Nozzle Virtual Impactor Concentrator



### Single Nozzle Virtual Impactor Concentrator

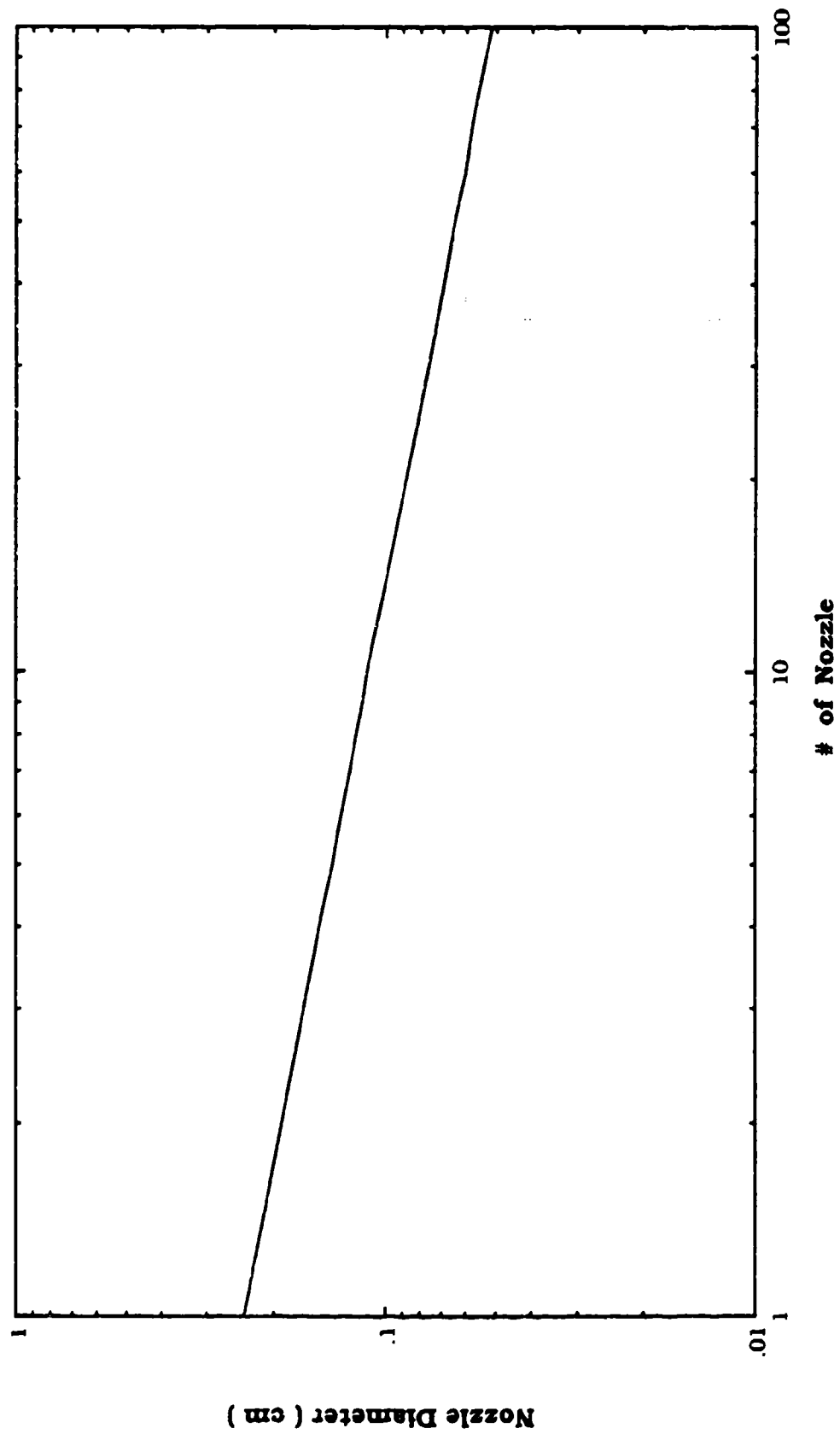


## Appendix B

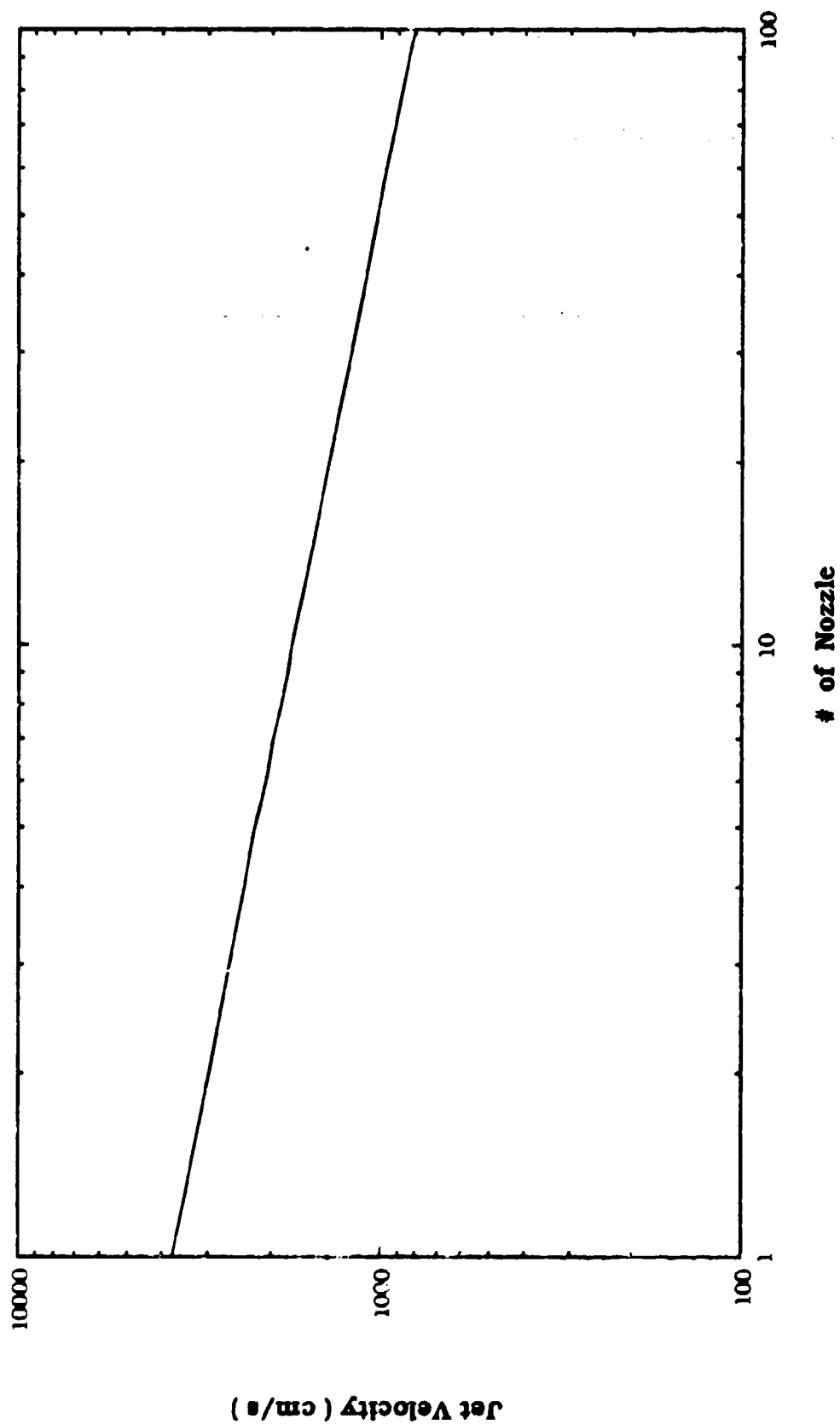
Performance of the Multiple Nozzle Virtual Impactor Concentrator  
with Sampling Flow Rates of 10, 100, 1000 and 22 Liters per Minute



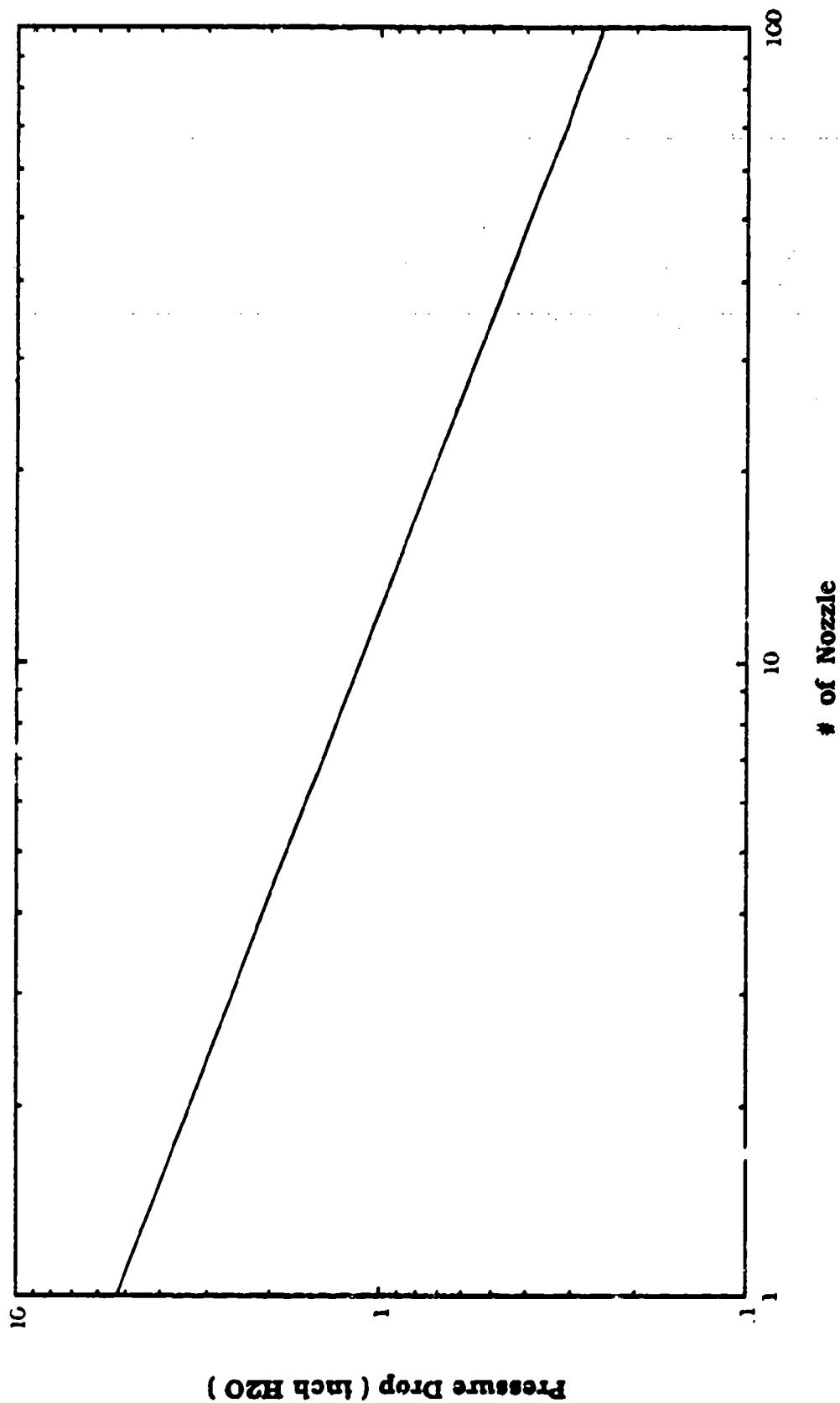
# Multiple Nozzle Virtual Impactor Concentrator ( $Q = 10 \text{ lpm}$ )



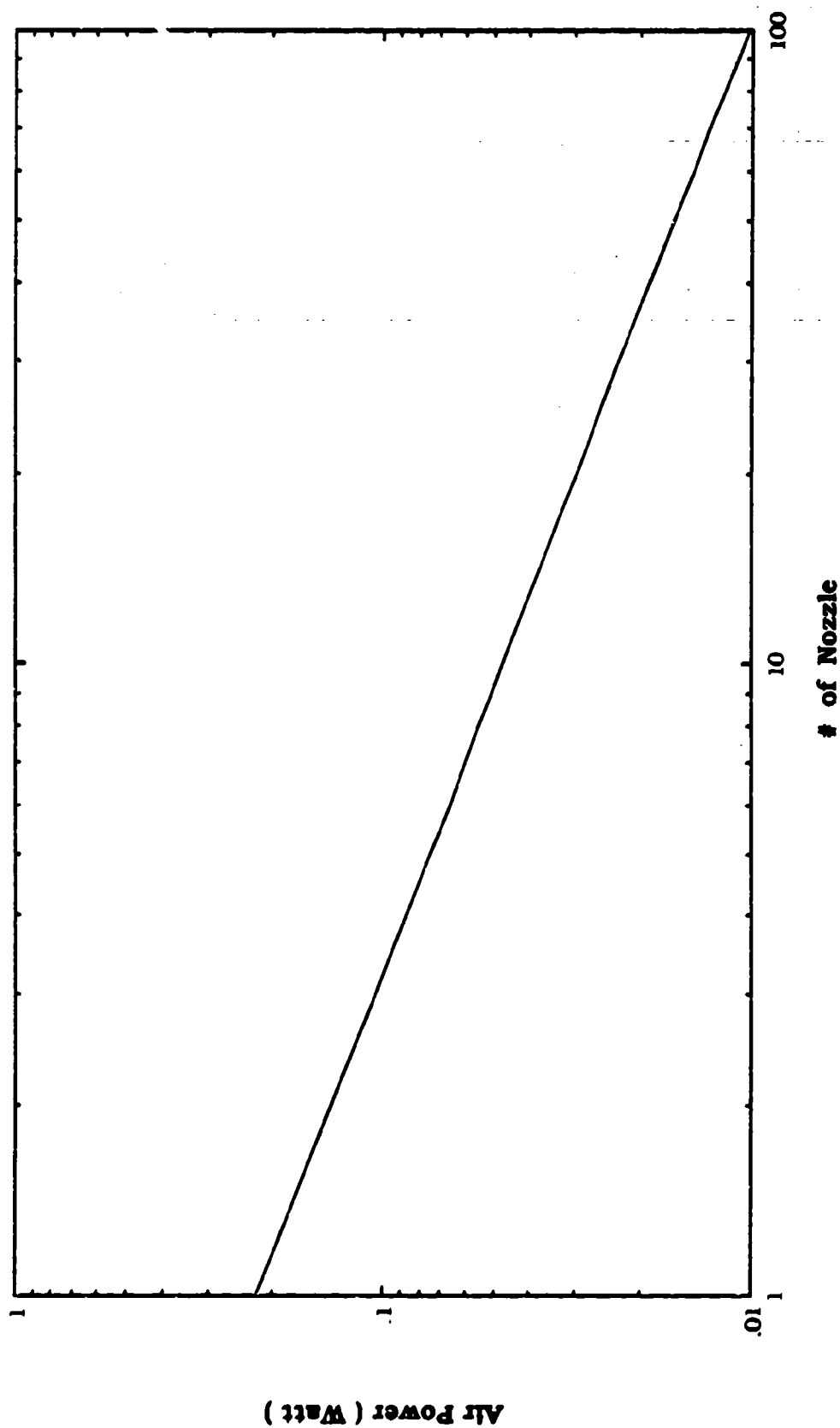
Multiple Nozzle Virtual Impactor Concentrator (  $Q = 10 \text{ lpm}$  )



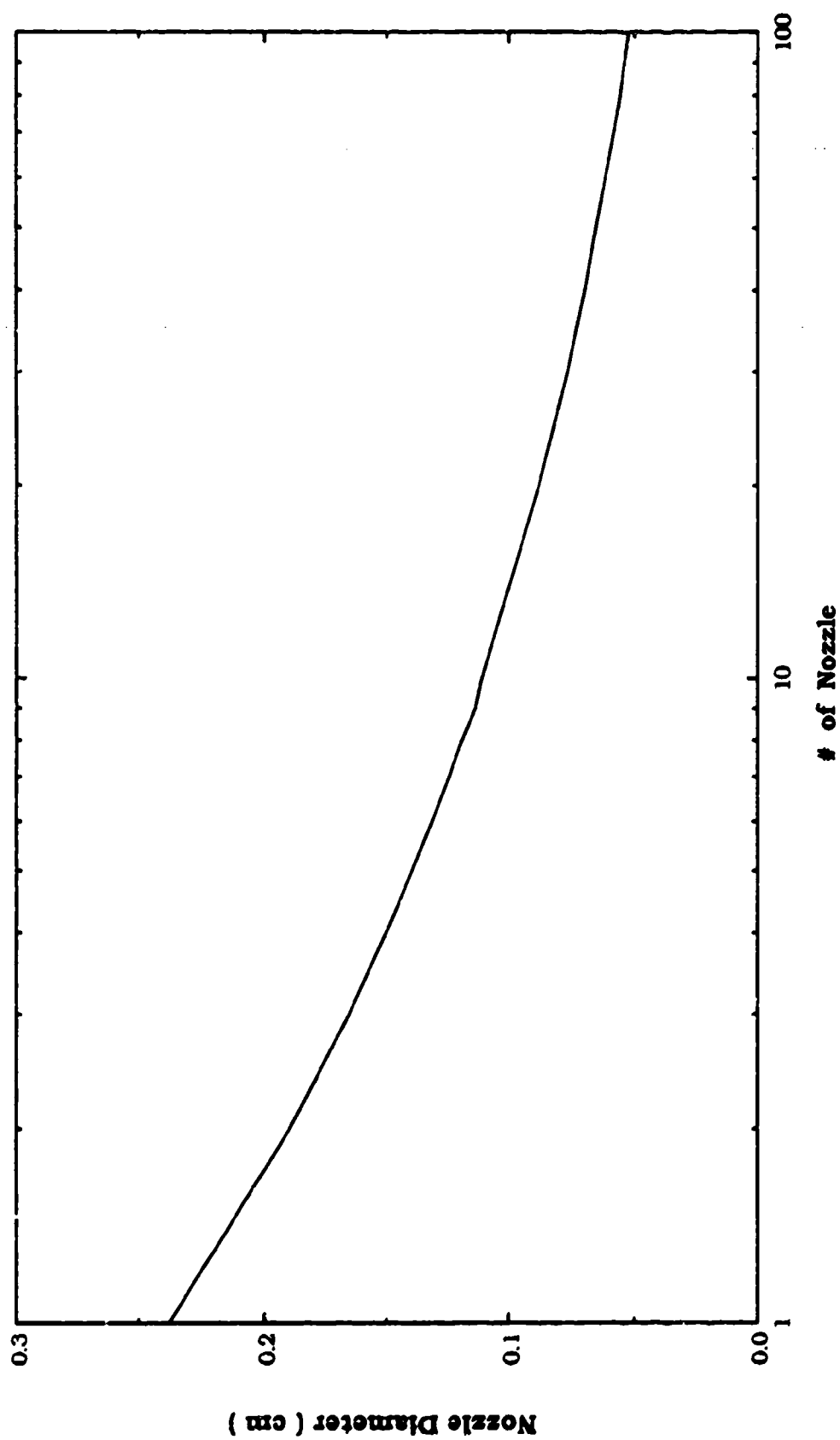
Mult : Nozzle Virtual Impactor Concentrator (  $Q = 10 \text{ lpm}$  )



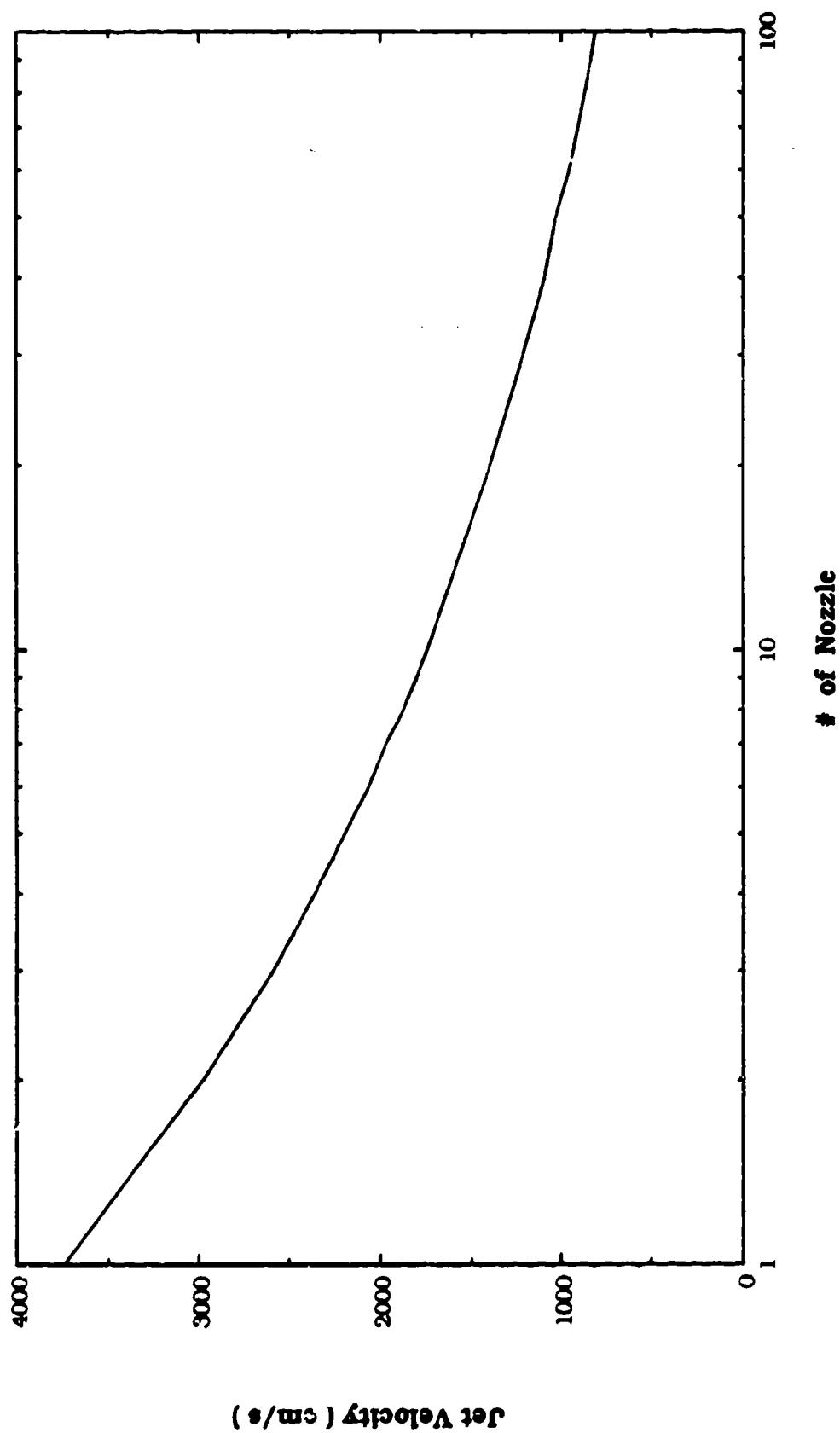
# Multiple Nozzle Virtual Impactor Concentrator ( $Q = 10 \text{ lpm}$ )



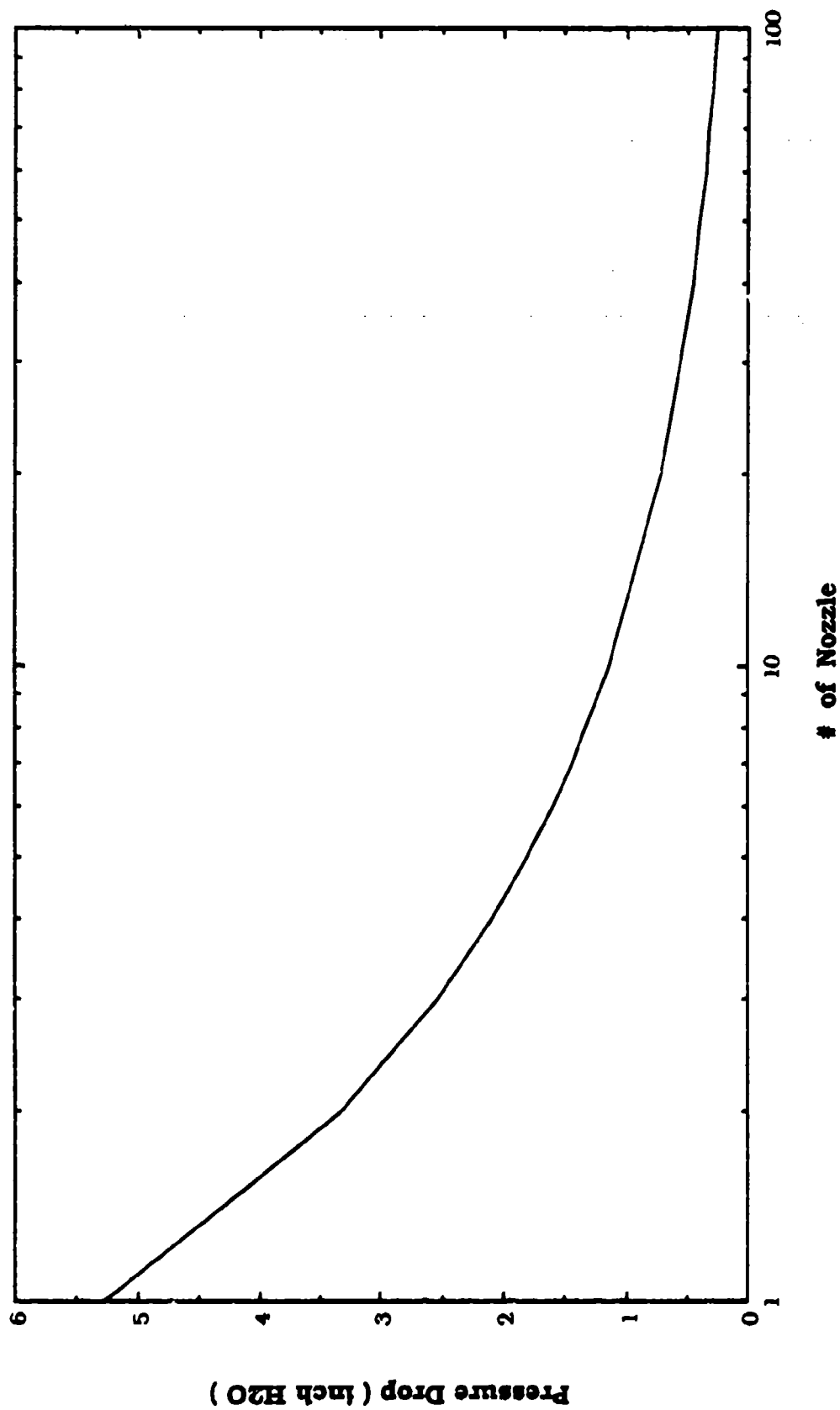
Multiple Nozzle Virtual Impactor Concentrator (  $Q = 10 \text{ lpm}$  )



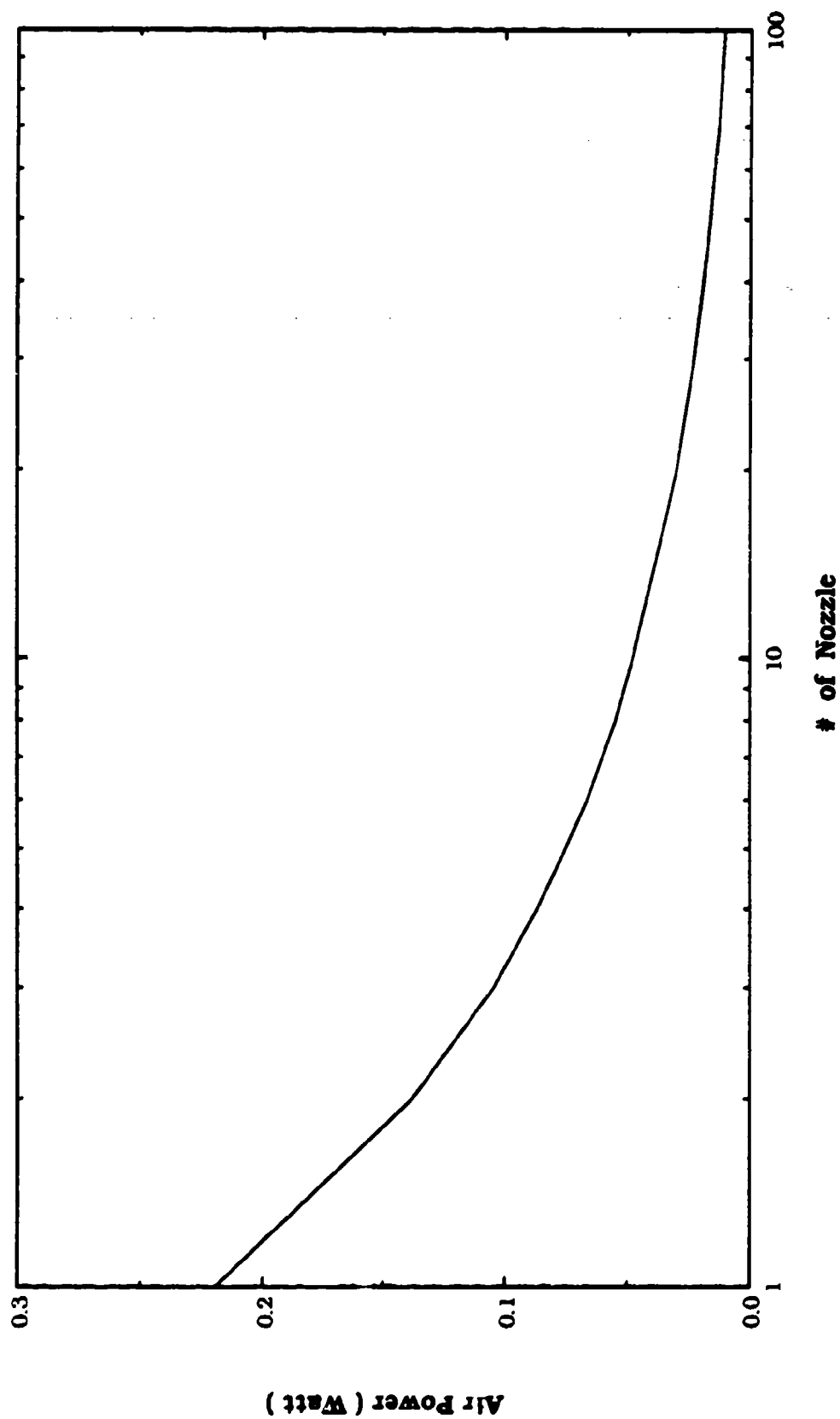
# Multiple Nozzle Virtual Impactor Concentrator (Q= 10 lpm )



Multiple Nozzle Virtual Impactor Concentrator (  $Q = 10 \text{ lpm}$  )

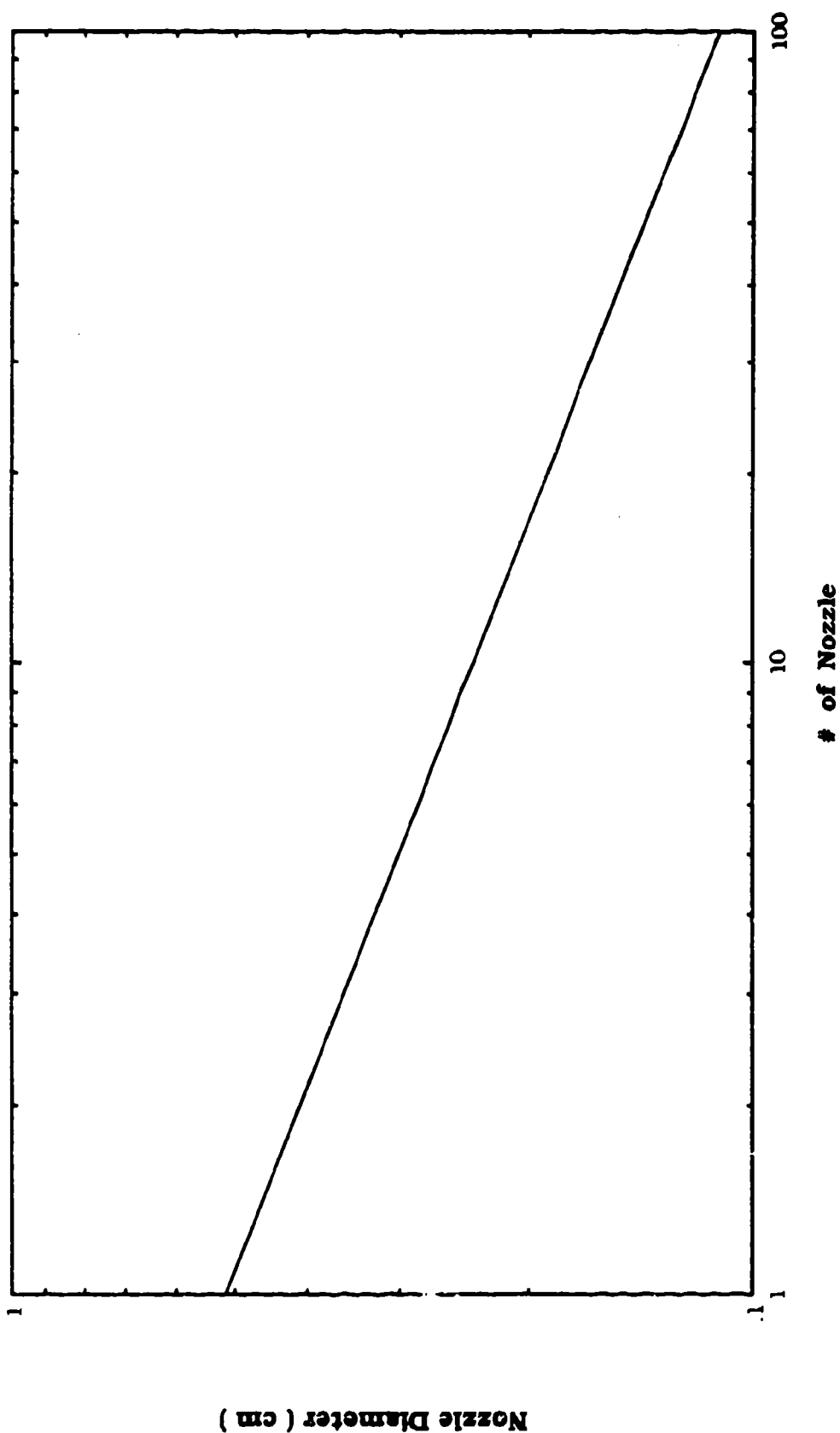


# Multiple Nozzle Virtual Impactor Concentrator ( Q= 10 lpm )

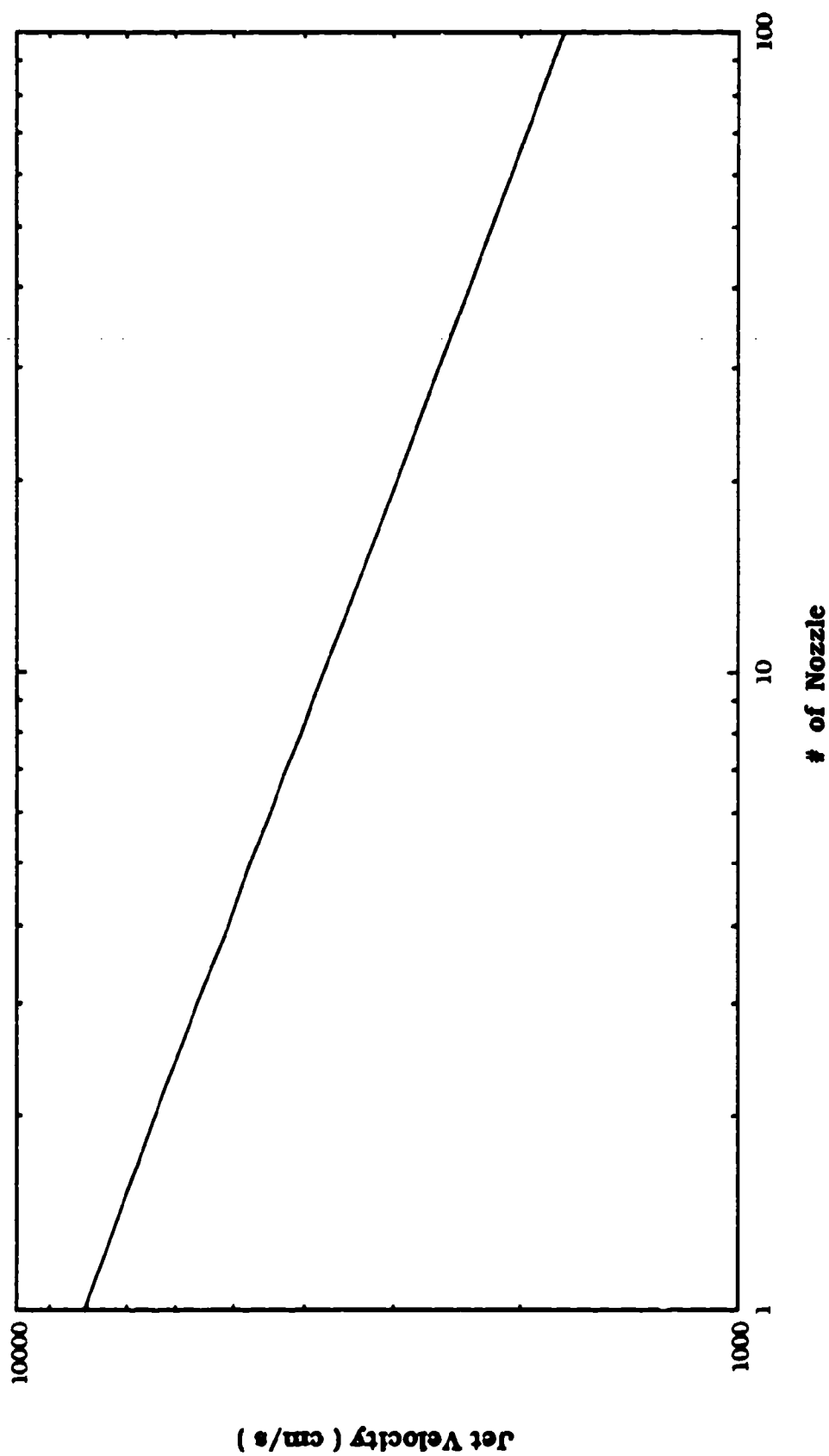




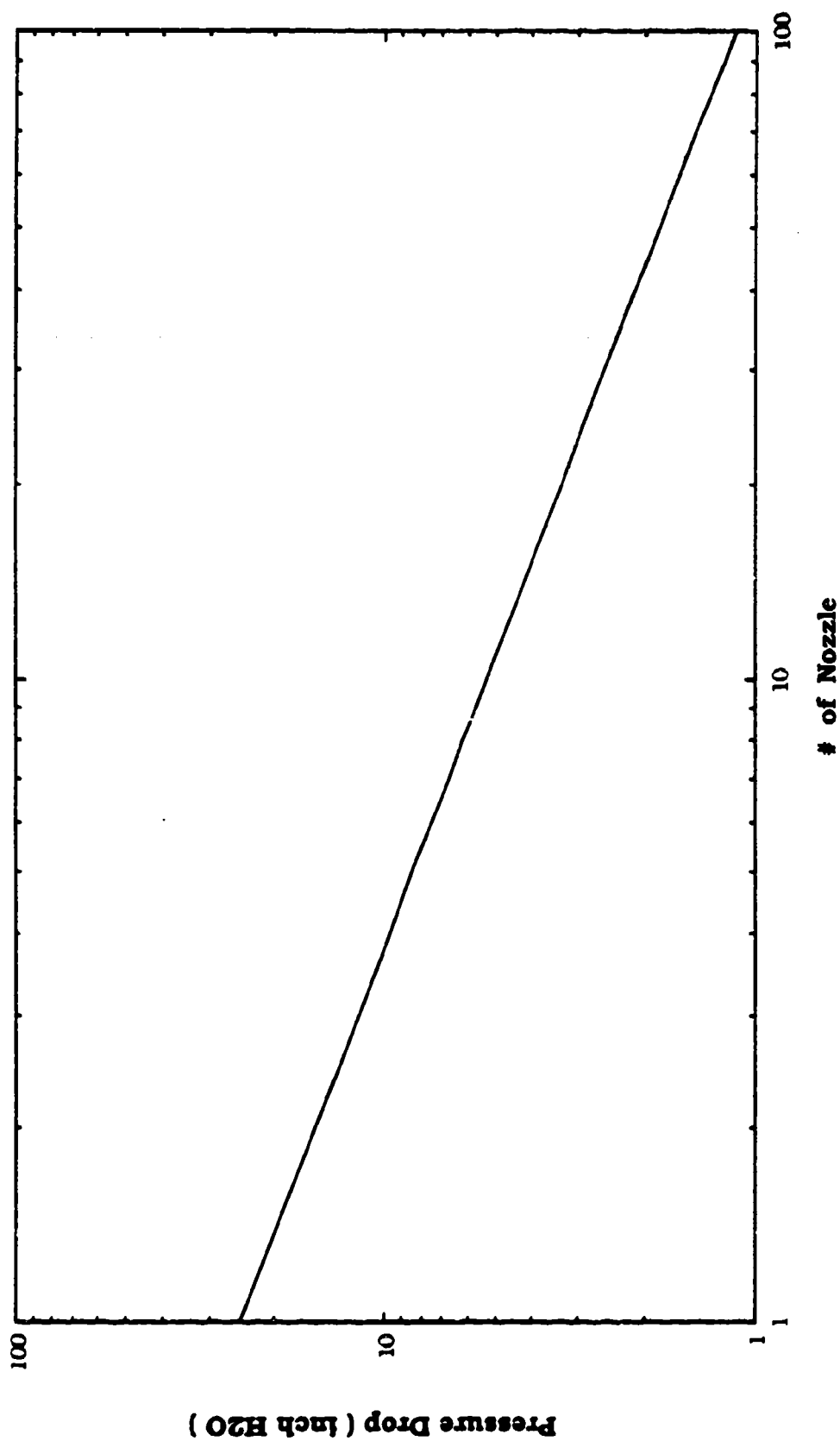
# Multiple Nozzle Virtual Impactor Concentrator ( $Q=100$ lpm )



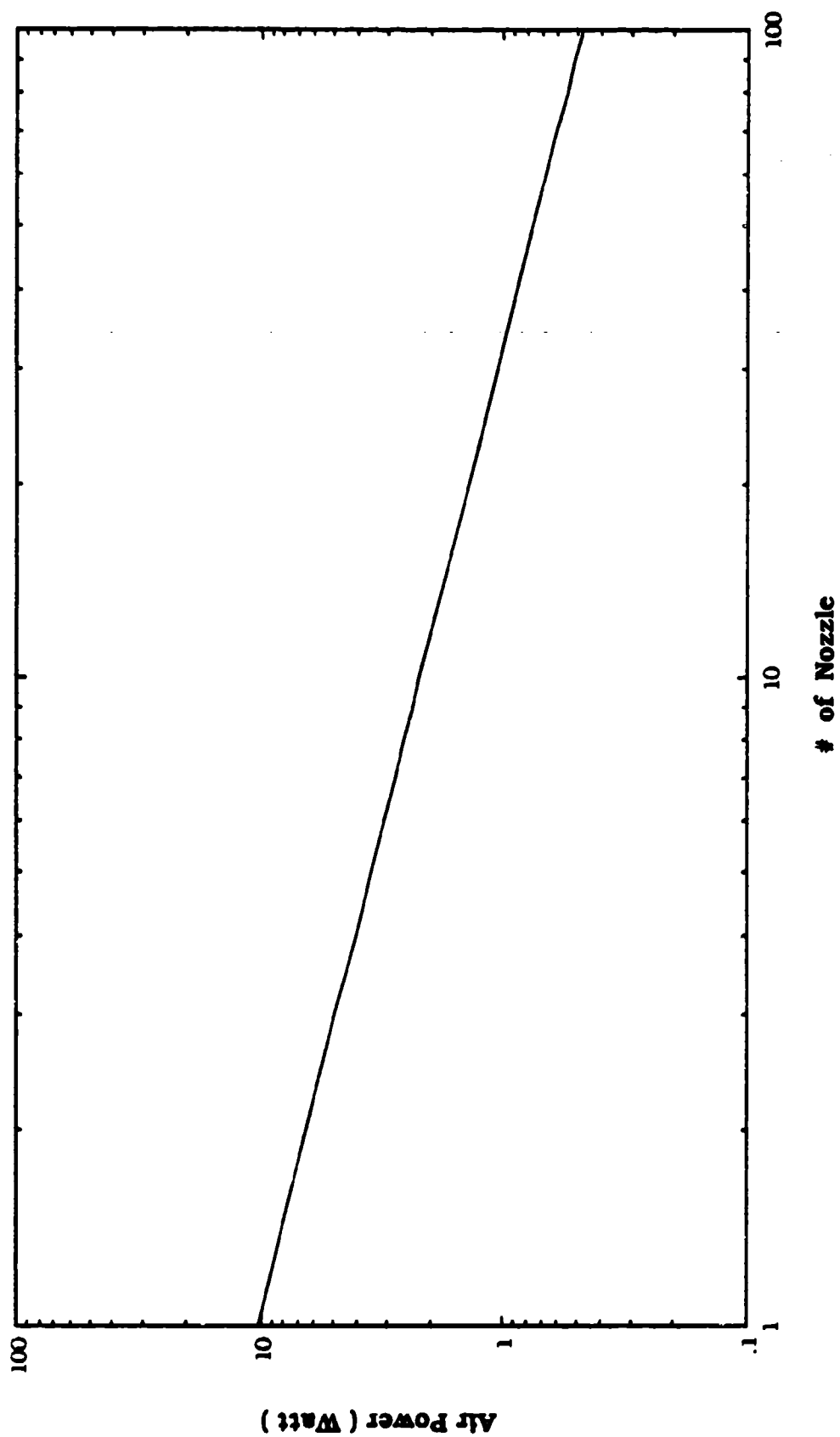
# Multiple Nozzle Virtual Impactor Concentrator ( $Q = 100 \text{ lpm}$ )



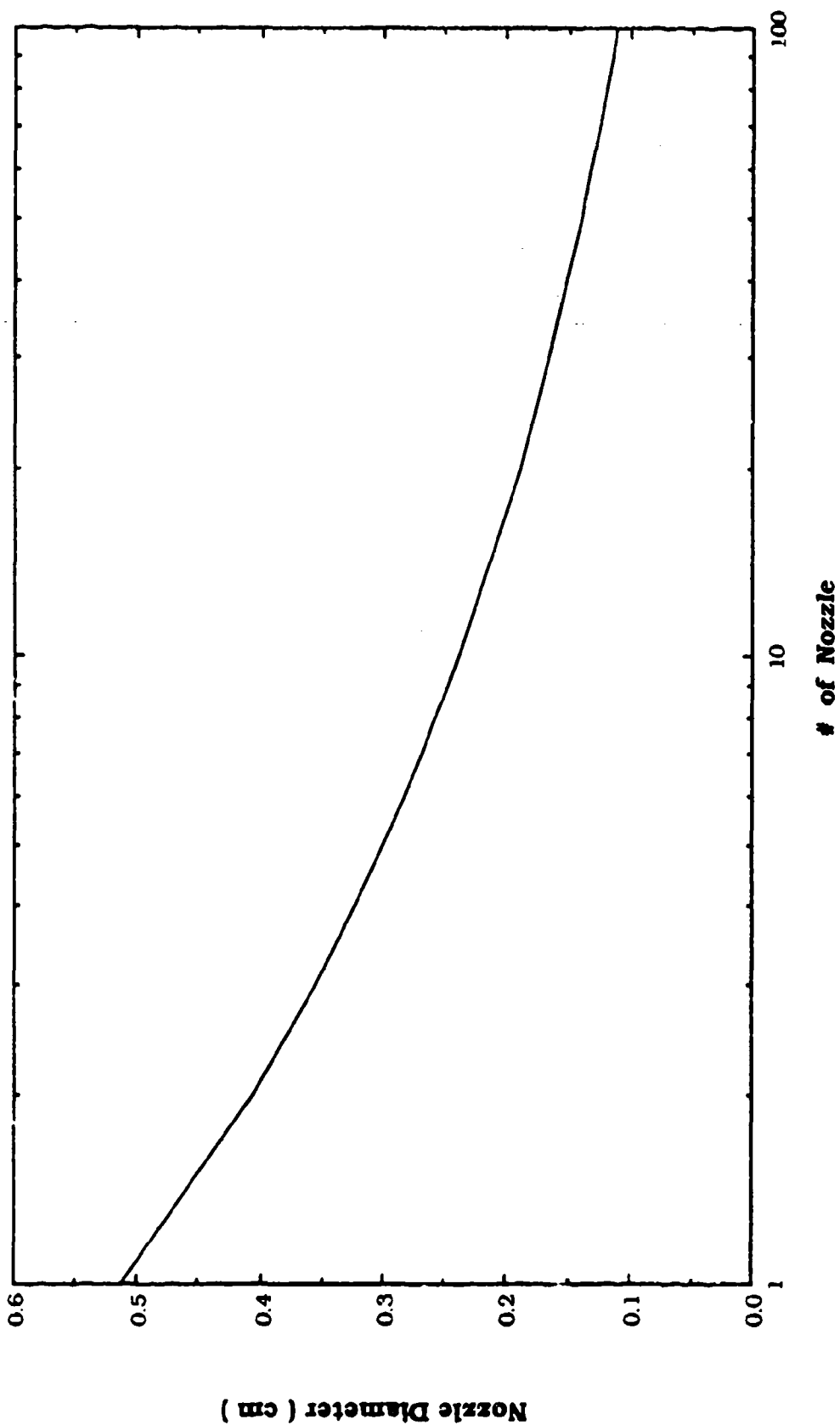
# Multiple Nozzle Virtual Impactor Concentrator ( Q= 100 lpm )



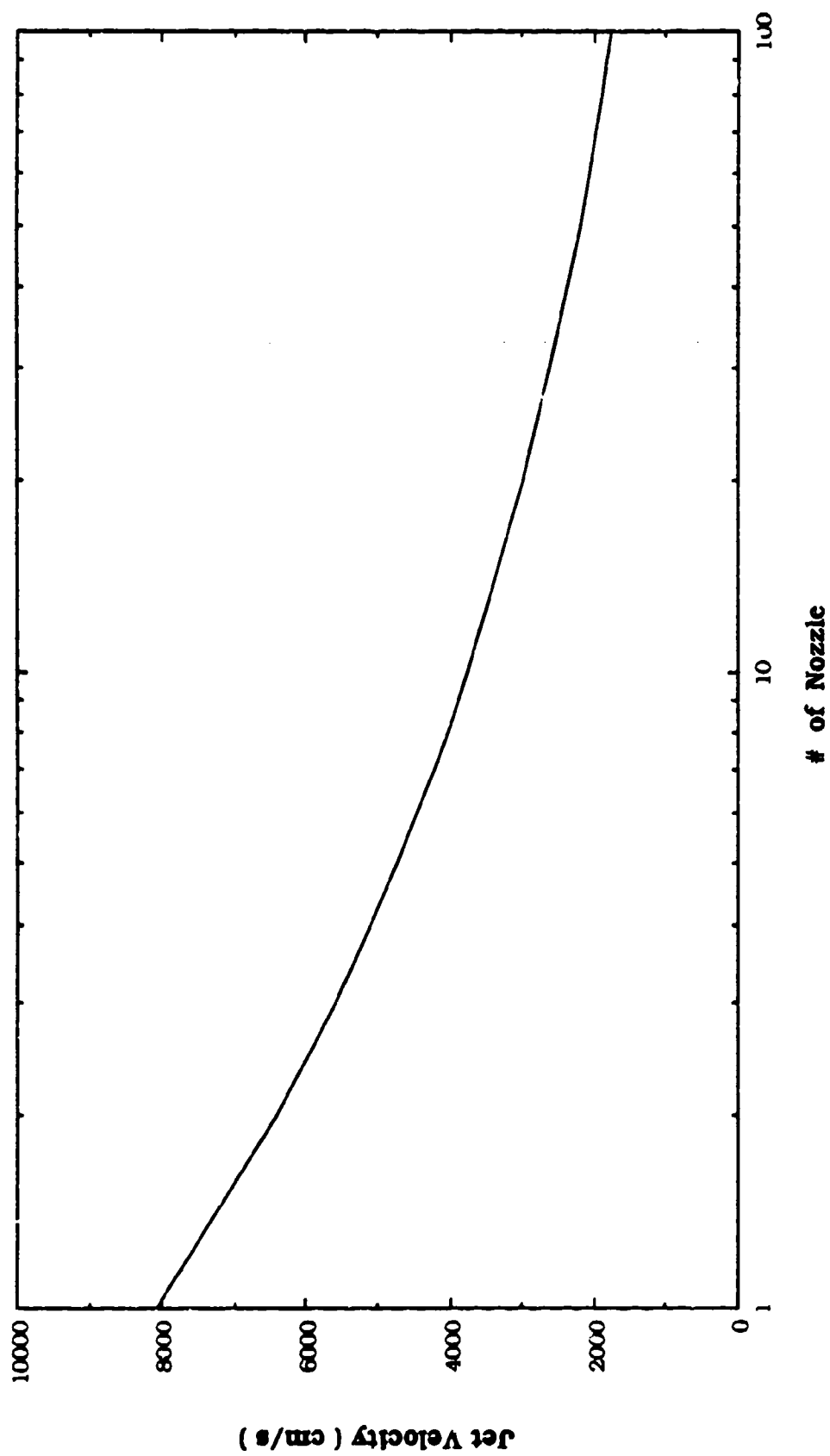
# Multiple Nozzle Virtual Impactor Concentrator ( $Q = 100 \text{ lpm}$ )



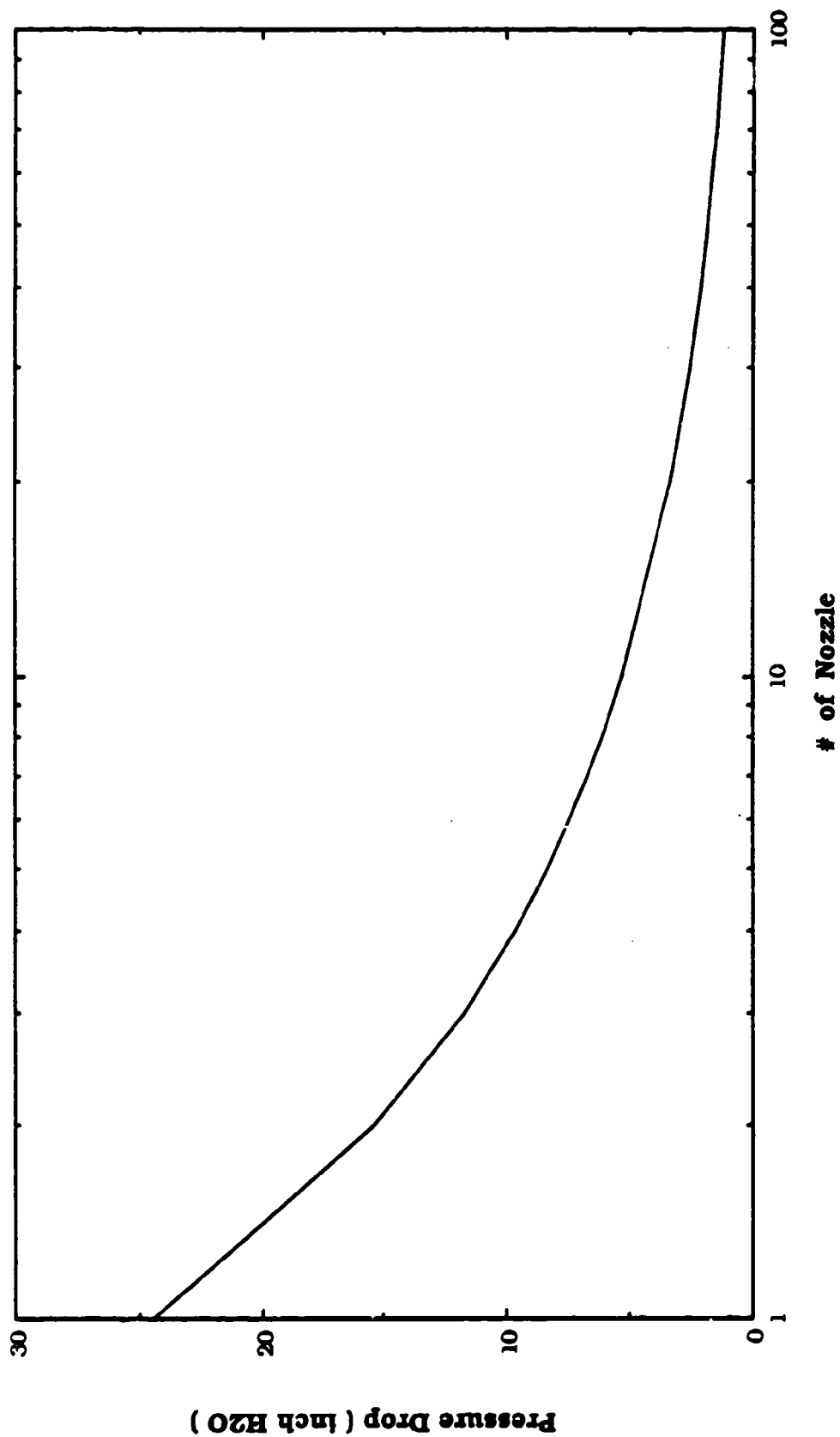
**Multiple Nozzle Virtual Impactor Concentrator (  $Q = 100 \text{ lpm}$  )**



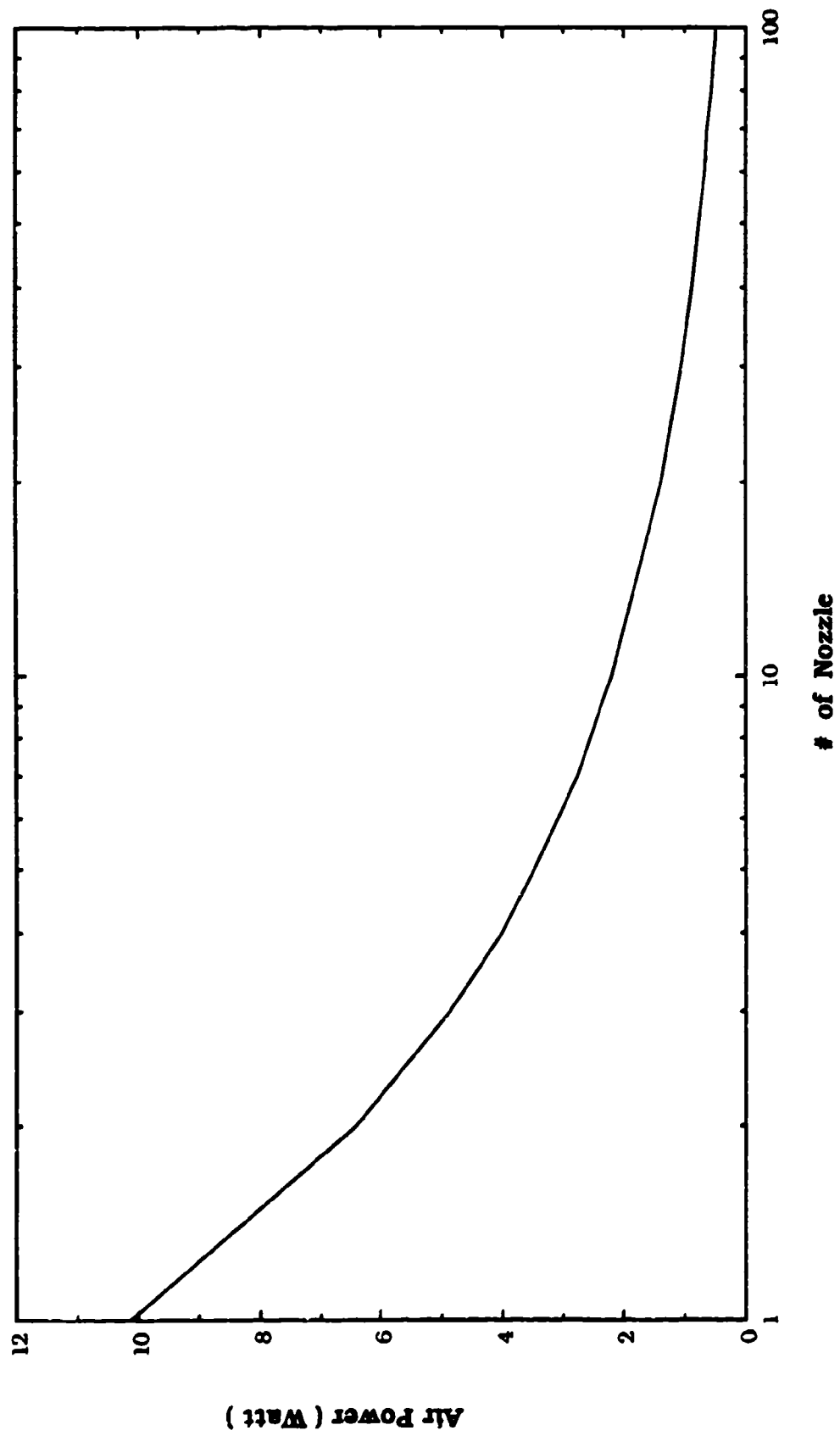
Multiple Nozzle Virtual Impactor Concentrator (  $Q = 100 \text{ lpm}$  )



**Multiple Nozzle Virtual Impactor Concentrator (  $Q = 100 \text{ lpm}$  )**

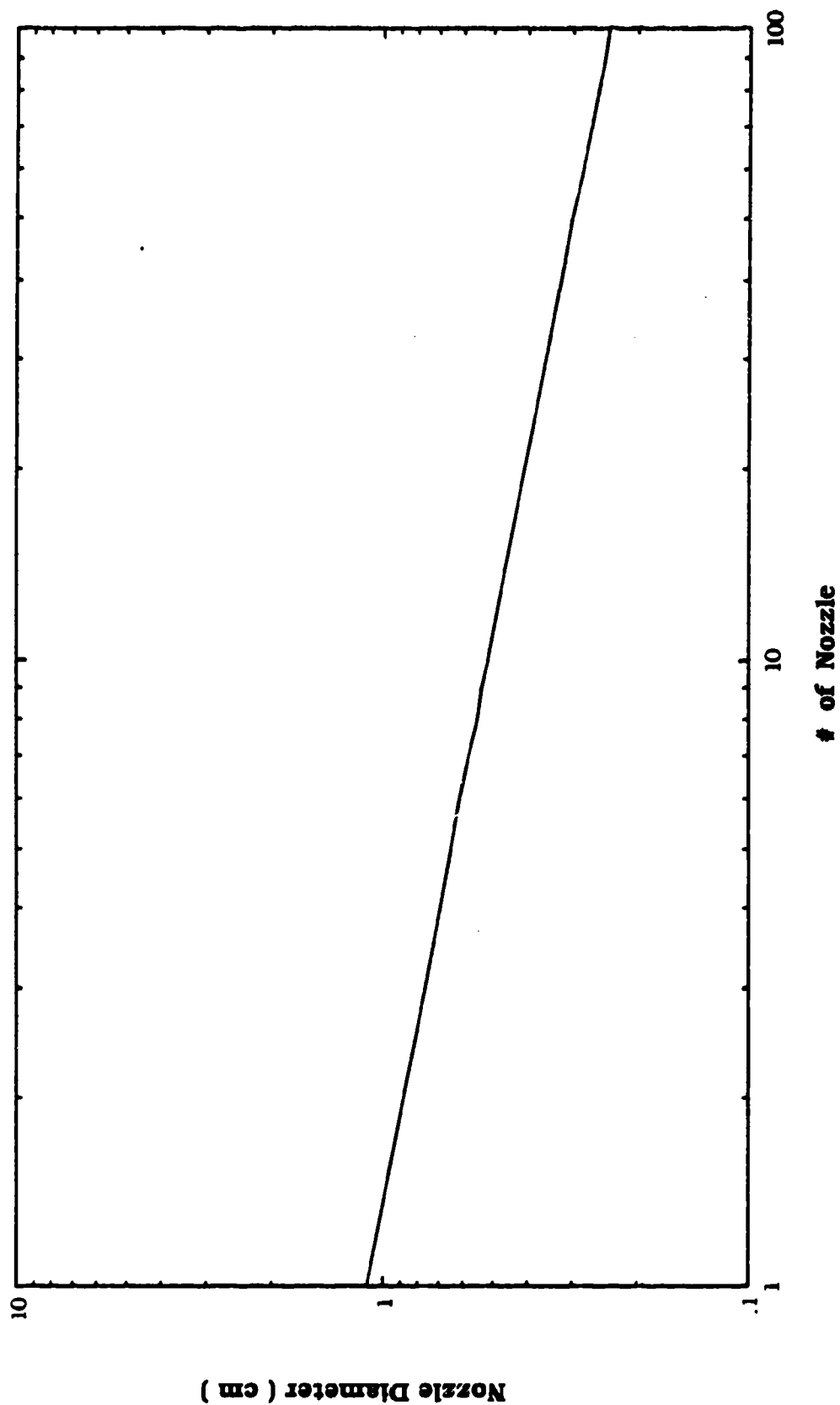


Multiple Nozzle Virtual Impactor Concentrator (  $Q = 100$  lpm )

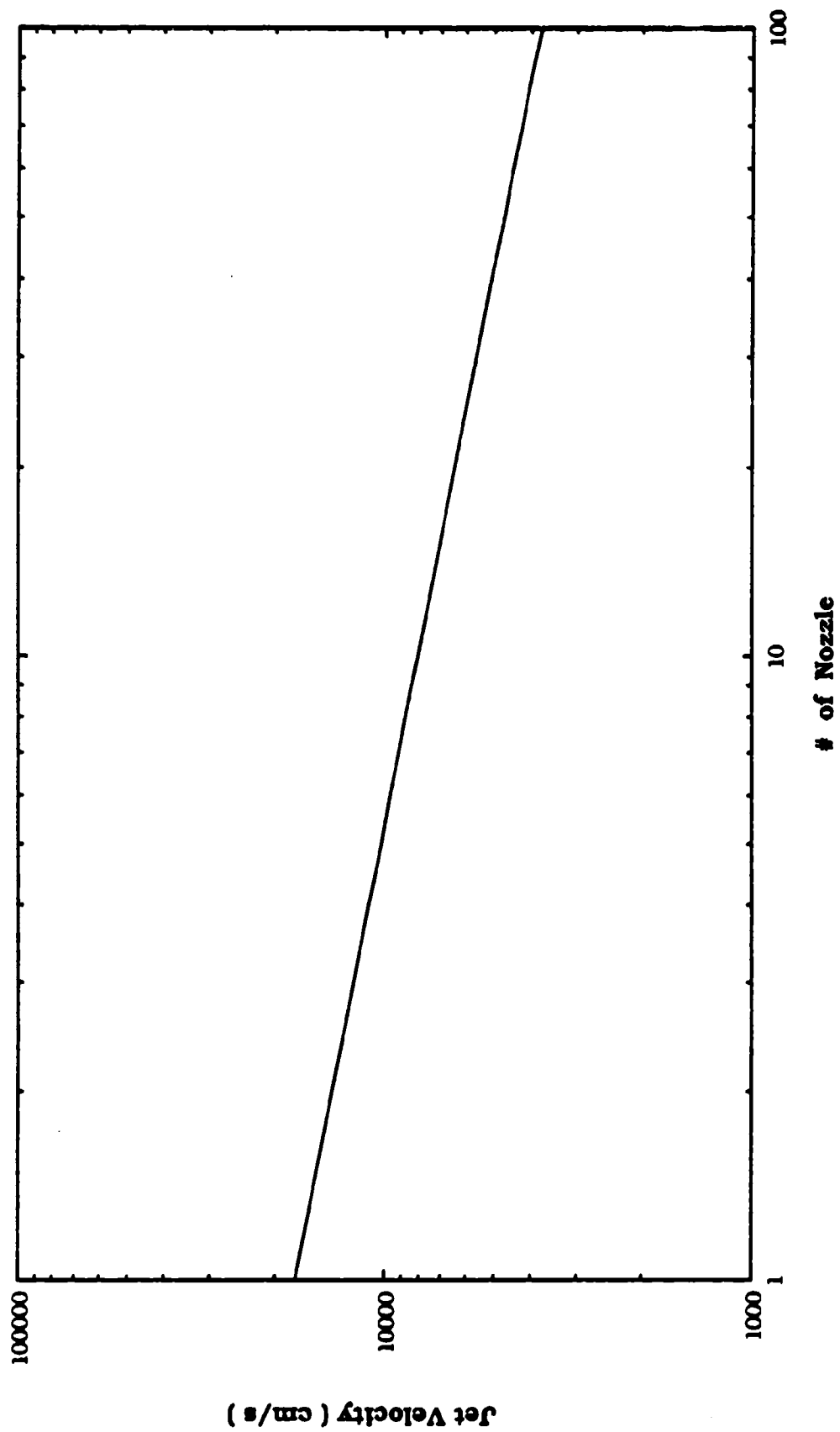




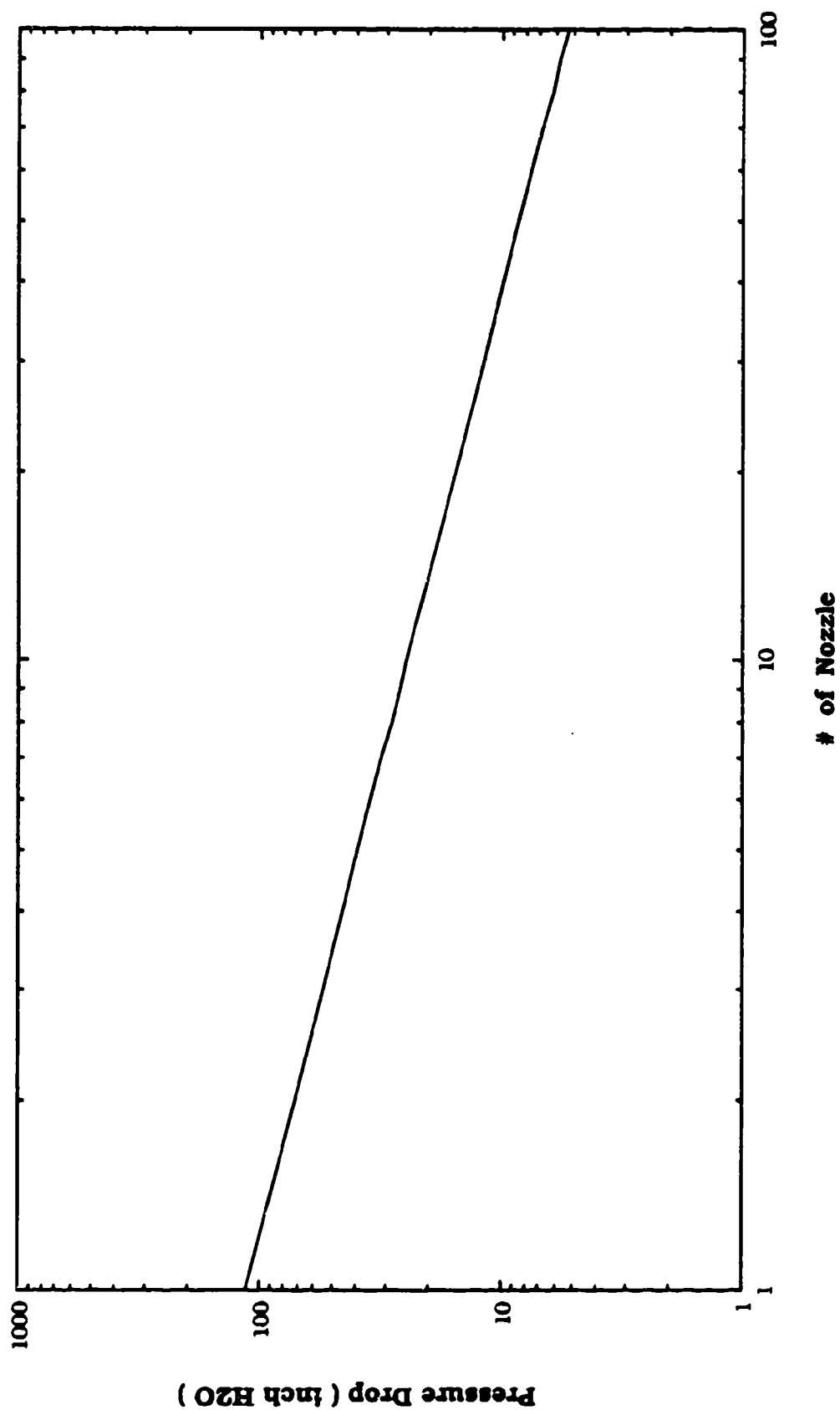
# Multiple Nozzle Virtual Impactor Concentrator ( $Q = 1000 \text{ lpm}$ )



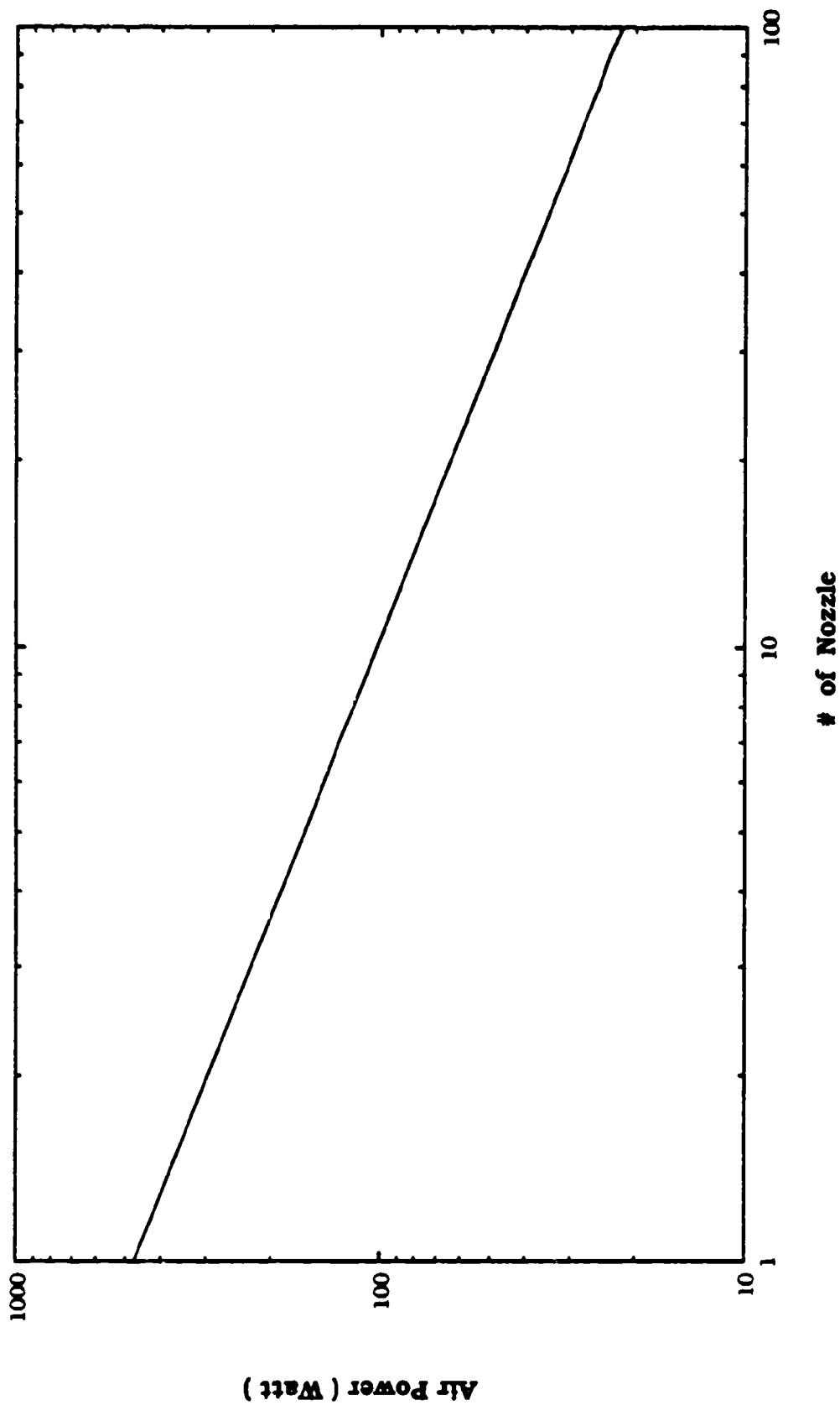
# Multiple Nozzle Virtual Impactor Concentrator ( Q= 1000 lpm )



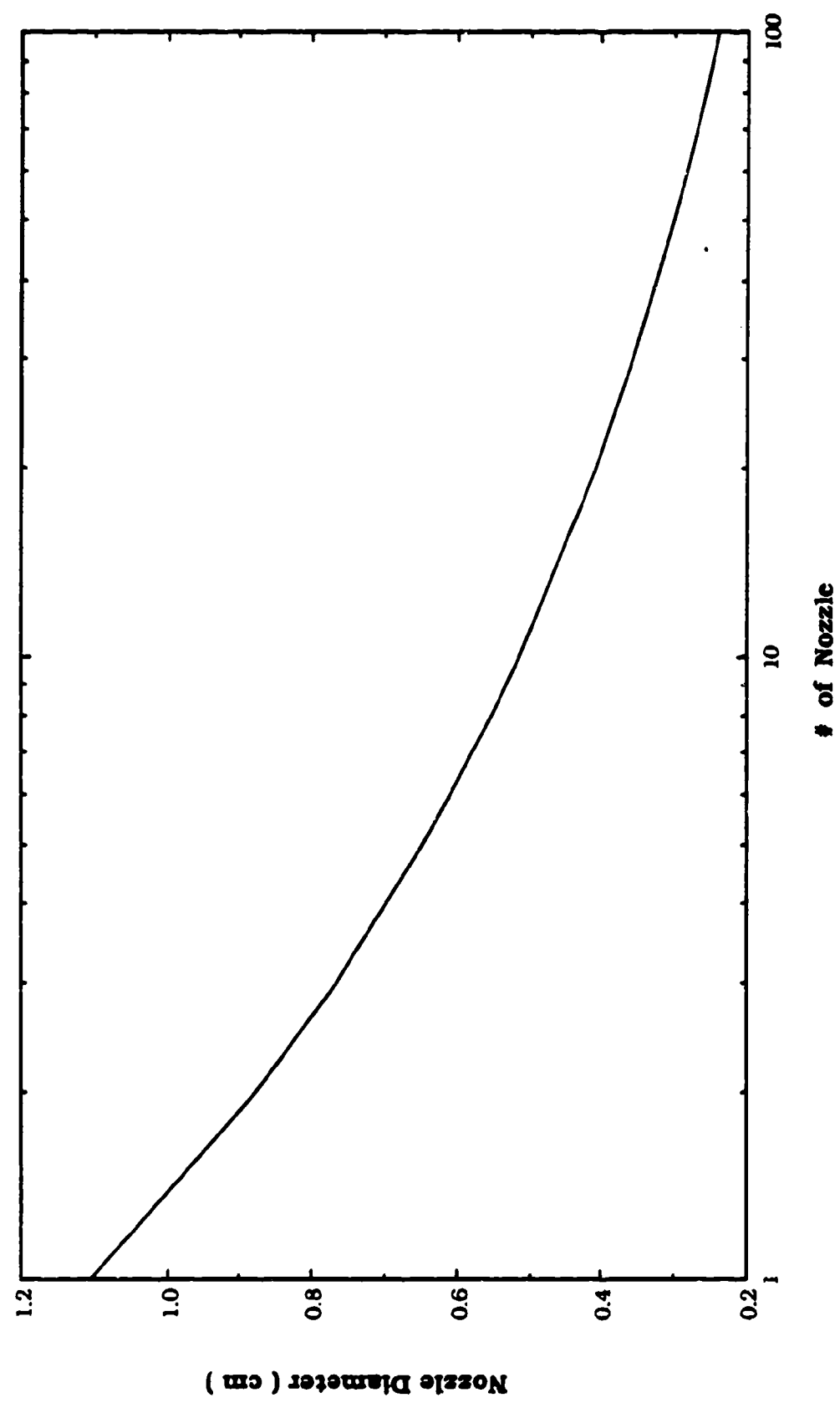
# Multiple Nozzle Virtual Impactor Concentrator ( Q= 1000 lpm )



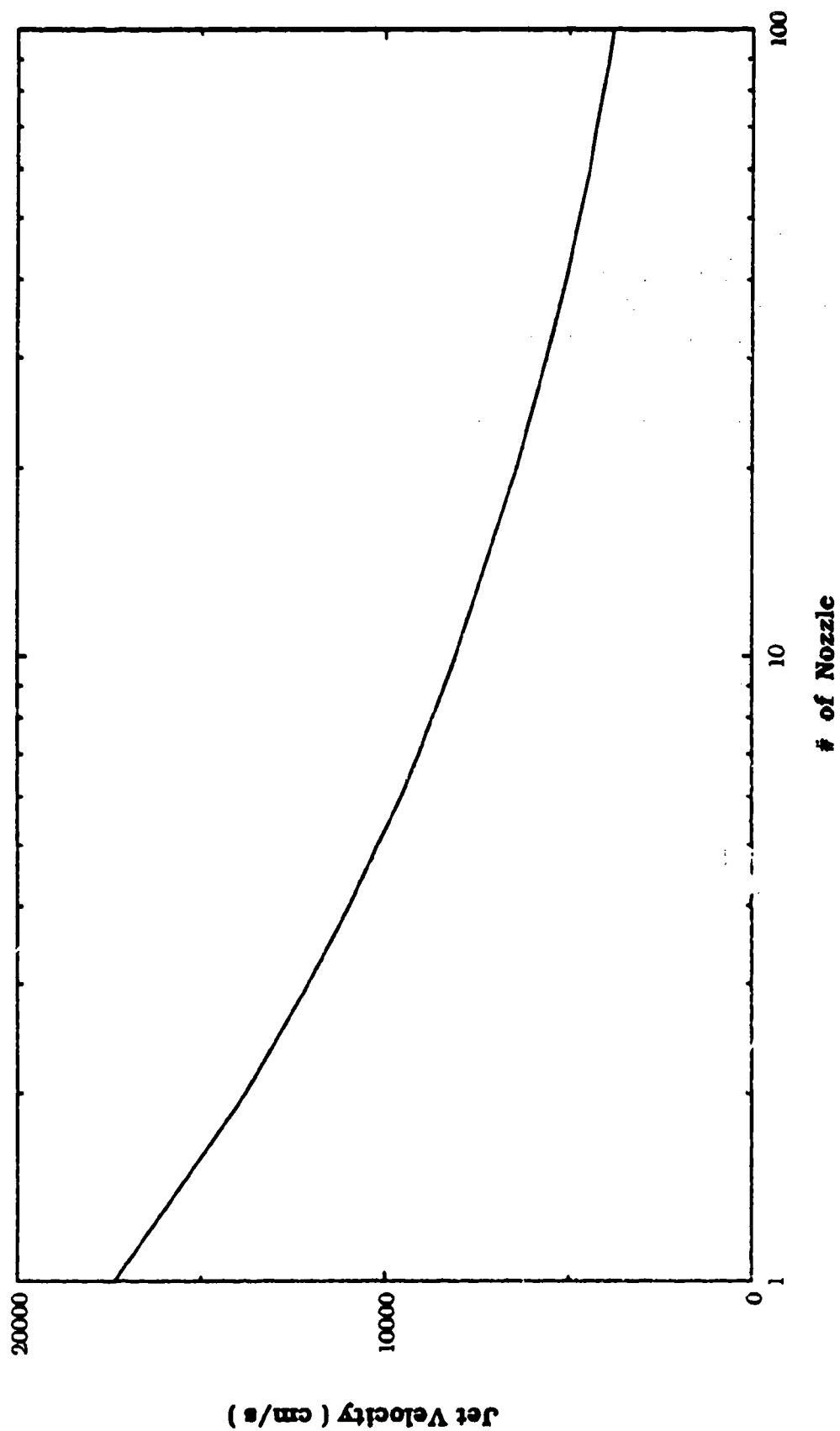
**Multiple Nozzle Virtual Impactor Concentrator ( Q= 1000 lpm )**



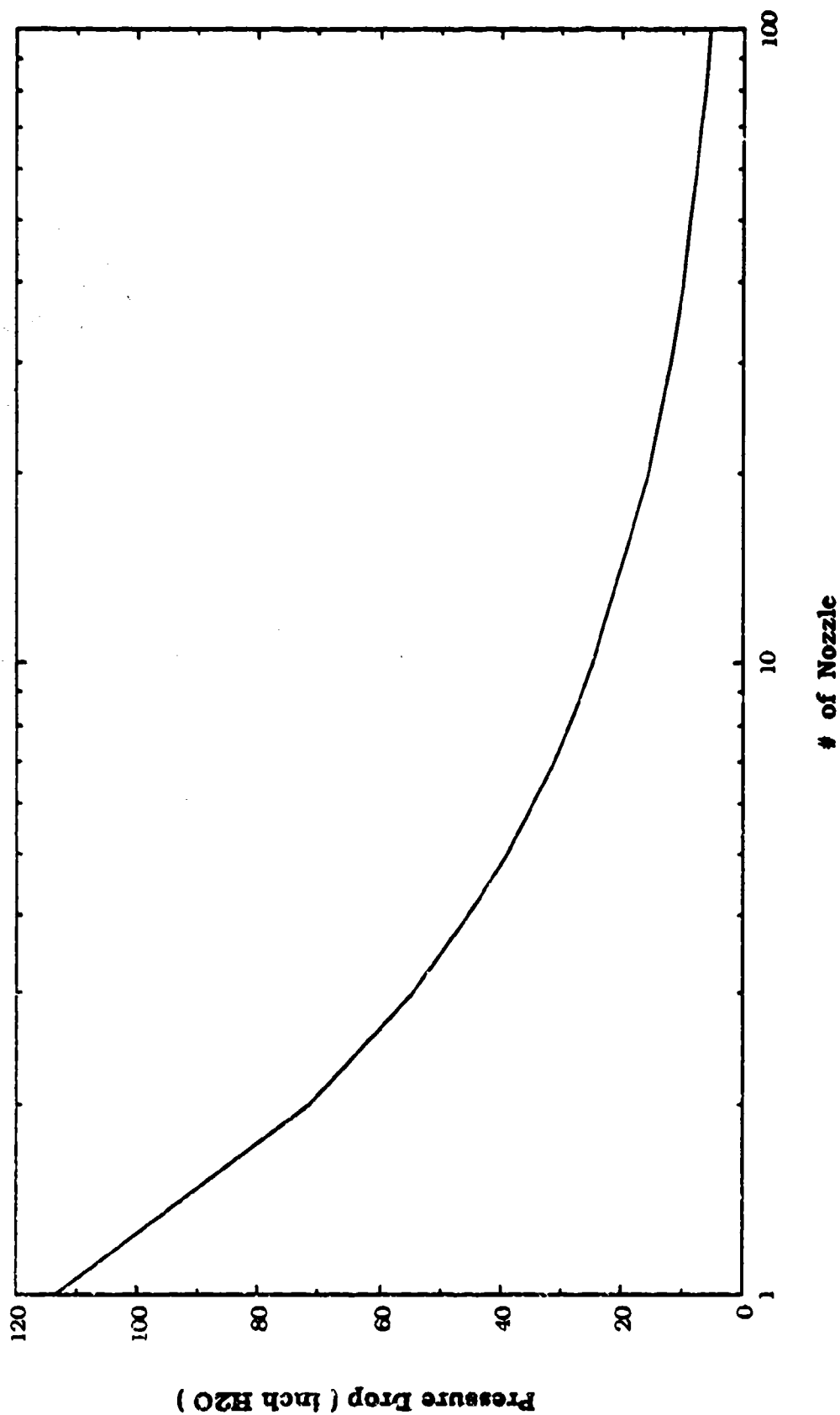
Multiple Nozzle Virtual Impactor Concentrator (  $Q = 1000$  lpm )



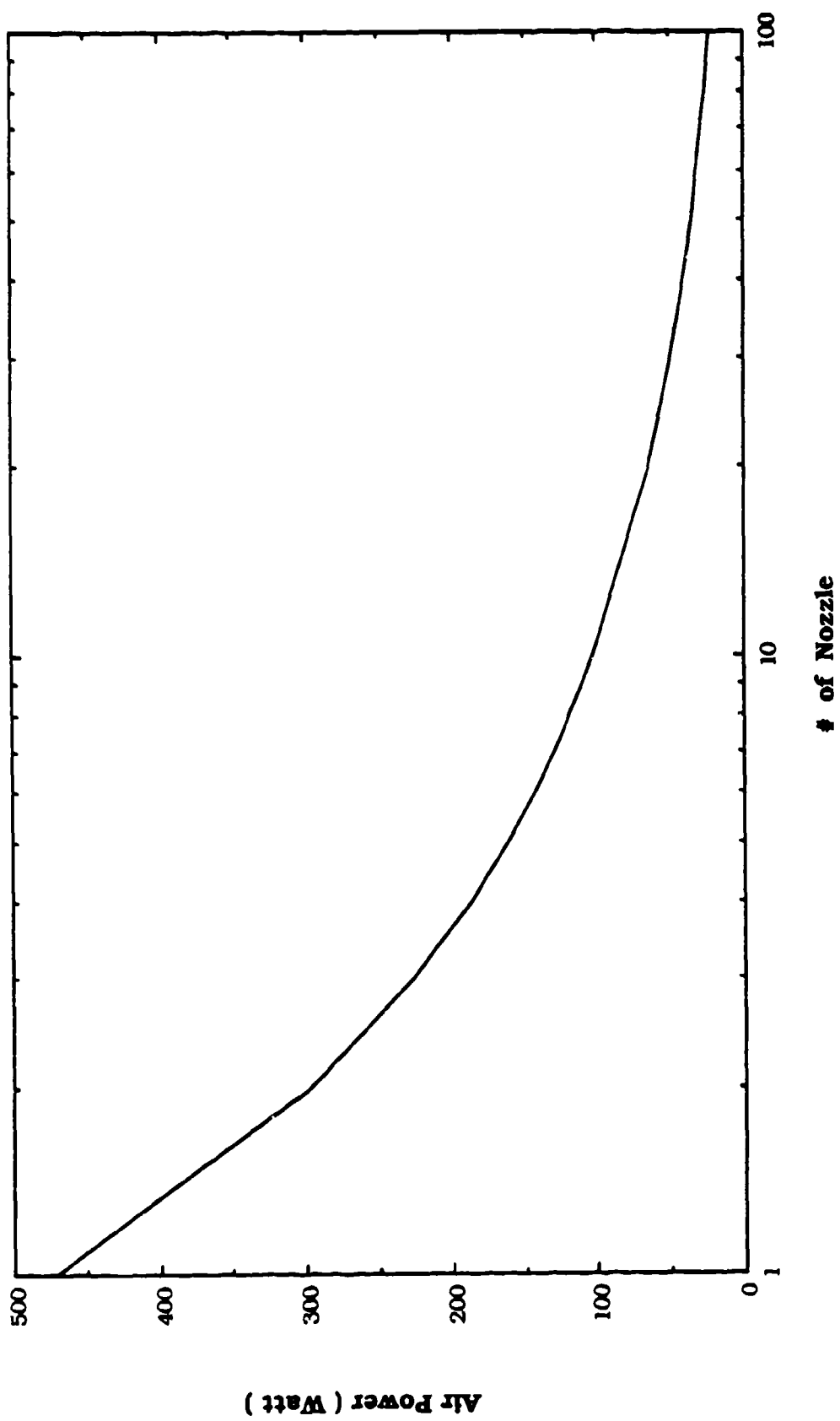
**Multiple Nozzle Virtual Impactor Concentrator (  $Q = 1000$  lpm )**



Multiple Nozzle Virtual Impactor Concentrator (  $Q = 1000$  lpm )

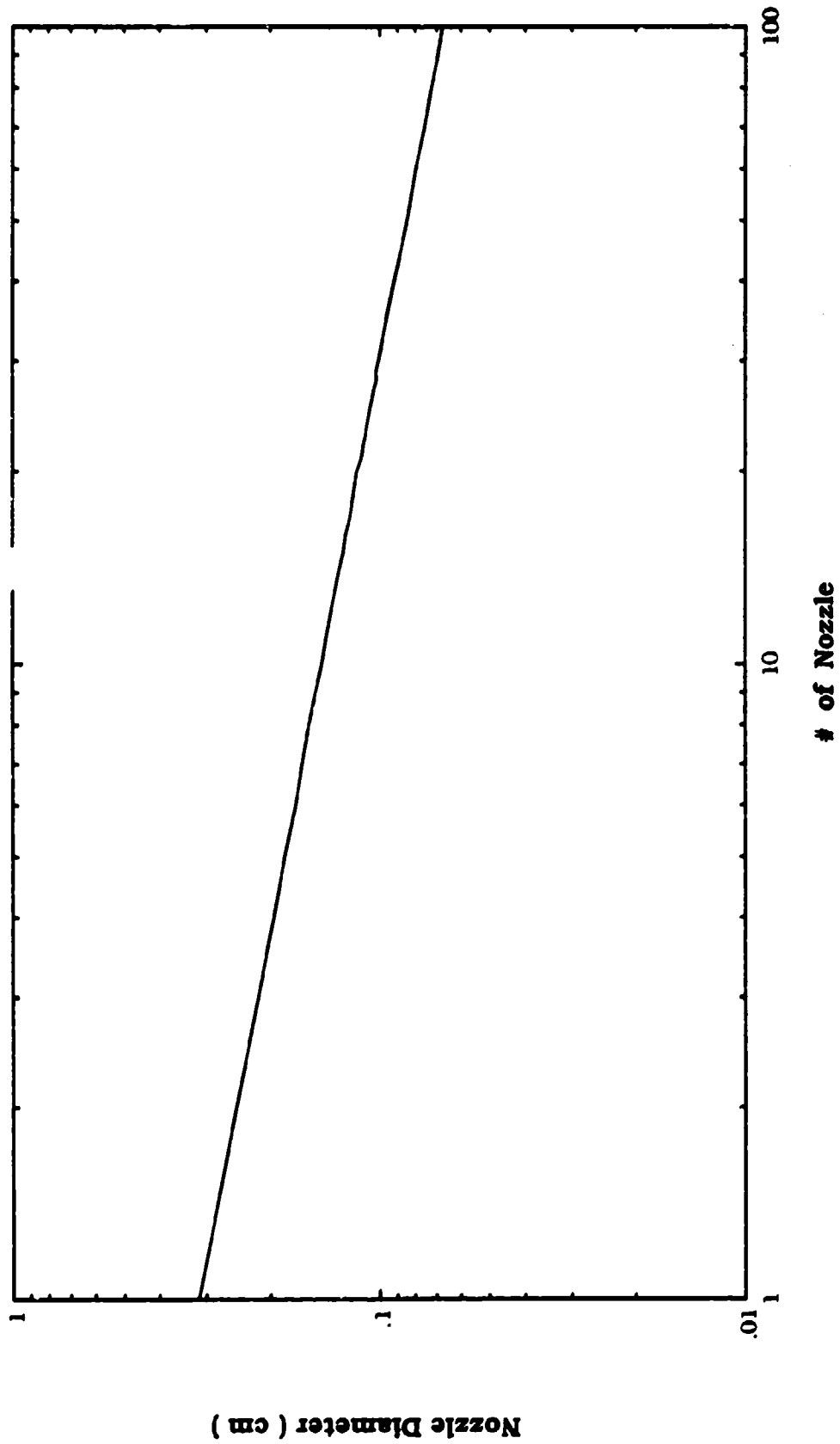


Multiple Nozzle Virtual Impactor Concentrator (  $Q = 1000$  lpm )

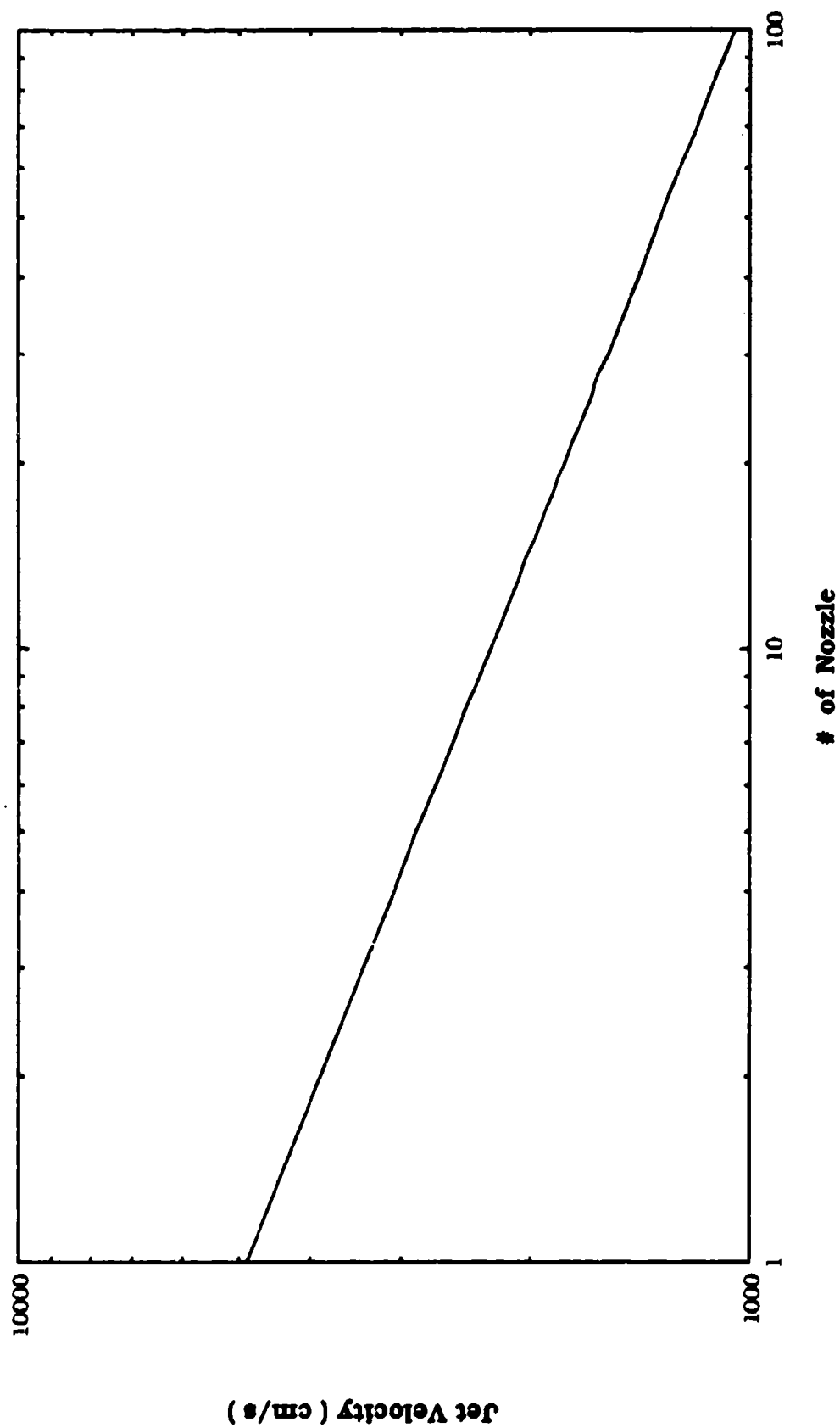


DP, um	2				
Slip Correction	1.11E+00				
Relaxation Time	1.34E-05				
$St^{0.5}$	6.50E-01				
Stokes Number	4.23E-01				
Nozzle Coefficient	8.00E-01				
Q, lpm	22				
Nozzle #	Flow Rate/ nozzle, lpm	Nozzle Dia. D, cm	Jet Velocity U, cm/s	Press. Drop Inch H2O	Air Power Watt
1	2.20E+01	3.10E-01	4.87E+03	8.92E+00	8.14E-01
2	1.10E+01	2.46E-01	3.86E+03	5.62E+00	5.13E-01
3	7.33E+00	2.15E-01	3.37E+03	4.29E+00	3.91E-01
4	5.50E+00	1.95E-01	3.07E+03	3.54E+00	3.23E-01
5	4.40E+00	1.81E-01	2.85E+03	3.05E+00	2.78E-01
6	3.67E+00	1.70E-01	2.68E+03	2.70E+00	2.47E-01
7	3.14E+00	1.62E-01	2.54E+03	2.44E+00	2.22E-01
8	2.75E+00	1.55E-01	2.43E+03	2.23E+00	2.04E-01
9	2.44E+00	1.49E-01	2.34E+03	2.06E+00	1.88E-01
10	2.20E+00	1.44E-01	2.26E+03	1.92E+00	1.75E-01
11	2.00E+00	1.39E-01	2.19E+03	1.80E+00	1.65E-01
12	1.83E+00	1.35E-01	2.13E+03	1.70E+00	1.55E-01
13	1.69E+00	1.32E-01	2.07E+03	1.61E+00	1.47E-01
14	1.57E+00	1.29E-01	2.02E+03	1.54E+00	1.40E-01
15	1.47E+00	1.26E-01	1.97E+03	1.47E+00	1.34E-01
16	1.38E+00	1.23E-01	1.93E+03	1.40E+00	1.28E-01
17	1.29E+00	1.20E-01	1.89E+03	1.35E+00	1.23E-01
18	1.22E+00	1.18E-01	1.86E+03	1.30E+00	1.19E-01
19	1.16E+00	1.16E-01	1.82E+03	1.25E+00	1.14E-01
20	1.10E+00	1.14E-01	1.79E+03	1.21E+00	1.10E-01
21	1.05E+00	1.12E-01	1.76E+03	1.17E+00	1.07E-01
22	1.00E+00	1.11E-01	1.74E+03	1.14E+00	1.04E-01
23	9.57E-01	1.09E-01	1.71E+03	1.10E+00	1.01E-01
24	9.17E-01	1.07E-01	1.69E+03	1.07E+00	9.78E-02
25	8.80E-01	1.06E-01	1.66E+03	1.04E+00	9.52E-02
26	8.46E-01	1.05E-01	1.64E+03	1.02E+00	9.28E-02
27	8.15E-01	1.03E-01	1.62E+03	9.91E-01	9.04E-02
28	7.86E-01	1.02E-01	1.60E+03	9.67E-01	8.83E-02
29	7.59E-01	1.01E-01	1.58E+03	9.45E-01	8.62E-02
30	7.33E-01	9.97E-02	1.57E+03	9.24E-01	8.43E-02
40	5.50E-01	9.06E-02	1.42E+03	7.63E-01	6.96E-02
50	4.40E-01	8.41E-02	1.32E+03	6.57E-01	6.00E-02
60	3.67E-01	7.91E-02	1.24E+03	5.82E-01	5.31E-02
70	3.14E-01	7.52E-02	1.18E+03	5.25E-01	4.79E-02
80	2.75E-01	7.19E-02	1.13E+03	4.80E-01	4.38E-02
90	2.44E-01	6.91E-02	1.09E+03	4.44E-01	4.05E-02
100	2.20E-01	6.67E-02	1.05E+03	4.14E-01	3.78E-02
					End

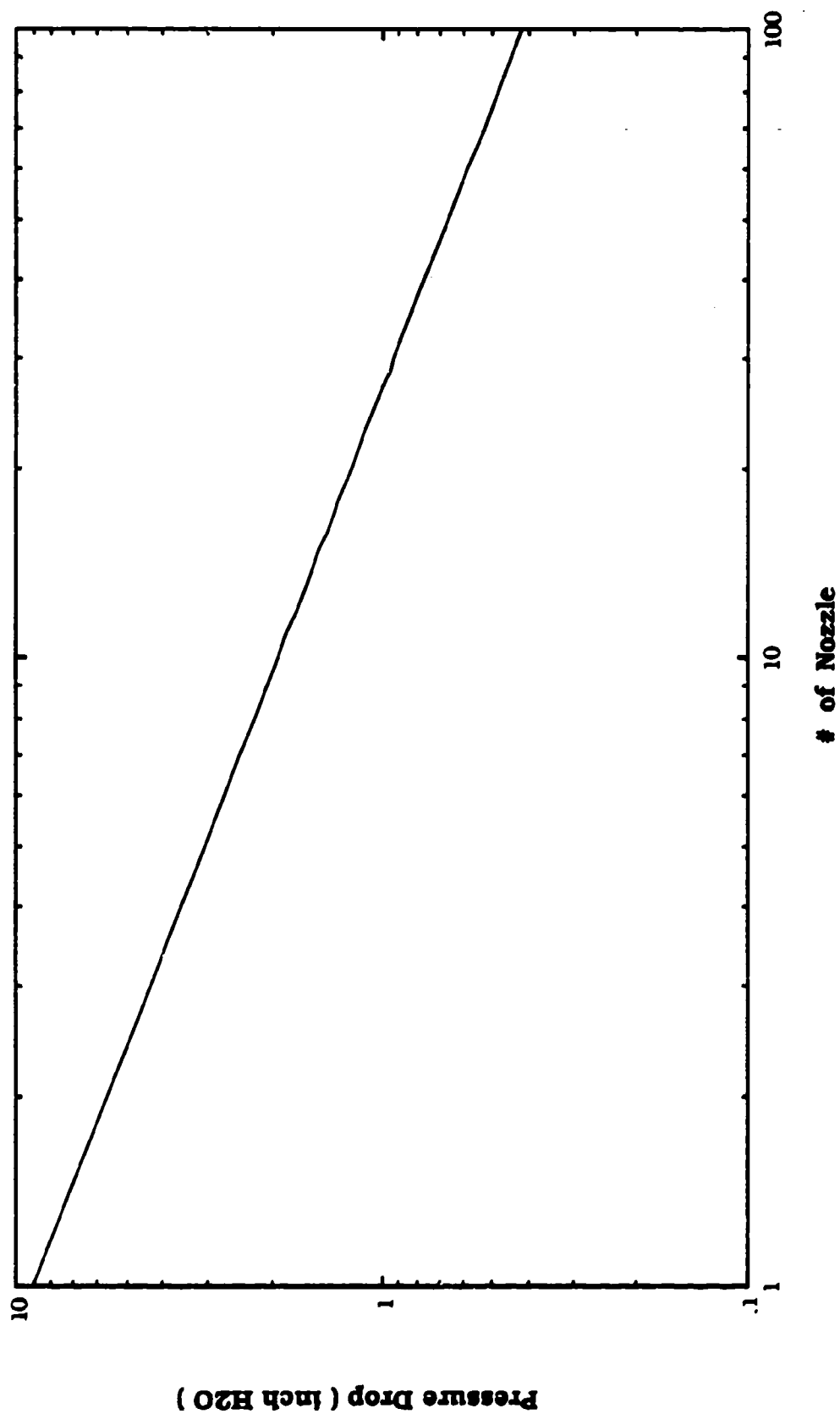
# Multiple Nozzle Virtual Impact Concentrator ( $Q = 22 \text{ lpm}$ )



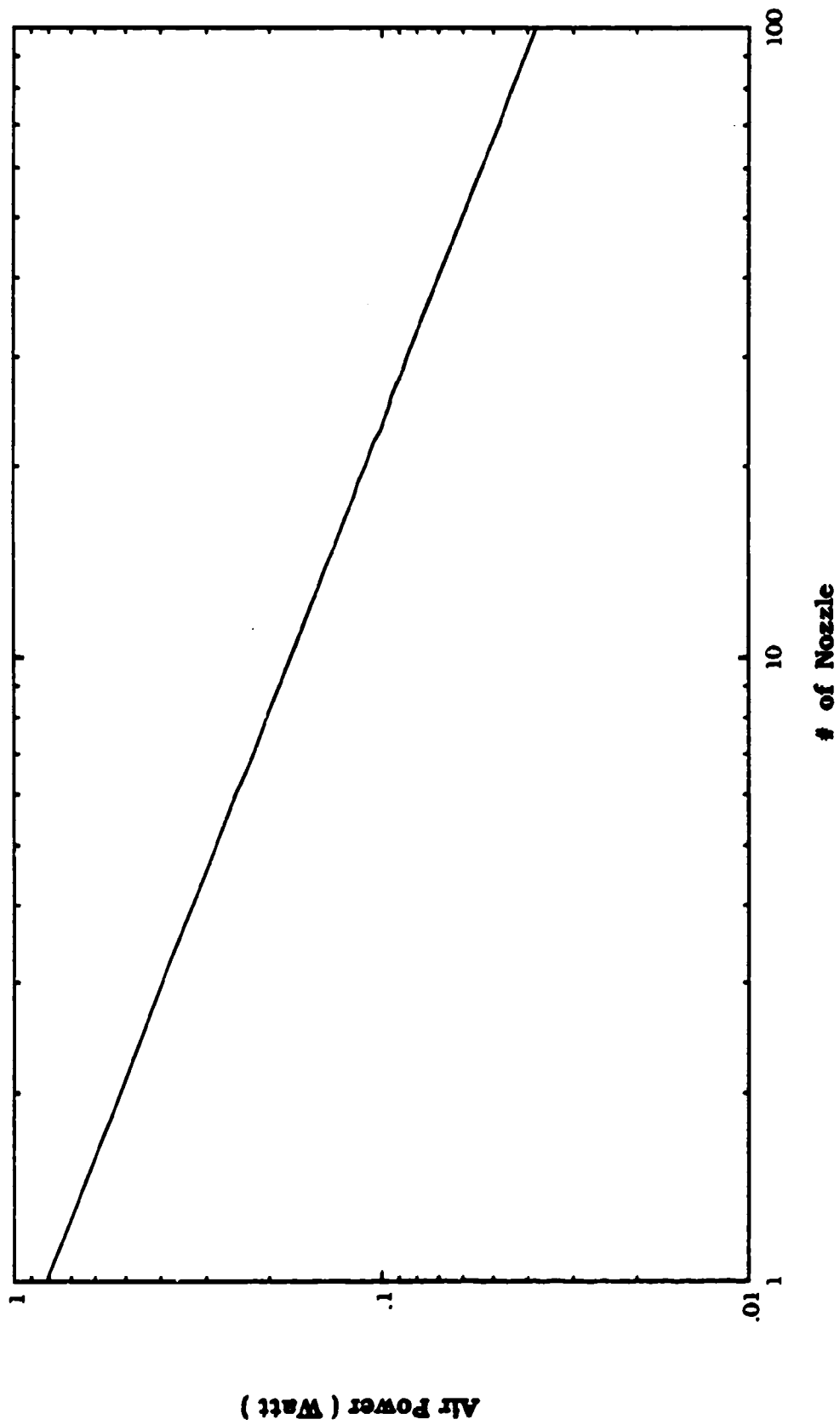
# Multiple Nozzle Virtual Impactor Concentrator ( $Q = 22 \text{ lpm}$ )



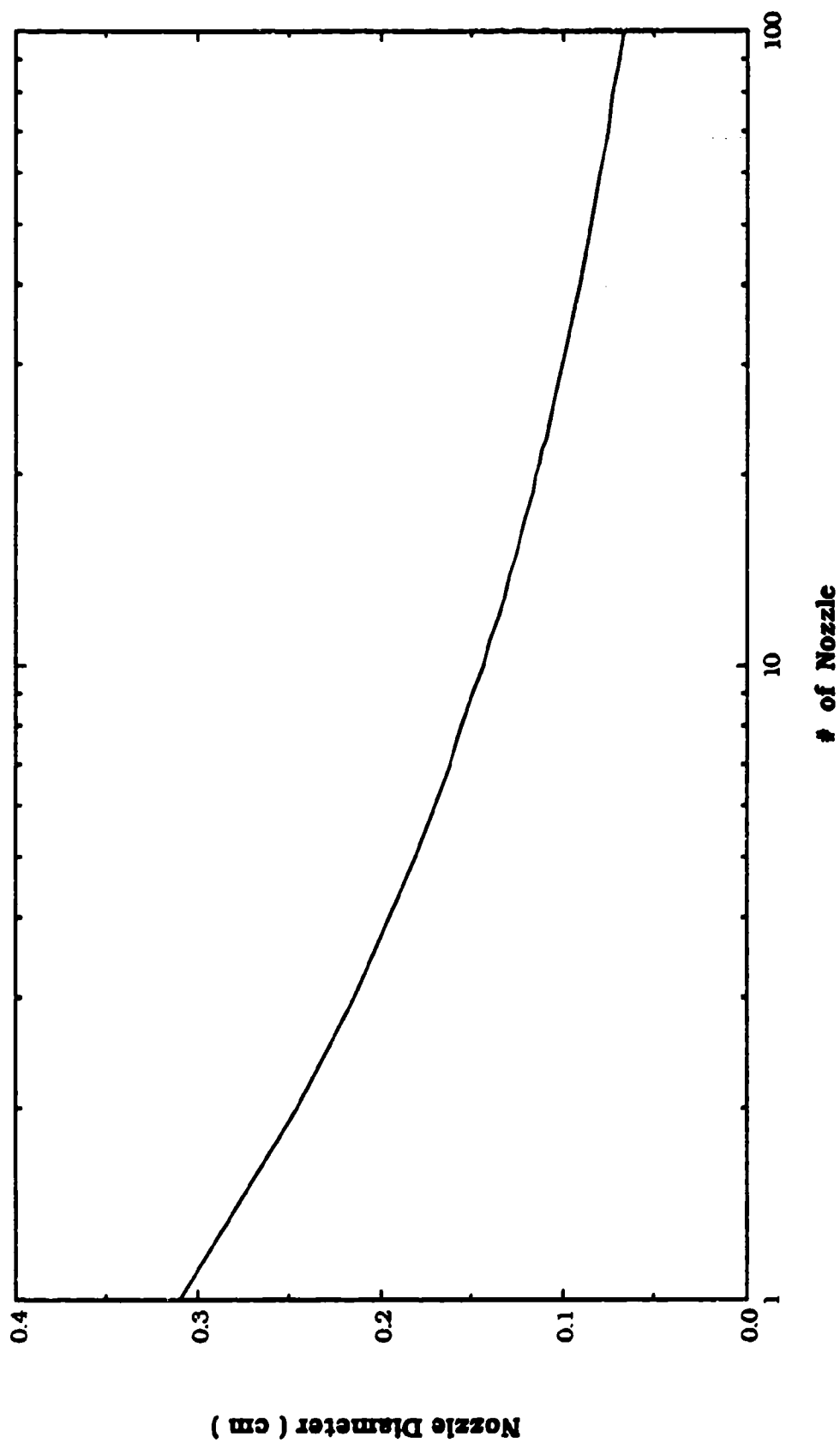
Multiple Nozzle Virtual Impactor Concentrator (  $Q = 22 \text{ lpm}$  )

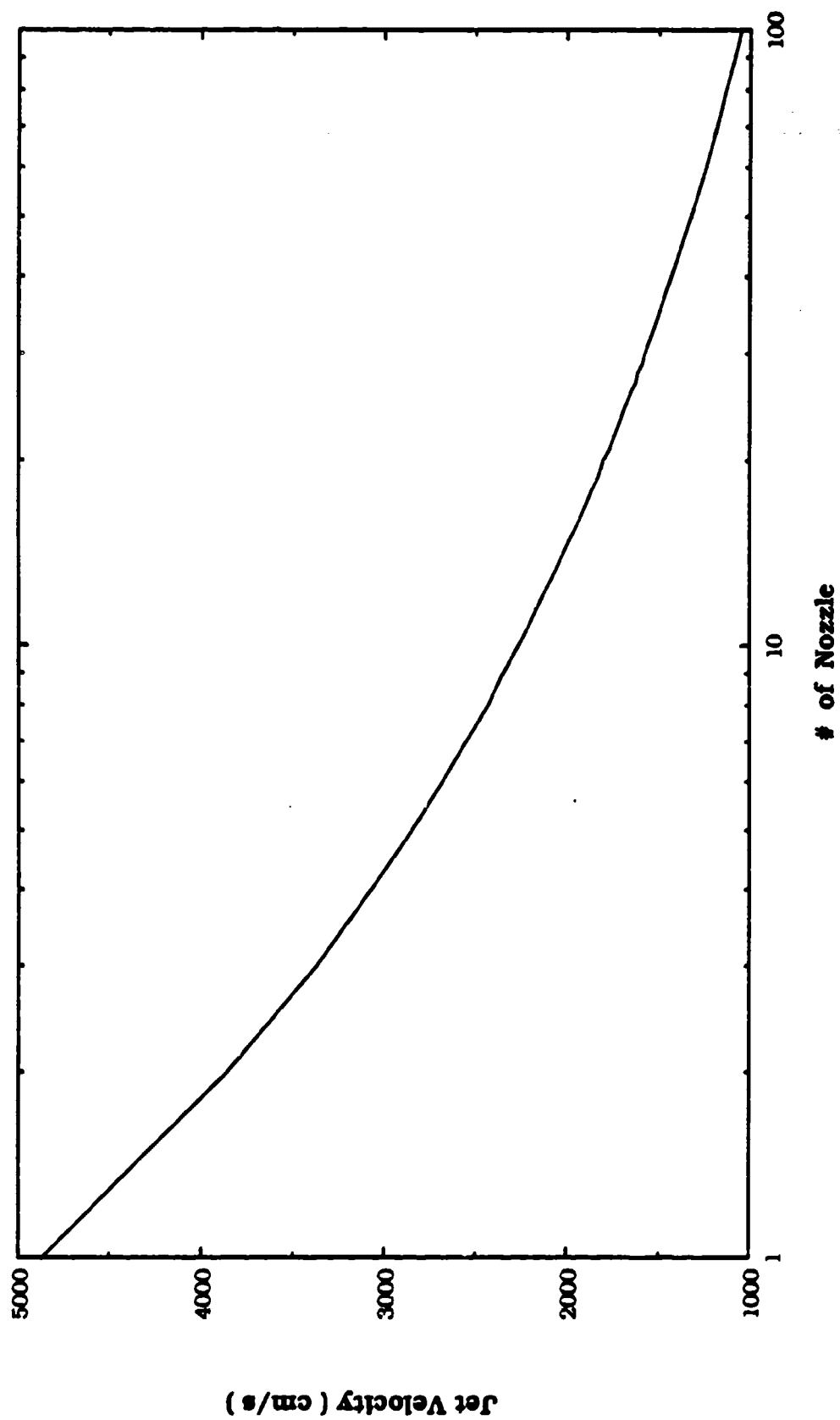


Multiple Nozzle Virtual Impactor Concentrator (  $Q = 22 \text{ lpm}$  )

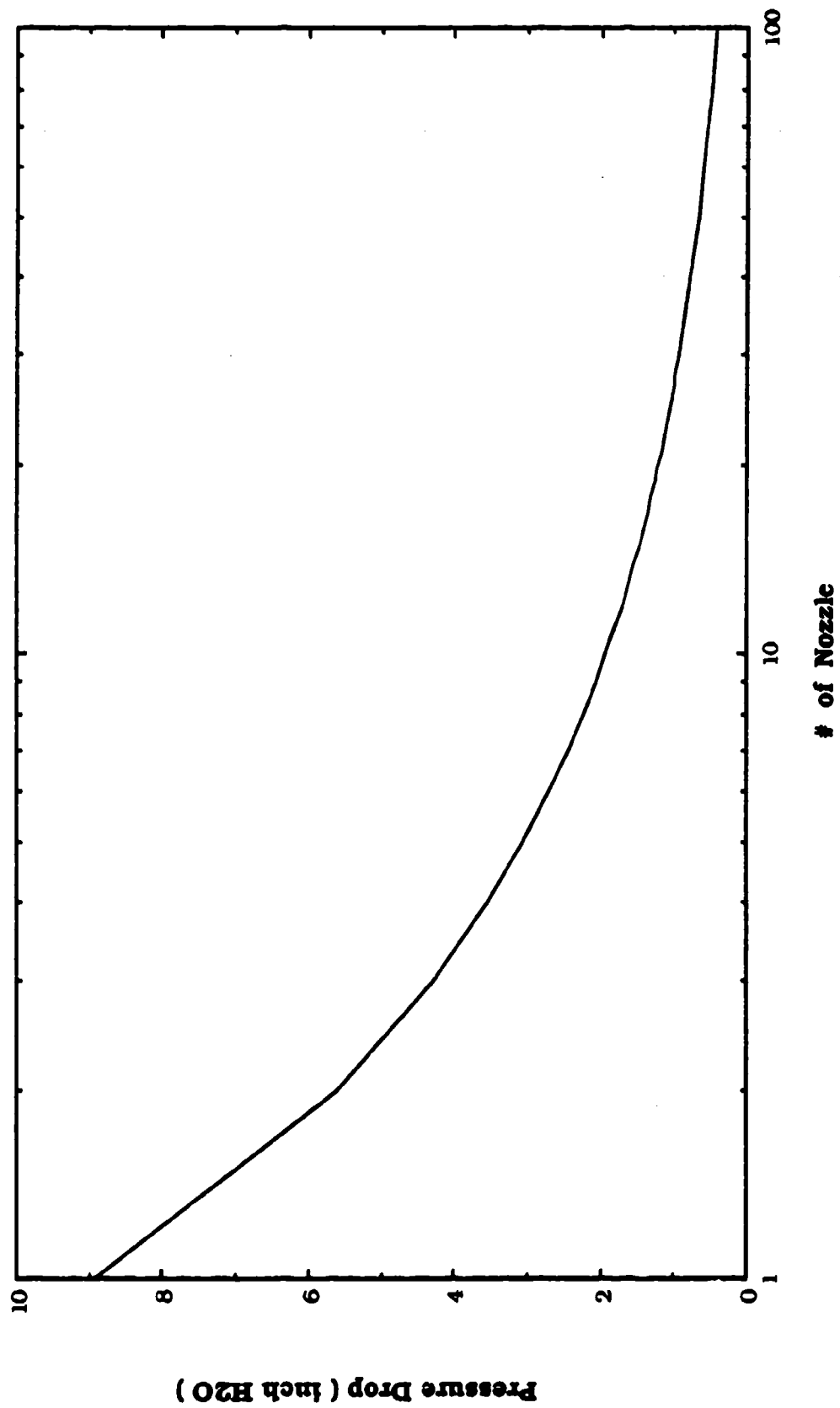


# Multiple Nozzle Virtual Impactor Concentrator ( $Q = 22 \text{ lpm}$ )

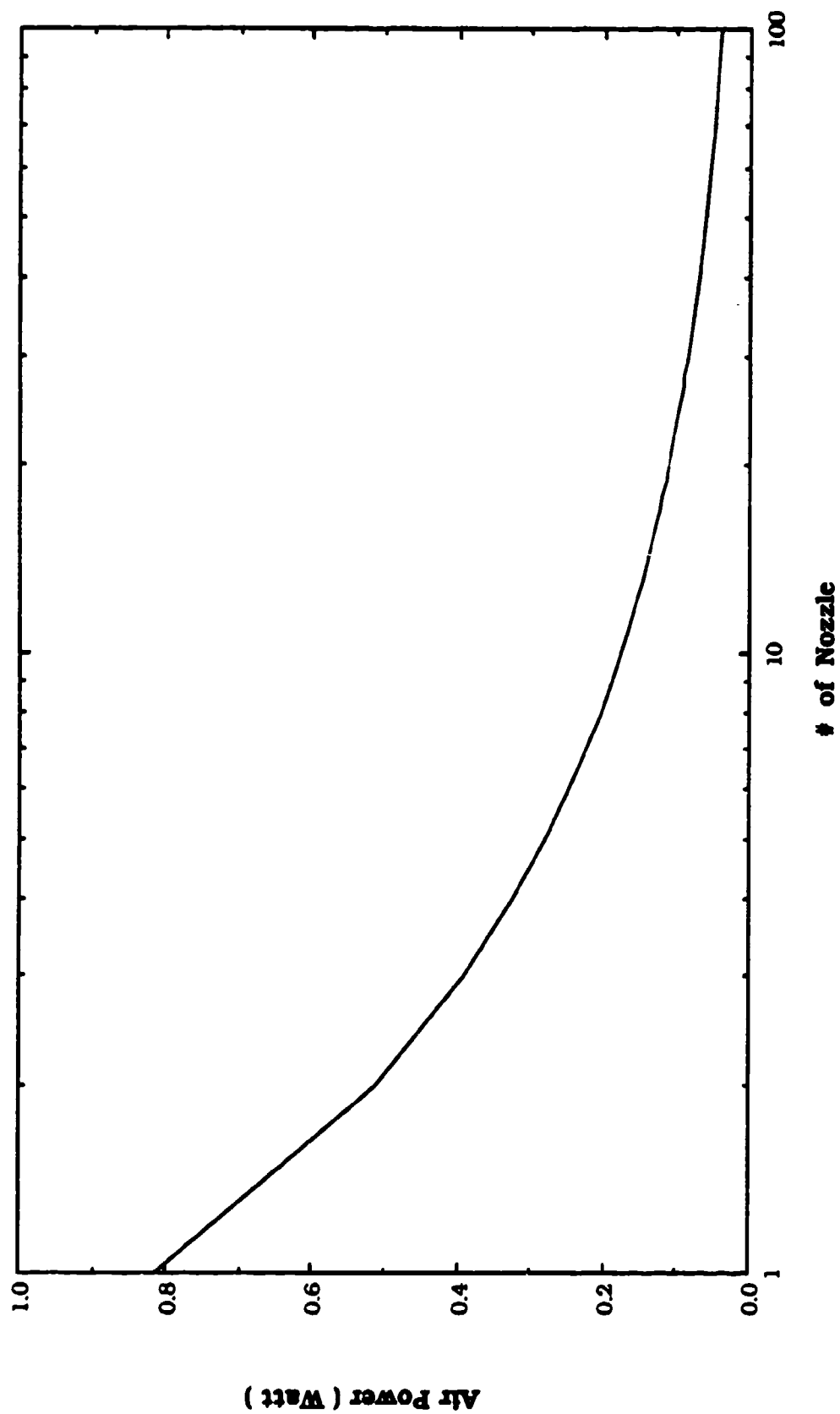


**Multiple Nozzle Virtual Impactor Concentrator (  $Q = 22$  lpm )**

Multiple Nozzle Virtual Impactor Concentrator (  $Q = 22 \text{ lpm}$  )

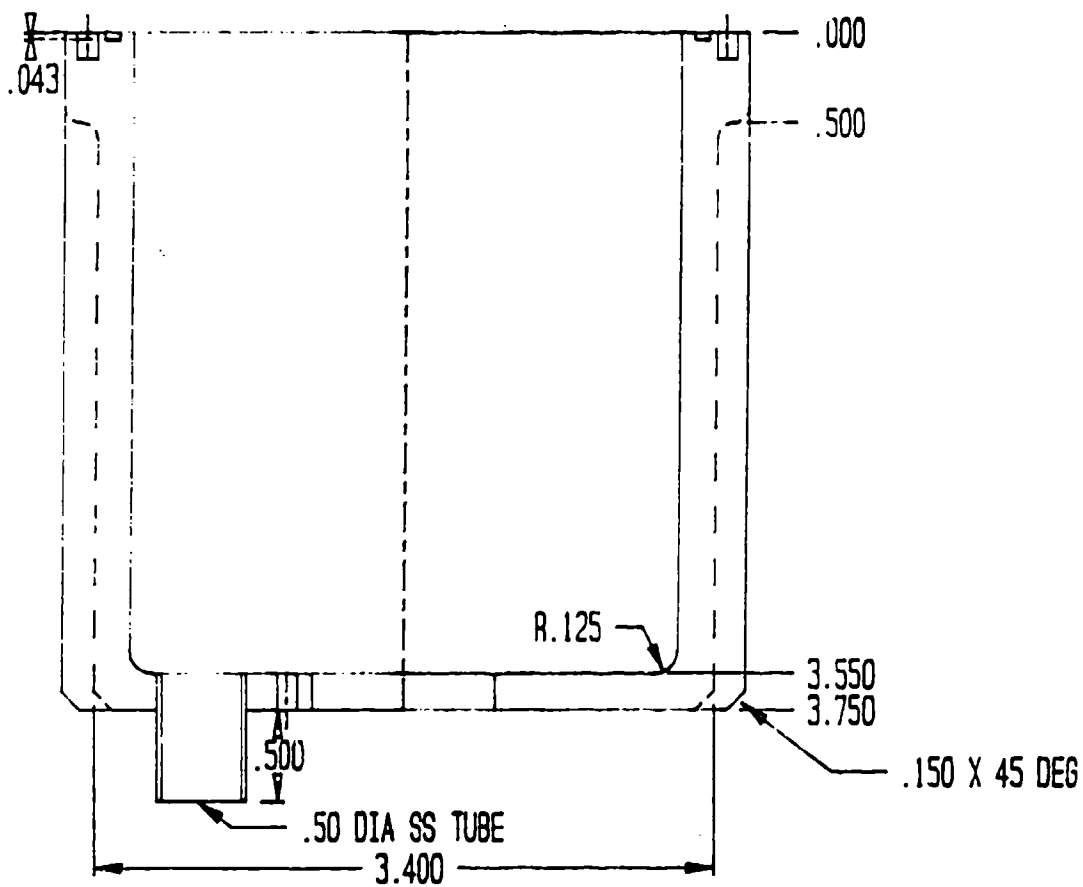
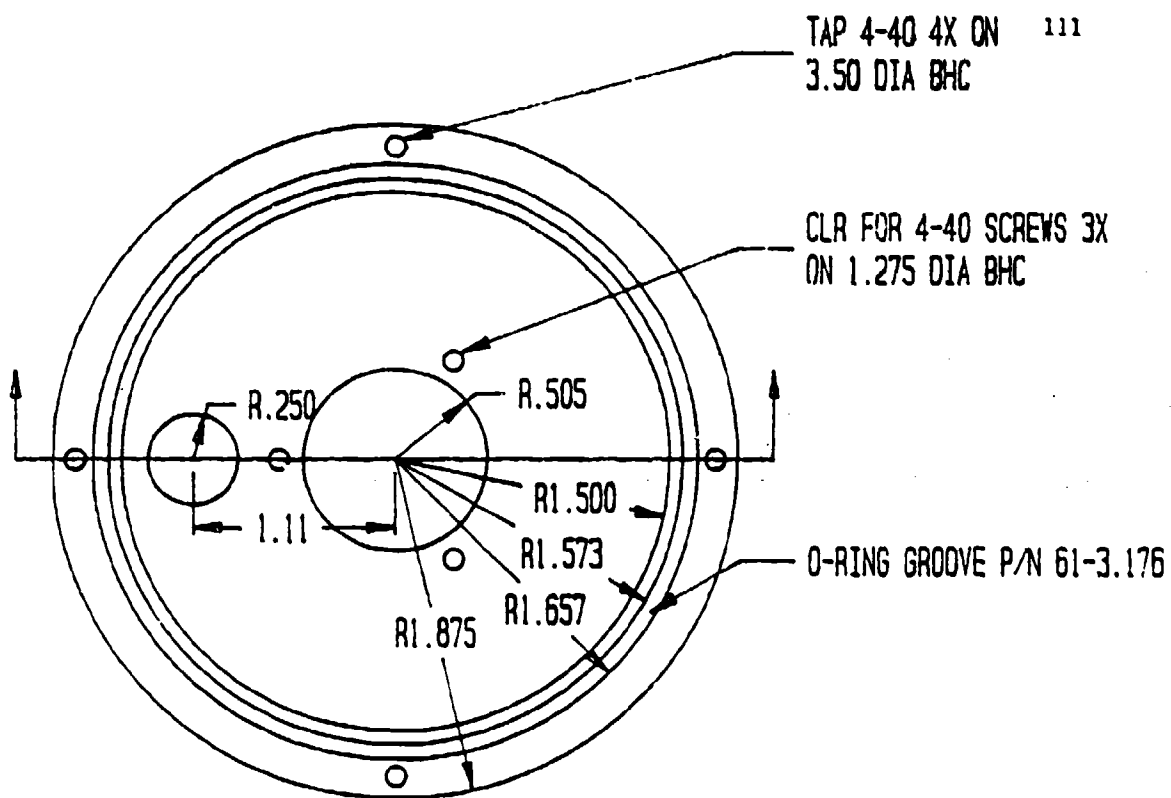


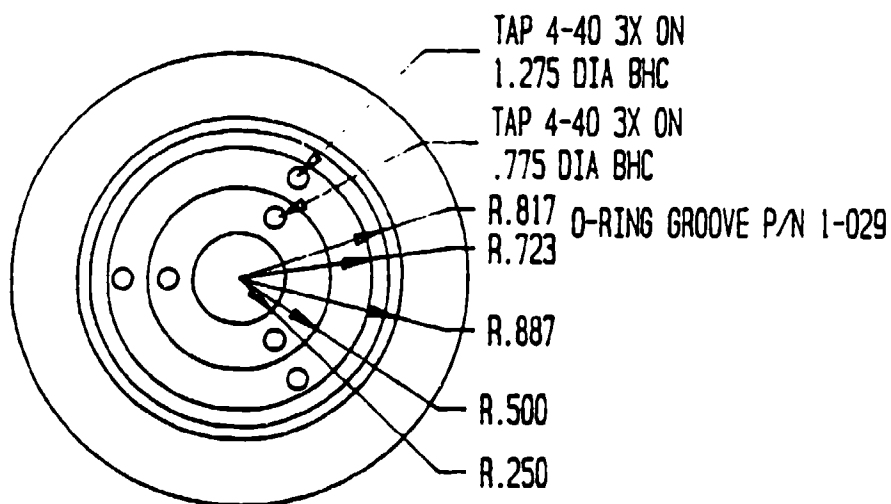
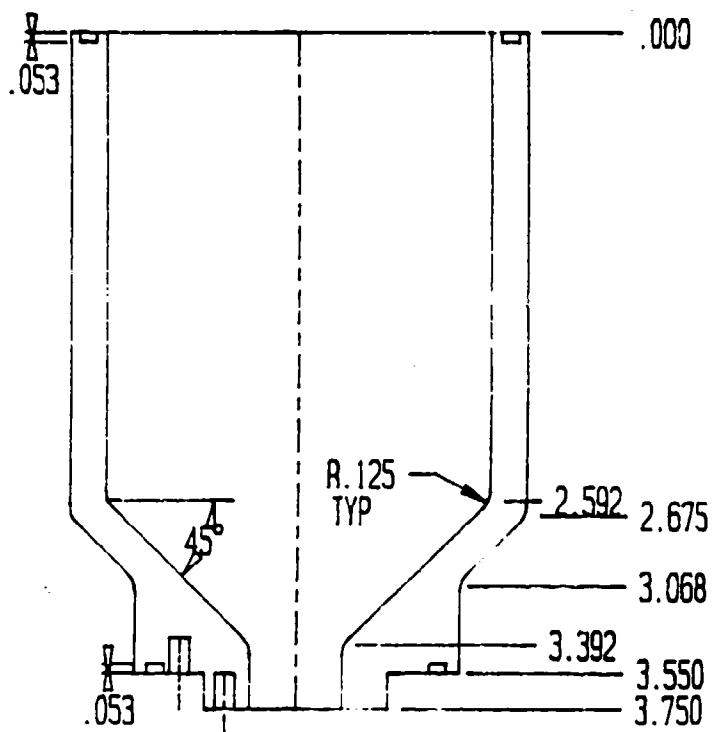
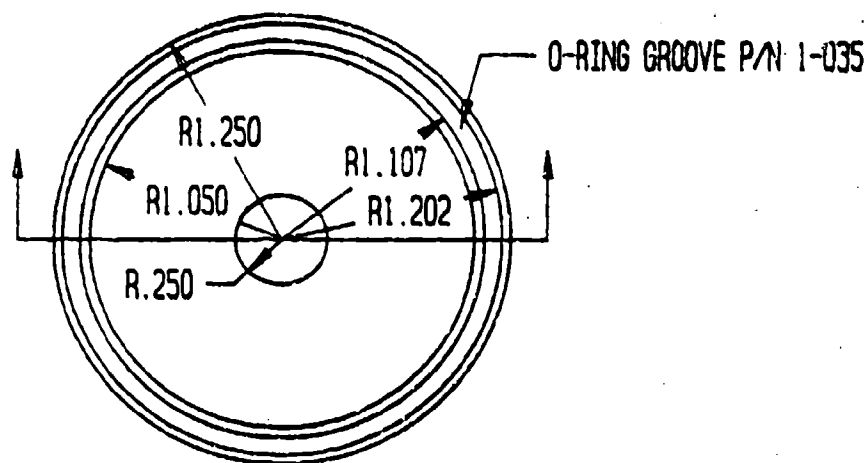
Multiple Nozzle Virtual Impactor Concentrator (  $Q = 22 \text{ lpm}$  )

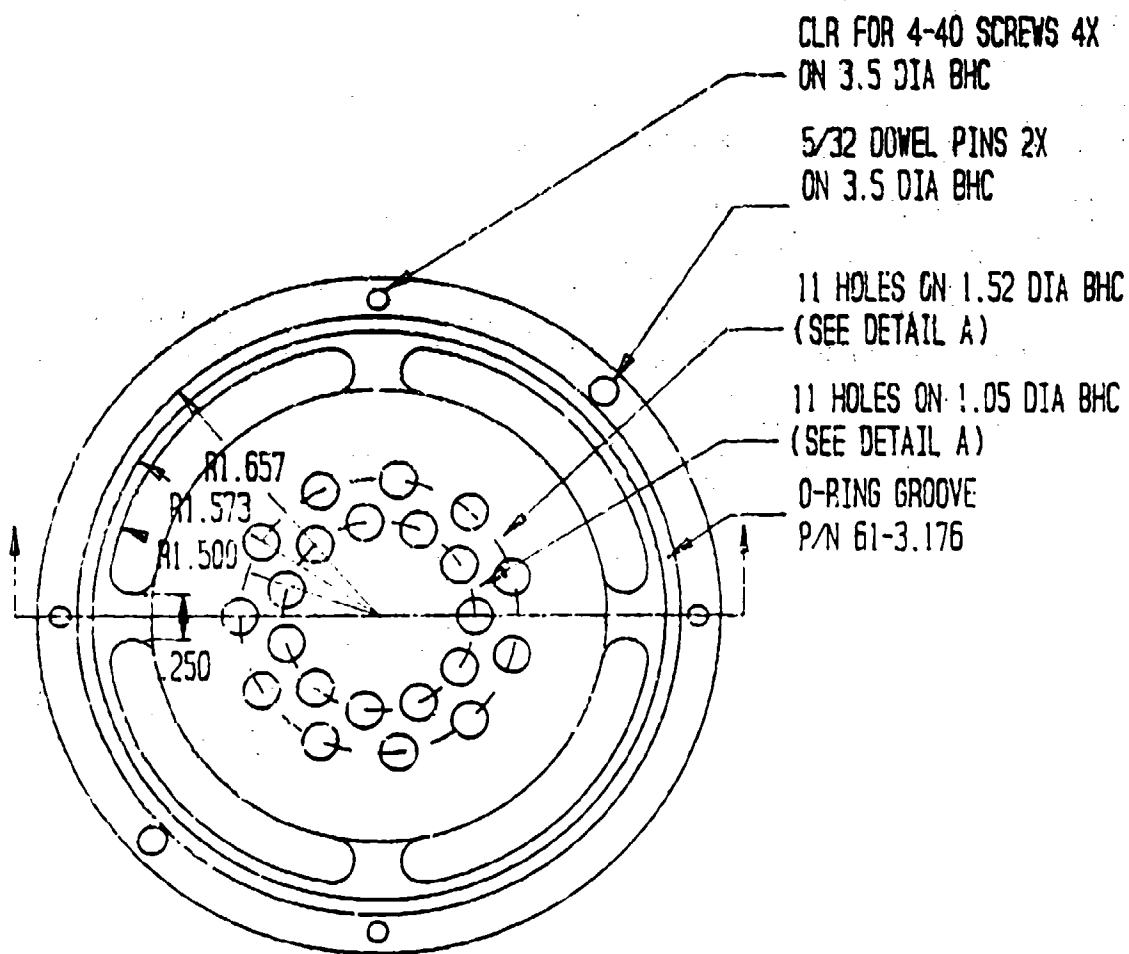


## Appendix C

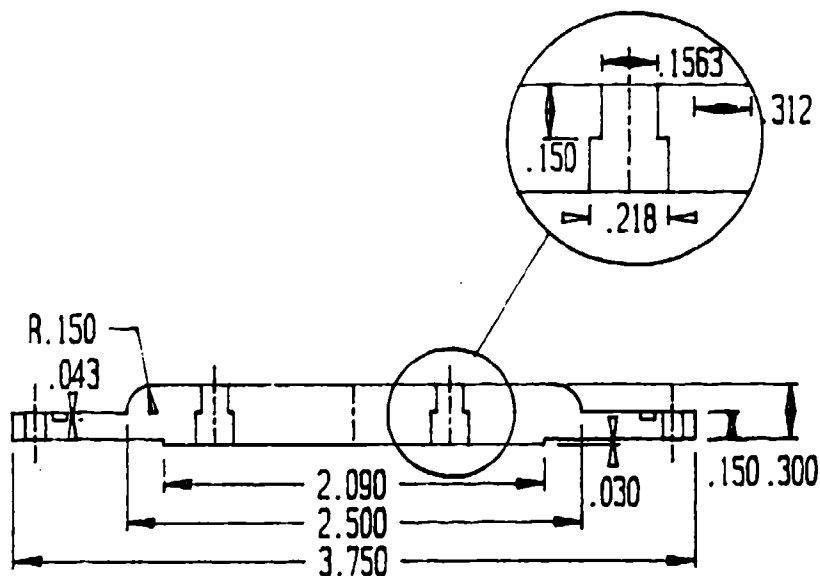
### Design Drawings for the Virtual Impactor Concentrator

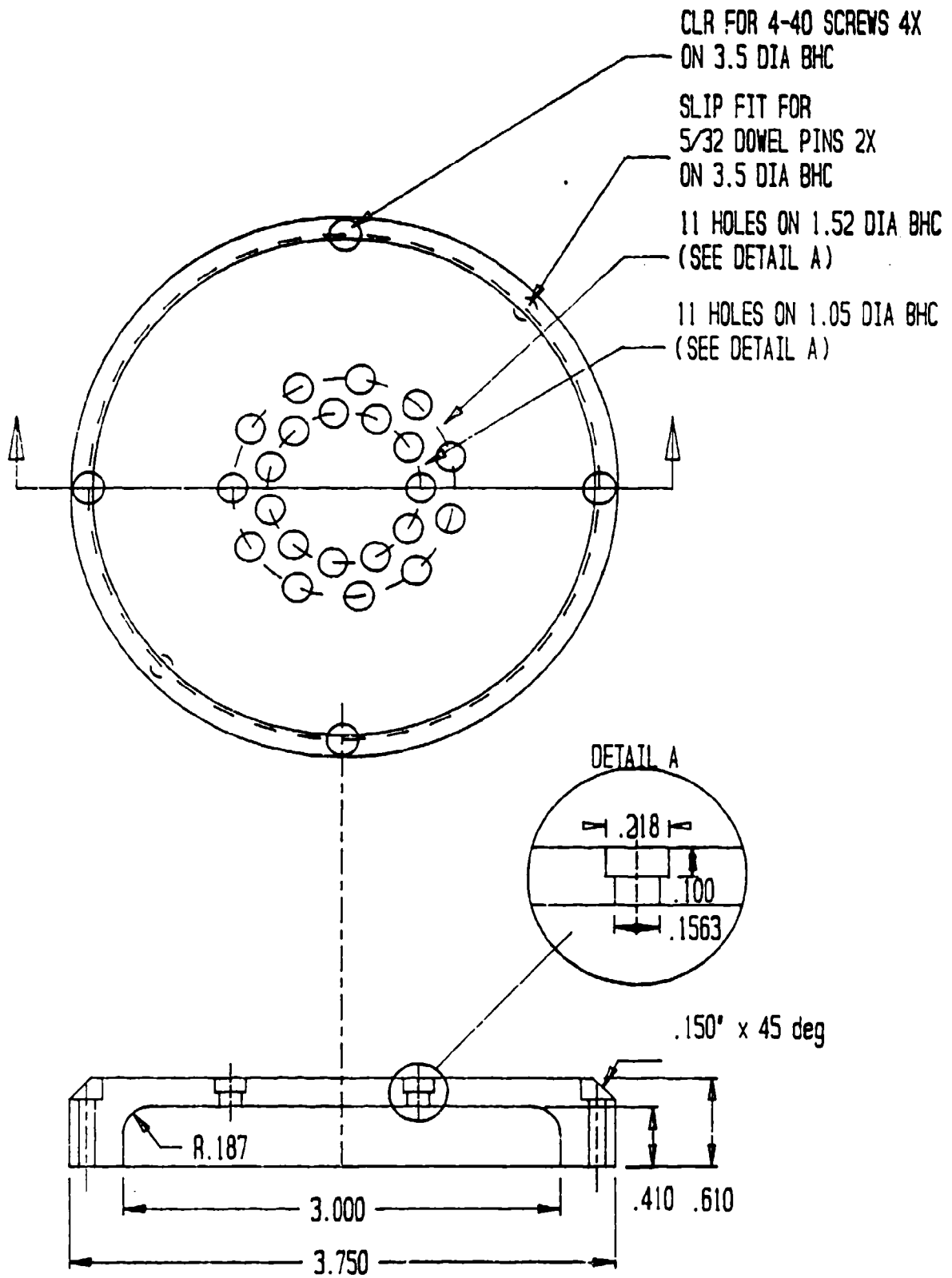


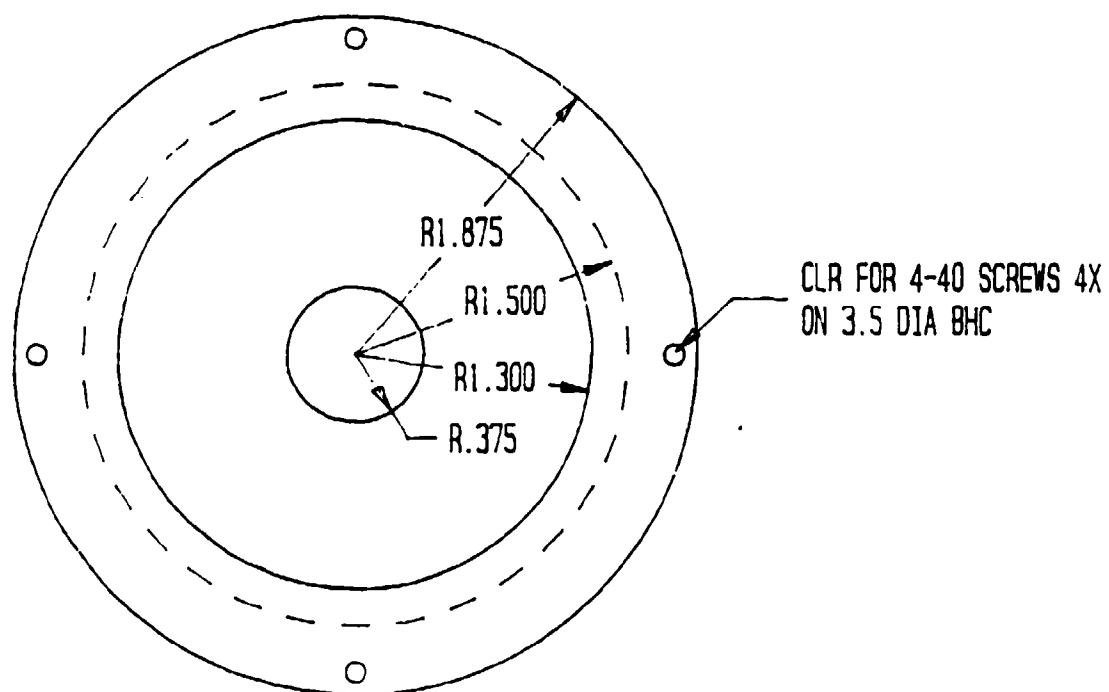
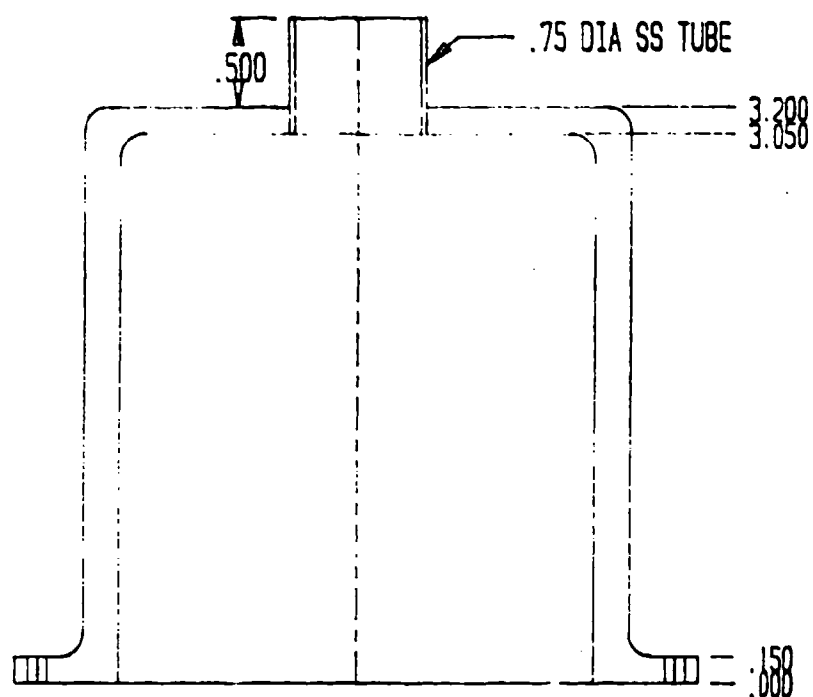




DETAIL A







END

FILMED

3-90

DTIC